



**Filipe Ventura Grilo**

Master of Science

## **High-temperature plasmas of interest to astrophysics and fusion reactors**

Dissertation submitted in partial fulfillment  
of the requirements for the degree of

Master of Science in  
**Physics Engineering**

Supervisor: Prof. Doctor Pedro Amaro, Assistant Professor,  
NOVA University of Lisbon

### Examination Committee

- Chair: Doctor André João Maurício Leitão do Valle  
Wemans, Assistant Professor, NOVA University of  
Lisbon
- Referee: Doctor Miguel Ângelo Pignatelli de Avillez,  
Assistant Professor, University of Évora
- Member: Doctor Pedro Manuel Duarte Gonçalves Amaro,  
Assistant Professor, NOVA University of Lisbon



FACULDADE DE  
CIÊNCIAS E TECNOLOGIA  
UNIVERSIDADE NOVA DE LISBOA

**November, 2020**



## **High-temperature plasmas of interest to astrophysics and fusion reactors**

Copyright © Filipe Ventura Grilo, NOVA School of Science and Technology, NOVA University Lisbon.

The NOVA School of Science and Technology and the NOVA University Lisbon have the right, perpetual and without geographical boundaries, to file and publish this dissertation through printed copies reproduced on paper or on digital form, or by any other means known or that may be invented, and to disseminate through scientific repositories and admit its copying and distribution for non-commercial, educational or research purposes, as long as credit is given to the author and editor.



## ACKNOWLEDGEMENTS

I would like to express my deep gratitude to my supervisor Prof. Dr. Pedro Amaro for all the guidance, knowledge sharing active support that were fundamental for the realization of this work, as well as my personal scientific growth. This gratitude extends to all the professors and colleagues from FCT NOVA's Physics Department for teaching and accompanying me on my education journey.

I would also like to offer my special thanks to all the co-authors of the paper that resulted from this work by providing all the experimental EBIT data and supporting the project. In particular, I would like to thank Priv.-Doz Dr. José R. Crespo López-Urruita and Dr. Chintan Shah for personally reviewing and advising the making of the paper, as well as Prof. Stefan Schippers for providing the raw data of Fe XVII DR rates measured at the Test Storage Ring in Heidelberg, and Prof. José Marques for providing the MCDF calculations.

Finally, I am particularly grateful to my family for always supporting my goals unconditionally. Special thanks to Miriam Colaço for being by my side all the time and believing in me no matter what.



## ABSTRACT

---

Physical interpretations of astrophysical observations of hot plasmas are made with models based on atomic data, being most of this from theoretical calculations of atomic structure and collisional processes. Recently, discrepancies have been arising between observations, laboratory experiments and the theoretical models.

Among the several collision processes included in these theoretical plasma models, Dielectronic Recombination (DR) constitutes an essential process for the plasma ionic balance. In this work, measurements of DR of Fe XVII and Kr XXVII from EBIT, as well as charge state dynamics simulations of the experiments and new FAC, MBPT and MCDF cross section calculations, are presented. Moreover, experimental DR rates were extracted and compared with widely used atomic databases.

Several discrepancies between the experimental data, the new calculations and existing atomic databases were found and discussed. This dissertation provides new DR atomic data for Fe XVII that is relevant for charge state balance calculations and spectral simulation of astrophysical plasmas. Furthermore, new data of DR of Kr XXVII is also presented, which can have future implications for the development of diagnostic tools that are currently in need for the development of future fusion reactors.

**Keywords:** Atomic data, Atomic processes, Highly charged ions, spectroscopy, Laboratory astrophysics, Plasmas, X-ray.

---





## RESUMO

---

Interpretações físicas de observações astronômicas de plasmas de alta temperatura recorrem a modelos baseados em dados atômicos, sendo que a maior parte provem de cálculos teóricos de estrutura atômica e processos de colisão. Recentemente, têm sido verificadas discrepâncias entre observações, experiências laboratoriais e modelos teóricos.

Dentro dos processos de colisão incluídos nestes modelos teóricos, a Recombinação Dielectrónica (DR) tem um papel essencial no balanço iónico do plasma. Neste trabalho foram apresentadas medições de DR de Fe XVII e Kr XXVII em EBIT, bem como simulações da dinâmica dos estados de carga nas experiências e novos cálculos de secção eficaz de DR feitos com FAC, MBPT e MCDF. Foram também extraídos valores experimentais de taxas de DR para comparar com valores de bases de dados amplamente usadas em astrofísica.

Foram encontradas e discutidas diversas discrepâncias entre os dados experimentais, os novos cálculos teóricos e as bases de dados existentes. Esta dissertação fornece novos dados de DR do Fe que são relevantes em cálculos de balanço de estados de carga e simulação do espectro de plasmas astrofísicos. As medições de Kr podem ter implicações no desenvolvimento de ferramentas de diagnóstico que são necessárias para o desenvolvimento de futuros reatores de fusão.

**Palavras-chave:** Dados atômicos, Processos atômicos, Iões altamente carregados, Espectroscopia, Astrofísica em laboratório, Plasmas, Raios-X.

---



# CONTENTS

<b>List of Figures</b>	<b>xiii</b>
<b>List of Tables</b>	<b>xv</b>
<b>Acronyms</b>	<b>xvii</b>
<b>Symbols</b>	<b>xix</b>
<b>1 Introduction</b>	<b>1</b>
1.1 X-ray astronomy . . . . .	1
1.2 Astrophysical plasmas in laboratory . . . . .	3
1.3 Need for atomic data . . . . .	5
1.3.1 Astrophysics . . . . .	5
1.3.2 Fusion reactors . . . . .	8
1.4 Organisation of the thesis . . . . .	9
<b>2 Theory</b>	<b>11</b>
2.1 Atomic structure . . . . .	12
2.1.1 One-electron systems . . . . .	12
2.1.2 Multi-electron systems . . . . .	13
2.1.3 Hartree-Fock method . . . . .	14
2.1.4 Configuration Interaction . . . . .	14
2.1.5 Multiconfiguration Dirac-Fock . . . . .	15
2.1.6 Many Body Perturbation Theory . . . . .	16
2.1.7 Continuum atomic wavefunction . . . . .	17
2.2 Decay processes . . . . .	18
2.2.1 Radiative decay . . . . .	18
2.2.2 Auger decay . . . . .	21
2.3 Electron-ion collision processes . . . . .	22
2.3.1 Collisional excitation and ionization . . . . .	23
2.3.2 Electron-ion recombination . . . . .	24
2.4 Charge exchange . . . . .	27
2.5 Polarization and anisotropy . . . . .	27

## CONTENTS

---

2.5.1	E1 and M1 transitions . . . . .	30
2.6	Atomic codes . . . . .	32
2.6.1	Flexible Atomic Code . . . . .	32
2.6.2	Multiconfiguration Dirac-Fock codes . . . . .	33
<b>3</b>	<b>Experimental Setup</b>	<b>35</b>
3.1	The Electron Beam Ion Trap . . . . .	35
3.1.1	Electron beam dynamics . . . . .	37
3.2	FLASH-EBIT . . . . .	39
3.2.1	Specifications . . . . .	39
3.2.2	Fe XVII measurement . . . . .	40
3.3	PolarX-EBIT . . . . .	42
3.3.1	Specifications . . . . .	42
3.3.2	Fe XVII measurement . . . . .	43
3.4	Test Storage Ring . . . . .	44
<b>4</b>	<b>Computational calculations and simulations</b>	<b>47</b>
4.1	Cross section calculations . . . . .	47
4.1.1	LMM DR calculations . . . . .	48
4.1.2	Collisional cross-section calculations . . . . .	51
4.2	Charge state dynamics simulations . . . . .	56
4.2.1	EBIT plasma and spectra simulations . . . . .	60
4.2.2	Spectral time evolution simulations . . . . .	63
4.3	Preliminary Kr charge state simulations . . . . .	65
<b>5</b>	<b>Experimental results and discussion</b>	<b>69</b>
5.1	Fit procedure . . . . .	73
5.2	DR resonant energy and strengths . . . . .	74
5.3	DR rates . . . . .	79
5.4	Preliminary Kr results . . . . .	84
<b>6</b>	<b>Conclusions and future prospects</b>	<b>85</b>
	<b>Appendices</b>	<b>87</b>
	<b>A Publications</b>	<b>87</b>
	<b>Bibliography</b>	<b>89</b>

## LIST OF FIGURES

1.1 Crab nebula observations . . . . .	2
1.2 3C and 3D measurements . . . . .	5
1.3 3C/3D oscillation strength ratio . . . . .	7
1.4 International Thermonuclear Experimental Reactor . . . . .	8
2.1 Schematic of the DR, RR, EA, CI, CE and RE processes . . . . .	22
2.2 Coordinate system of the DR emission angular distribution . . . . .	28
3.1 General representation of an EBIT . . . . .	36
3.2 Artistic representation of an ion cloud in an EBIT . . . . .	38
3.3 Simulation of the ion trajectory in an EBIT . . . . .	38
3.4 Cross-sectional view from the FLASH-EBIT . . . . .	39
3.5 Electron gun and collector from FLASH-EBIT . . . . .	40
3.6 Energy scheme of the FLASH-EBIT . . . . .	41
3.7 Cross-sectional view from the Heidelberg compact EBIT design . . . . .	42
3.8 Electron gun and collector from FLASH-EBIT . . . . .	43
3.9 Energy scheme of the PolarX-EBIT . . . . .	44
3.10 Scheme of the TSR . . . . .	45
4.1 FAC and MCDF FE XVII DR LMM calculations . . . . .	48
4.2 Example of MBPT calculation . . . . .	50
4.3 DR LM $n$ structure for Fe Ne-like . . . . .	51
4.4 CI and EA cross section for Fe Na-like . . . . .	56
4.5 RR cross section for Fe Ne-like . . . . .	57
4.6 Ionization energies for Fe and Kr . . . . .	59
4.7 Charge state dynamic simulations of a Fe plasma under different current density and electron energy conditions . . . . .	60
4.8 Simulation of the FLASH-EBIT experiment under different electron densities . . . . .	61
4.9 Simulation of the Fe XVII DR-LMM spectrum for different charge exchange rates. . . . .	63
4.10 DR LMM peak decays over time in the PolarX-EBIT experiment . . . . .	64
4.11 PolarX-EBIT measured effective electron current . . . . .	64
4.12 Spectral time evolution . . . . .	66

LIST OF FIGURES

---

4.13 Kr charge state simulations . . . . .	67
5.1 FLASH-EBIT experimental results . . . . .	70
5.2 PolarX-EBIT experimental results . . . . .	71
5.3 FAC Fe XVII DR-LMM calculation broadened to match experimental conditions	71
5.4 TSR Fe XVII DR-LMM measurements. . . . .	72
5.5 Fit of the experimental results . . . . .	75
5.6 Comparison between experimental results and theoretical calculations of the DR LMM cross section . . . . .	80
5.7 Kr experimental results . . . . .	81
5.8 Kr DR-LMM preliminary results . . . . .	83

## LIST OF TABLES

4.1	Relevant theoretical values of DR-LMM resonant energy and strength . . . .	52
4.2	Continuation of table 4.1. . . . .	53
4.3	Wavelengths of the transitions listed in the tables 4.1 and 4.2 . . . . .	54
4.4	Continuation of table 4.3. . . . .	55
5.1	Experimental resonant energies for the DR-LMM . . . . .	76
5.2	Experimental resonant strengths for the DR-LMM . . . . .	77
5.3	Experimental DR coefficient rates dor DR-LMM . . . . .	82





## ACRONYMS

CE	Collisional Excitation
CI	Collisional Ionization / Configuration Interaction
CX	Charge Exchange
DW	Distorted Wave
EA	Excitation with Autoionization
EBIT	Electron Beam Ion Trap
FAC	Flexible Atomic Code
FWHM	Full Width Half Maximum
GRASP	General-Purpose Relativistic Atomic Structure Program
HCI	Highly Charged Ion
ITER	International Tokamak Experimental Reactor
MBPT	Many Body Perturbation Theory
MCDF	Multiconfiguration Dirac-Fock
MCDFGME	Multiconfiguration Dirac-Fock and General Matrix Element
RE	Resonant Excitation
REDA	Resonant Excitation with Double Autoionization
RR	Radiative Recombination
RR	Dielectronic Recombination
TSR	Test Storage Ring



## SYMBOLS

$A^a$	Auger decay rate
$A^r$	Spontaneous emission decay rate
$c$	Speed of light
$\Phi$	Configuration state function
$\alpha^{DR}$	Dielectronic recombination rate coefficient
$e$	Population of ions with charge $q$
$E$	Energy
$\phi^f$	Free electron orbital
$h$	Planck's constant
$H$	Hamiltonian
$I_e$	Electron beam current
$j$	Total angular momentum
$j_e$	Current density
$\kappa$	Relativistic angular momentum
$K_B$	Boltzmann's constant
$m_e$	Electron mass
$n$	Principal quantum number
$N_q$	Population of ions with charge $q$
$P$	Degree of polarization
$\phi_{n\kappa m}$	Dirac spinor

## SYMBOLS

---

$\Psi$	Atomic wavefunction
$r$	Electron radial position
$r_B$	Brillouin radius
$r_H$	Herrmann radius
$\Phi^S$	Slater determinant
$\sigma$	Cross section
$T$	Temperature
$V_{ij}^{e-e}$	Electron-electron interaction potentials
$W$	Angular distribution

## INTRODUCTION

### 1.1 X-ray astronomy

Optical astronomy has had a rich history over the last centuries. Observations by primordial telescopes developed by Galileu provided vast and detailed information of the observable cosmos, such as the phases on Venus and the moons of Jupiter, both discovered in 1610 [1]. With technological advances in optics and increasing size of telescopes even allowed observation of distant and faint objects, like the GN-z11 galaxy in 2016 (currently the furthest galaxy observed) [2]. However, observation of certain regions of the electromagnetic spectrum was only possible after the middle of the 20<sup>th</sup> century. Planet Earth's atmosphere is optically thick to x-ray radiation, which means that most x-rays coming from space are scattered and absorbed before reaching the surface. Before the start of space exploration, even without observations, the sun was already theorized to be a source of x-ray radiation, being the possible culprit for the strong ionization of the ionosphere [3]. In the end of 1940's, a photographic plate attached to a V-2 rocket (protected by a Be window) was able to detect x-rays beyond the atmosphere [4]. Later, another V-2 rocket with the ability to roll around its flight axis confirmed that the x-ray source was the sun [5]. These discoveries, and the advancement of space technology, allowed the beginning of the x-ray astronomy. In 1962, the first x-rays coming from outside the solar system were detected by an Aerobee 150 rocket [6], which its source is a low mass x-ray binary. While a few more sources were discovered by the use of rockets, the development of x-ray space observatories made possible to catalog more than 200000 sources by the end of the century [7]. The advancement of this technology made possible not only to spatial imaging of the sources of x-ray, but also to make analysis of the respective spectrum, which provided more tools to investigate the nature and behavior of the celestial bodies.

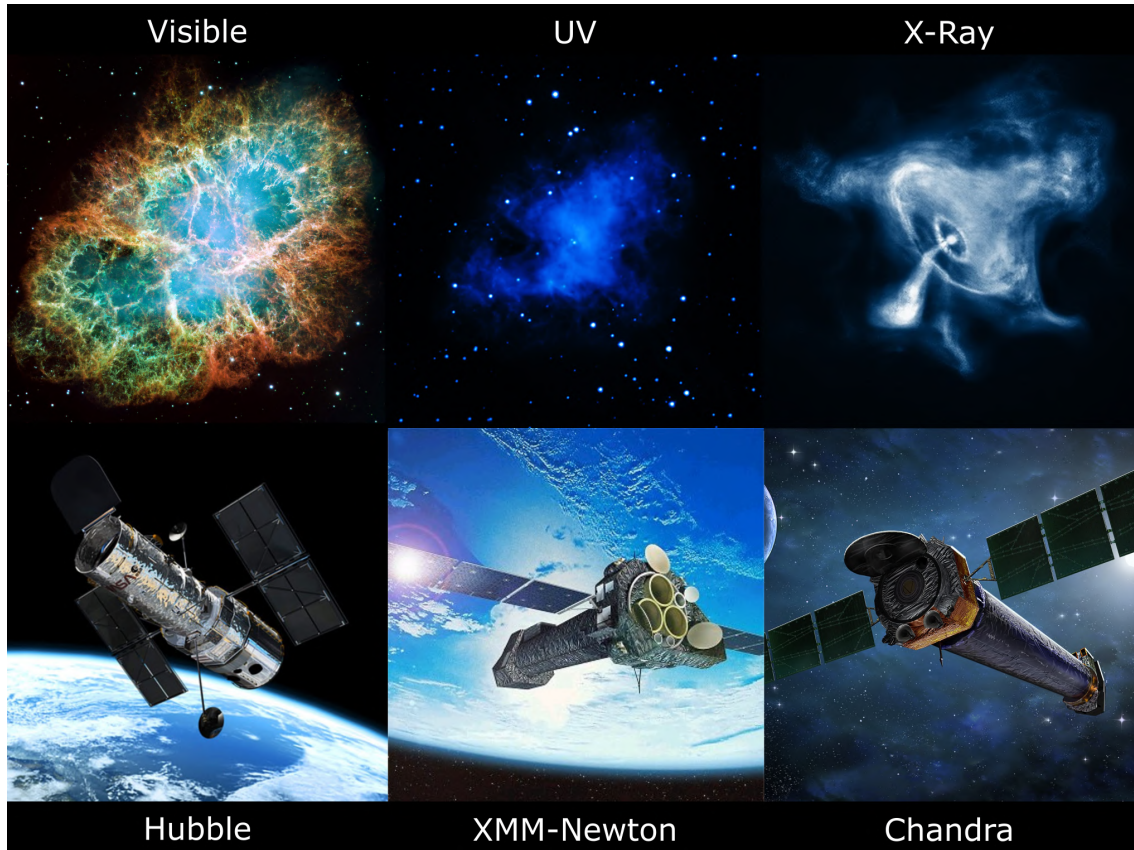


Figure 1.1: Observations of the Crab nebula in the visible, ultra-violet (UV) and x-ray energy range. The images were acquired by the Hubble, XMM-Newton and Chandra space observatories, respectively. Images adapted from [17].

Nowadays, most of the x-ray observations are made in on-going missions of the satellites XMM-Newton [8] and Chandra [9], both launched in 1999, and NuSTAR [10], launched in 2012. The first has a low-energy reflection grating detector with an energy range of 0.35 to 2.5 keV, while Chandra has both a low and high-energy transmission grating detector, with ranges of 0.08 to 6 keV and 0.5 to 10 keV. Both also have CCD detectors for x-ray imaging purposes. Figure 1.1 shows observations of the Crab Nebula made by the Hubble, XMM-Newton and Chandra telescopes for the visible, ultra-violet and x-ray energy ranges, respectively. In this case, x-ray imaging allowed direct observation of behaviour of a pulsar (rapidly spinning neutron star) that lies in the heart of the nebula [11]. The mentioned observatories have been used extensively to study extreme astrophysical systems, like binary systems, supermassive black holes and pulsars [12–14]. These satellites originated many discoveries in astrophysics, but their grating spectrometers are impractical for very faint sources. The NuSTAR telescope uses x-ray optics with a 10.14 m focal length to focus x-rays on a solid-state detector. This observatory is complementary to the previous ones, as it is designed to study hard x-rays, with an energy range of 3 to 79 keV. The next generation satellites, XRISM [15] (planned to launch in 2022) and Athena [16] (planned to launch in 2031) will overcome this problem by employing

detectors with higher sensitivity and resolution, and a bigger aperture.

Cosmic sources that exhibit high energy process, like stars, binary systems, pulsars and black holes, generate high temperature plasmas (MK) composed of Highly Charged Ions (HCI). The x-ray spectra of these objects contains signatures of the most astrophysically abundant elements, usually with atomic number  $Z \leq 30$ . Astrophysical plasmas are usually classified as either photoionized plasmas or coronal plasmas. In the first type, there is a strong source of continuum photon radiation that is responsible for the ionization of the gas, and consequently for the charge balance of the ion populations [18]. The electron temperature is normally low and does not have to exceed a certain ionization potential for the dominant ion species to appear. These plasmas are usually found near powerful radiation sources, such as active galactic nuclei and x-ray binaries [18]. In coronal plasmas, the charge state balance is established by electron-ion collisions, namely the ionization and recombination collisional processes [19]. Here, the electrons have Maxwellian or quasi-Maxwellian energy distributions and their temperature is comparable to most of the ionic species temperatures. These plasmas are commonly found in clusters of galaxies and stellar coronae. The electron densities are commonly found to be in the order of  $n_e \approx 10^8$  to  $10^{13} \text{cm}^{-3}$  [19]. Due to the low density in the coronal limit, the radiative and Auger decay rates are much higher than the collision rates, which leads to spectra dominated by emission lines of resonant processes, such as the Dielectronic Recombination [18, 19]. Here, the ion density is sufficiently low for the absorption of the radiative emissions by the plasma itself to be considered negligible. X-ray spectroscopy of these plasmas provides a variety of information about the physical conditions of celestial bodies. Since this kind of spectra are directly related to the electronic structure of the HCI, quantities such as chemical composition, temperature and electronic density of the plasma can be inferred through experimental data analysis and plasma modeling. As we shall see in the next section and chapters 3 and 4, these plasma conditions are similar to ones produced in artificial plasmas, in particular to the case of electron densities.

## 1.2 Astrophysical plasmas in laboratory

Unlike many other areas of physics, experimental data in astronomy can only be obtained by observing the universe without control of the physical parameters of objects in study. As such, there is no possibility to study the physical processes individually, as the observed photons are produced by all the physical processes that happen simultaneously. Therefore, to test new astrophysical theories, models that simulate the observed objects have to be developed. These models rely heavily on several fields, namely molecular, atomic and nuclear physics, and often with multidisciplinary approaches. This work is focused on the atomic data regarding HCI predominantly present in hot astrophysical plasmas.

With the development of experimental physics technology, it is nowadays possible to emulate hot plasmas with similar conditions to the ones found in outer space. X-ray

sources with HCI, such as magnetic fusion plasma devices [20], laser-produced plasmas [21] and ion traps (details in chapter 3) [22], have been used to extract experimental atomic data with importance to astrophysics. There are many sources of HCI in laboratory, but the Electron Beam Ion Trap (EBIT), the tokamak and storage rings have been the most used ones for laboratory measurements of astrophysical plasmas [19]. Both devices produce low density plasmas in the coronal limit [19], with radiative and autoionization processes being much faster than the electron-ion collision rates, which makes them ideal to study recombination processes. They also provide spectroscopical data, similar to what is observed in x-ray satellites. The EBIT is capable of producing and maintaining HCI systems, which is the main experimental focus of this thesis. As this device is capable of producing a plasma of any element up to bare uranium [23], it is ideal to study plasmas with importance to astrophysics [24]. As described in detail in chapter 3, it also provides methods to study ion-electron recombination processes that play a fundamental role in hot plasma modeling. Apart from the ionic species, the electron energy and density can be selected and controlled, thereby enabling the study of plasmas in a wide variety of conditions. A fuller explanation of the functioning of the EBIT is presented in chapter 3. The Tokamak is another device capable of generating and maintaining high temperature plasmas. In this case, the plasma is magnetically confined in a device with toroidal geometry. The tokamak is generally less versatile than the EBIT, as its electron temperature and density varies throughout the locations of the plasma, i.e. the plasma is generally hotter and denser in its center [19]. The ions are constantly moving and experiencing the different conditions, resulting in emission spectra more complex and difficult to analyse. This downside can also be perceived as an advantage, as in real astrophysical plasmas the ions also experience variations in temperature and density and are also subjected to interplay of several different processes. As such, the tokamak can be used to make realistic tests to the mentioned interplay and reproduce spectra comparable to real astrophysical observations, while an EBIT is mostly used for careful tests of individual atomic processes. Since the EBIT provides means to focus on specific atomic data and check experimentally its accuracy, the EBIT can be the analogous of the "debug tool" of computer coding. An example is the study of the 3C and 3D lines (explained in more detailed in the next section). Figure 1.2 shows an astrophysical observation of the Capella star system with the Chandra telescope, where the lines 3C and 3D produced by Ne-like Fe are identified in the subfigure (b). These lines have been studied in more detail, as is the case of the subfigure (a), where the two lines are observed individually in an EBIT.

Heavy ion storage rings, like the Heidelberg's Test Storage Ring (TSR), are also extensively used to study electron-ion collisional processes [27]. Instead of producing a plasma in a trap, HCI are injected in a ring in the form of a beam that is redirected and refocused to circulate there for extensive periods of time. Additionally, an electron beam is merged with the ion beam with an adjustable relative ion-electron energy. As recombination and ionisation processes occur, the ions with different charge states are selected and their



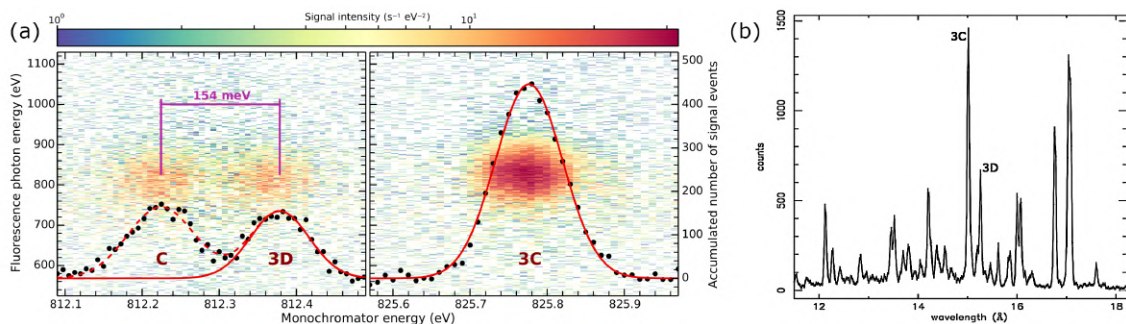


Figure 1.2: (a) Measurement of the 3C and 3D lines in an EBIT [25]. (b) Observation of the 3C and 3D lines in the Capella x-rays [26].

respective current is measured. This enables the study of collisional ionization and recombination cross sections on the HCI charge state population of the beam. However, due to technical restrictions no photon emission is observed. A description of the TSR can also be found in chapter 3.

## 1.3 Need for atomic data

### 1.3.1 Astrophysics

Astrophysical models that predict plasma characteristics from astrophysical observations rely on atomic data that can explain the structures present in the experimental spectra. The case of iron (Fe) is of special importance in x-ray astronomy: this element is the most abundant heavy element in the universe due to its high nuclear binding energy per nuclear particle, with addition that its HCI form has atomic transitions in the x-ray region. Intensity ratios of Fe HCI emission lines depend on the local plasma conditions, and are important candidates for astrophysical diagnostic tools [28, 29]. For example, the degree of polarization of the K-shell emissions of Fe XVII can be used to measure plasma anisotropies, such as electron and ion beam orientations or magnetic field orientations [30]. K-shell line ratios for Fe and Ni have also been used to determine the temperature of galaxies [31].

Another example are the L-shell emission in Fe, in particular for Fe XVII (Ne-like, Fe<sup>16+</sup>) in the 700 to 950 eV photon energy range. Given the closed-shell structure of this ion, the presence of LM x-ray emissions is predominant in the observations [29]. Consequently, several experiments have been performed over the years to provide accurate values of the wavelengths and relative transition intensities for L-shell transition of Fe XV-XIX [21], Fe XVI [32], Fe XVII [28, 33–37], Fe XVIII-XXIV [38, 39], Fe XXI-XXIV [40], Fe XXIV [41, 42] and Fe XXI-XXIV [43]. In these works, many discrepancies between experimental results and theory have been found and are yet to be solved, such as the 3C/3D problem, that is going to be discussed later, and the iron plasma L-shell opacity discrepancies found in systematic measurements at stellar interior temperatures [44].

Several other studies have found that in some situations plasma models match better with astrophysical observations under the assumption that the currently known theoretical atomic data is not entirely correct and must be revised to achieve good results [27, 45]. Moreover, updated atomic data of the L-shell Fe may solve differences in models that are used to predict Fe abundance in low-temperature elliptical galaxies [46].

One notable example is the problem of the 3C/3D line ratio. Collisional excitation of the  $3d \rightarrow 2p$  and  $3s \rightarrow 2p$  transitions in Fe XVII produces the strongest lines observed in x-ray spectra. Such an example of the strongest Ne-like Fe lines are the, usually labeled as, 3C and 3D, defined by  $(2p_{1/2}^5 3d_{3/2})_{J=1} \rightarrow (2p^6)_{J=0}$  and  $(2p_{3/2}^5 3d_{5/2})_{J=1} \rightarrow (2p^6)_{J=0}$ , with energies around 826 eV and 812 eV. Both lines have low contribution from cascades and their intensity is almost only dependent on electron collisional excitation (CE) and dielectronic recombination (DR), processes which respective strength varies as a function of electron temperature and density, making the 3C/3D ratio a possible diagnostic tool [28]. However, the use of this tool has been hampered due to discrepancies between theoretical predictions and experimental observations [47–49]. Several EBIT experiments probing Ne-like Fe agreed with each other for the experimental value of 3C/3D, but all of them appear to deviate between 10 and 35% of the state-of-the-art theoretical predictions. In 2012, a novel x-ray spectroscopy measurement was performed at the LCLS free-electron laser facility [50]. A low value of 3C/3D oscillator-strength ratio was reported, reinforcing the mentioned discrepancy. One possible explanation for these results may have been an Na-like contamination which produces a so-called C line  $((2p_{3/2}^3 2p_{1/2} 3s 3d_{5/2})_{J=3/2} \rightarrow (2p^6 2s_{1/2})_{J=1/2})$  with an energy value close to the 3D line. A possible mixture of the C and 3D would result in an apparent lower ratio closer to the experimental results. This theory was recently disproved, as new measurements performed at the PETRA III synchrotron with the PolarX-EBIT had enough resolution to resolve both 3C, 3D and C lines and a lower 3C/3D ratio still persists [25]. The results from this reference paper are shown in figure 1.3, where a clear deviation is demonstrated between the old and newer calculations and all the recent experiments, as well as most astrophysical observations. These two examples show that atomic data for astrophysics needs experimental benchmark besides theoretical reverification.

Among the various atomic processes that lead to the x-ray emission of the previous cases, dielectronic recombination is an important process due to its high resonant strength. It is a recombination process, thus changing the charge state of the ion. As such, it plays an important role in charge state balance dynamics, that only depends on the possible ionization and recombination processes [51]. Furthermore, it produces x-ray emissions that closely accompany the main excitation lines. The dielectronic recombination (more details can be found in chapter 2) is a process where an ion captures a free electron in a resonant way, with a simultaneous excitation of a bound electron, leaving the ion in a doubly excited state. The excited ion may either autoionize or radiatively decay. The latter option concludes the DR process. For example, in the case of Fe XVII, DR-LMM means a resonant capture of an electron in the M-shell with an excitation of a

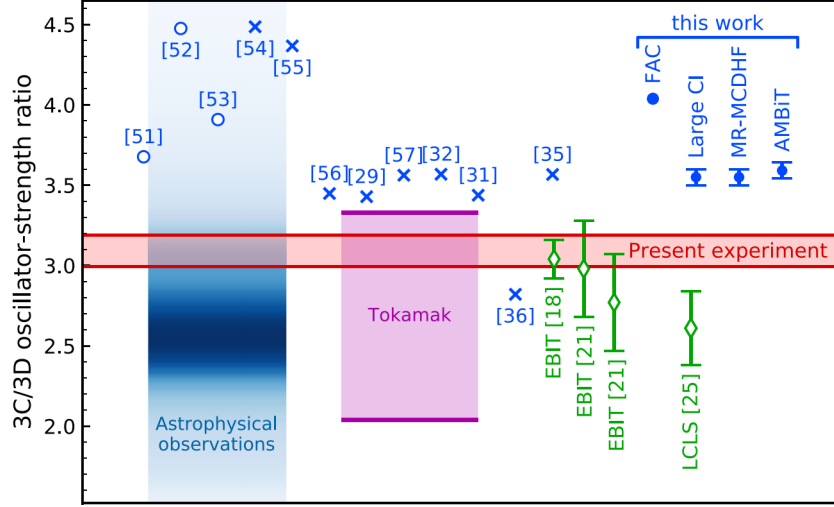
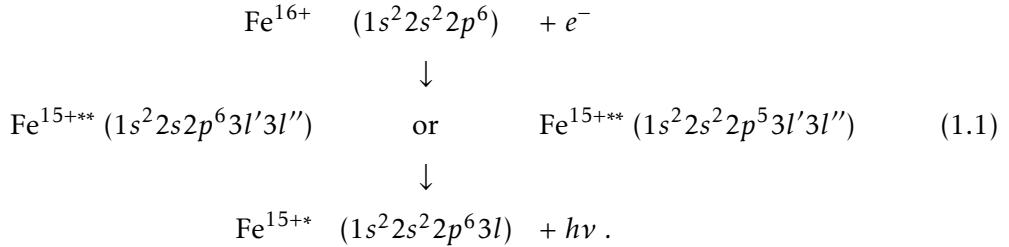


Figure 1.3: Experimental and theoretical (blue) values of the 3C/3D oscillation strength ratio for Fe XVII. The experimental values include astrophysical observations, tokamak measurements and experiments in several EBIT systems. The blue open circles represent the value from existing databases and blue crosses represent several past theoretical predictions. The blue closed circles represent the most recent calculations and the green diamonds represent EBIT experiments. Adapted from [25].

bound electron from the L-shell to the M-shell,



This process produces strong emissions that are close to the main Fe XVII LM lines, deviated only by the perturbation caused by the spectator electron (the electron that didn't decay in the last step of the DR process). Due to this proximity to the main lines, they are often referred to as satellite lines, since they always accompany the main excitation lines [52]. These type of lines have already been observed with Chandra in spectra from stellar coronae like Capella and Procyon and used for temperature diagnostics [53, 54]. The relative intensity of these lines depend on the temperature and electron density, and can also be used as plasma diagnostic tools. Thus, it is imperative to know the resonant strengths of this process accurately when using collision-radiative models, such as AtomDB [55] and SPEX [56], to diagnose temperatures. The atomic data used for such models can also be obtained in databases like CHIANTI [57] and OPEN-ADAS. Apart from DR  $3l5l'$  and  $3l6l'$  satellite lines for Fe XVII-XXIV [43], no laboratory measurements of wavelength and relative intensity of DR satellite lines are available [58]. Recently, DR cross sections for the  $3lnl'$  sequence were published with the intent to investigate

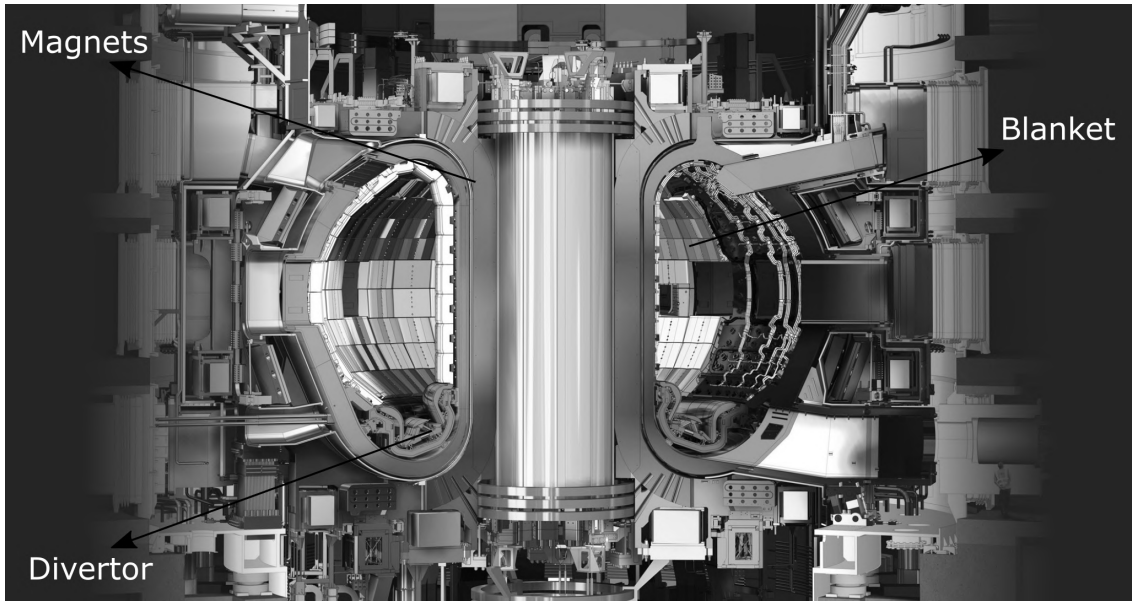


Figure 1.4: 3D model of the future International Thermonuclear Experimental Reactor (ITER). Adapted from [59].

$3d \rightarrow 2p$  and  $3s \rightarrow 2p$  line ratios above the collisions excitation threshold [37]. One of the main objectives of this thesis is to continue the investigation of the last reference, with an analysis of the data published in the last paper, with an emphasis on the DR-LMM structure. The extracted experimental values of the DR-LMMM structure were compared to new theoretical calculations performed with several codes and the values available in multiple databases. This study is given in chapter 4.

### 1.3.2 Fusion reactors

Besides investigating the details of astrophysical plasmas in laboratory, the tokamak are mainly design to study the feasibility of nuclear fusion as a promising source of clean energy [20]. In these plasmas, it is intended to promote a self-sustained fusion reaction between deuterium and tritium to produced energy. The International Tokamak Experimental Reactor (ITER) aims to achieve a steady state plasma with an output fusion energy of around ten times the heating energy required to maintain the reaction [60]. The design choice for the plasma-facing material for this device is tungsten (W), due to its high melting point, low sputtering yield, high-energy sputtering threshold and low tritium retention [52]. As W sputtering is expected, plasma diagnostic tools are being developed based on W HCl x-ray emissions, similar to the aforementioned astrophysical plasma diagnostic tools [61]. Several instruments will be used on ITER to observe W radiation to determine local plasma conditions. As such, there is a growing need for reliable highly charged tungsten emission experimental data as well as dependable ionization balance calculations.

Another element that can have an important role in the tokamak plasma is krypton

(Kr). Some calculations suggest that the neutral hydrogen losses are not large enough to limit the heat load on plasma facing materials [62], namely the divertor and blanket. Additional impurities are then needed to dissipate the heat at the borders of the plasma. One proposed element is Kr. It is expected that it can provide radiative cooling in the edge region at a rate of around 100 MW without perturbing the plasma core [63]. Some experiments of injection of Kr in tokamaks successfully yielded plasmas with lower electron density and temperature around the edges [64]. Furthermore, this element can also be used for x-ray diagnostics of the core region [64, 65]. The expected electron energy range of the region is between 10 and 30 keV. At these energies, the Kr is not fully stripped and K-shell transitions can be observed under high temperatures. Temperature diagnostics can work in a similar manner as the ones used in astrophysical plasmas. It is then important to understand all the atomic processes involving this element for several charge states to model the behaviour of the Kr plasma under the different temperature regimes. The cooling rates for the  $KL_n$  DR series and K-shell, L-shell and M-shell electron impact excitation have been measured in the past in EBIT systems [65, 66]. Within this thesis we explore new measurements of the DR-LMM structure of Kr XVII obtained in an EBIT system.

## 1.4 Organisation of the thesis

This thesis has the main objectives of providing theoretical and experimental atomic data important for the modeling and diagnostics of high-temperature plasmas, with an emphasis on measurements of dielectronic recombination cross sections and DR rate coefficients.

As stated before, there is a lack of experimental atomic data for Fe XVII. This thesis aims to continue the investigations made on Fe XVII in the 0.3 to 1.1 keV energy range with an EBIT (FLASH-EBIT, at Max-Planck-Institut für Kernphysik in Heidelberg [37]). The DR-LMM region, between 300 and 500 eV was analysed and compared with new calculation performed with several theoretical methods, which are described in chapter 2. New measurements made in another EBIT, namely Polar-X EBIT (details in chapter 3), were also analysed in this work. The latter are focused on the DR-LMM region and were made in a different scheme that allows the study of the charge state dynamics in the several electron beam energy conditions. Charge state simulations were also made to study the effects of the EBIT experimental conditions in the results. The extracted results were compared to old DR measurements made in the TSR, as well as theoretical values from several atomic databases.

Similarly, atomic data of Kr is also essential for fusion reactor plasma modeling and diagnostics. This work presents new measurements of Kr made on the FLASH-EBIT in the 400 to 2500 eV region. It is expected to observe the Kr XXVII DR  $LM_n$  series, as well as the direct impact excitation of the L-shell and M-shell.

This thesis is organized as follows:

- Chapter 2 describes the theoretical background to perform atomic structure calculations, as well as electron-ion collision processes. It begins by introducing the basic equation for one-electron systems and moves to the description of methods to compute the structure of multi-electron systems. It then makes a brief introduction to the collisional processes relevant to plasma charge state modeling, describing the principal processes of ionization and recombination. An introductory description of the angular distribution and polarization of the photons emitted in an EBIT is also presented.
- Chapter 3 describes the main components and general operation of an electron beam ion trap. The FLASH-EBIT and PolarX-EBIT characteristics and schemes of operation relevant to this work are then presented. A concise description of the TSR is also included.
- Chapter 4 details the theoretical atomic data calculations made in the course of this work. The application of these calculations to simulate the charge dynamics in the experimental conditions is also presented.
- Chapter 5 overviews the experimental analysis and comparison with theoretical calculations. It displays the final tabulated results of measured DR resonant strengths and respective DR rate coefficients of the Fe XVII DR-LMM structure. The measurements of Kr XXVII (Ne-like) are also briefly overviewed.
- Chapter 6 draws the conclusion regarding the calculations and analysis made in this work. It also discusses future prospects of this investigation.

## THEORY

In the following chapter, the theoretical framework underlying this work will be described in detail. Firstly, the basis of atomic structure calculations will be covered, starting with one-electron systems and evolving into multi-electron systems. Several types of methods to approximate solutions to the multi-electron system problems will be briefly presented. As it is an essential part of the dynamics of a plasma, the most relevant ion-electron collision processes will be described, as well as the mathematical framework to compute their respective cross section values. The charge exchange process will also be briefly covered due to its importance in electron beam ion traps. In the end of the chapter, the polarity and anisotropy of the photon emissions at an EBIT will be discussed.

In order to understand the behaviour of a hot plasma, it is required to know all the atomic processes present in the system as well as the atomic structure of the ions involved. As a plasma is composed essentially of ions and electrons, most of the present processes are based on ion-electron collisions. Some of these processes result in the emission of x-ray radiation, which is usually measured to probe the system. Processes such as recombination and ionization result in a change of the ion charge, thus resulting in dynamical charge state populations. The study of the charge state dynamics is essential to create a realistic model of the plasma and can help the understanding of several phenomena observed in the laboratory experiments. Apart from the DR process and radiative transitions, all the theory in this work will be presented in atomic units. More details about the theoretical descriptions can be found in [18, 27, 67–69].

Some widely used codes dedicated to the calculation of atomic energy structure and transition probabilities will be briefly presented in the end of the chapter.

## 2.1 Atomic structure

In order to obtain the atomic structure consisted of energy states and wavefunctions of a HCI, the Hamiltonian equation must be solved [68–70]:

$$H\Psi = E\Psi, \quad (2.1)$$

where  $H$ ,  $\Psi$  and  $E$  are the Hamiltonian, wavefunction and energy of a bound state. Since HCI atomic systems are usually subjected to relativistic effects, due to the high Coulomb field, it is necessary to solve the previous equation with the fully relativistic Dirac-Coulomb Hamiltonian [71]. For  $N$  electrons, the Hamiltonian is

$$H = \sum_i^N h_i + \sum_{i<j}^N V_{ij}^{e-e}, \quad (2.2)$$

where  $V_{ij}^{e-e}$  are all the electron-electron interaction potentials that include both Coulomb and Breit interaction. The Dirac-Coulomb Hamiltonian of a single electron is given by

$$h_i = c\boldsymbol{\alpha} \cdot \mathbf{p} + \beta c^2 + V_C(r_i), \quad (2.3)$$

where  $c$  is the light speed,  $\mathbf{p}$  is the linear momentum operator,  $V_C(r)$  is the nuclear Coulomb radial potential and  $\boldsymbol{\alpha}$  and  $\beta$  are the Dirac  $4 \times 4$  matrices

$$\boldsymbol{\alpha} = \begin{pmatrix} 0 & \boldsymbol{\sigma} \\ \boldsymbol{\sigma} & 0 \end{pmatrix} \quad \text{and} \quad \beta = \begin{pmatrix} 1 & 0 \\ 0 & -1 \end{pmatrix}, \quad (2.4)$$

where  $\boldsymbol{\sigma}$  are the Pauli spin matrices.

### 2.1.1 One-electron systems

For one-electron systems, the equation (2.1) is reduced to

$$\left[ c\boldsymbol{\alpha} \cdot \mathbf{p} + \beta c^2 + V_C(r) \right] \Psi_{n\kappa} = E_n \Psi_{n\kappa}. \quad (2.5)$$

This equation has analytical solutions in the form of

$$\phi_{n\kappa m}(r, \hat{r}) = \frac{1}{r} \begin{pmatrix} iP_{n\kappa}(r)\chi_{\kappa m}(\hat{r}) \\ Q_{n\kappa}(r)\chi_{-\kappa m}(\hat{r}) \end{pmatrix}. \quad (2.6)$$

These solutions are known as the Dirac spinors. Here,  $n$  is the principal quantum number,  $m$  is the z-component of the total angular momentum  $j$  and  $\kappa$  is the relativistic angular momentum, related to the orbital (gls) and total angular momentum by  $\kappa = (l - j)(2j + 1)$ . The quantities  $r$  and  $\hat{r}$  represent the the electron radius and unitary position vector, both in spherical coordinates. The function  $\chi_{\kappa m}(r)$  is the spherical spinor consisting of angular coupling of spherical harmonics and  $1/2$ -spinors. The radial functions  $P_{n\kappa}(r)$  and  $Q_{n\kappa}(r)$  are the two components of the relativistic radial wavefunction, usually referred to as the large and small components. By inserting the solution (2.6) in the equation (2.5), one can



obtain the radial coupled functions  $P_{n\kappa}(r)$  and  $Q_{n\kappa}(r)$  by solving the resulting coupled differential equations [67, 69]

$$\left(V_C(r) + c^2\right)P_{n\kappa}(r) + c\left(\frac{d}{dr} - \frac{\kappa}{r}\right)Q_{n\kappa}(r) = E_n P_{n\kappa}(r), \quad (2.7)$$

$$-c\left(\frac{d}{dr} - \frac{\kappa}{r}\right)P_{n\kappa}(r) + \left(V_C(r) - c^2\right)Q_{n\kappa}(r) = E_n Q_{n\kappa}(r), \quad (2.8)$$

where  $E$  is the energy eigenvalue corresponding to the  $P_{n\kappa}(r)(r)$  and  $Q_{n\kappa}(r)(r)$  eigenfunctions. While these equations have an analytical solution for a Coulomb potential, for most cases of other potentials, such as finite nuclear size, numerical methods are required, such as Numerov method [67] or finite basis set [72, 73].

### 2.1.2 Multi-electron systems

With the introduction of one or more electrons, the Hamiltonian equation becomes a three-body problem with no known analytical solutions in both classical and quantum physics. Although the angular part of the solutions is analytical due to the spherical symmetry of the atomic system, the radial part can only be obtained numerically. Many procedures have been employed over the years for solving the radial solutions of each electron and the composed  $N$ -electron wavefunction, which ones mentioned in this work are described bellow.

The simplest way to approximate the solutions is to consider an independent-particle model, where the electron-electron interaction potentials are replaced by a central potential in which the electrons move independently [18, 69], i.e.

$$\sum_{i \neq j} V_{ij}^{e-e} \sim V_i^C(r). \quad (2.9)$$

This potential can be defined to mimic the screening of the nucleus electrostatic attraction by the rest of the electrons. In this model, the atomic wavefunction  $\Psi$  is the product of  $N$  atomic orbitals  $\psi_i$  that are solution of the single electron  $N$  equations

$$\left[h_i + V_i^C(r)\right]\psi_i = \epsilon_i \psi_i, \quad (2.10)$$

where  $\epsilon_i$  is an eigenvalue of the eigenfunction  $\psi_i$ . These equations are simply the equation (2.5) with the addition screening central potential. The form of this screening potential depends upon the individual orbitals. In these cases, the potential is updated after the calculation of initial trial orbitals, which can be one-electron orbitals from previous section 2.1.1 or Thomas-Fermi orbitals [69], and the procedure is repeated iteratively. This is known as a self-consistent-field procedure.

### 2.1.3 Hartree-Fock method

A better approximation can be obtained by applying the variational principle to equation (2.1). A first approximation is taken by defining a trial wavefunction as

$$\Phi^S(r_1, \dots, r_N) = (N!)^{-1/2} \begin{vmatrix} \phi_{(n\kappa m)1}(r_1) & \cdots & \phi_{(n\kappa m)1}(r_N) \\ \vdots & \ddots & \vdots \\ \phi_{(n\kappa m)N}(r_1) & \cdots & \phi_{(n\kappa m)N}(r_N) \end{vmatrix}, \quad (2.11)$$

where  $r_i$  is the electron space coordinates  $(r, \hat{r})$  and  $\phi(r_i)$  are Dirac spinors defined in (2.6). The function, known as the Slater determinant, is totally antisymmetric and independent of the ordering of the labels  $i$ , therefore ensuring that the Pauli exclusion principle is obeyed. According to the variational principle, the Slater determinant that best describes the system is such that the energy expectation value is stationary in regard to small variations of the radial part of the orbitals  $\phi_i$  [18],

$$\delta \left\langle \Phi^S(r_1, \dots, r_N) \left| \sum_i^N h_i + \sum_{i < j}^N V_{ij}^{e-e} \right| \Phi^S(r_1, \dots, r_N) \right\rangle = 0. \quad (2.12)$$

This leads to the Hartree-Fock equations [74] (Dirac-Fock for the relativistic case), a system of  $N$  nonhomogeneous coupled integro-differential equations that can be solved iteratively in a self-consistent-field manner. This method takes into account the electron correlation within an electron configuration.

### 2.1.4 Configuration Interaction

A better approximation can be made by considering the interaction between configurations. The Configuration State Function (CSF) for an  $N$  electron atomic system is defined as a mixture of Slater determinants,

$$\Phi(r_1, \dots, r_N) = \sum_i d_i \begin{vmatrix} \phi_{(n\kappa m)1}(r_1) & \cdots & \phi_{(n\kappa m)1}(r_N) \\ \vdots & \ddots & \vdots \\ \phi_{(n\kappa m)N}(r_1) & \cdots & \phi_{(n\kappa m)N}(r_N) \end{vmatrix}, \quad (2.13)$$

where  $d_i$  are coefficients determined by imposing that the  $\Phi$  remains an eigenfunction of the operators  $\hat{J}_z$  and  $\hat{J}^2$ . To include correlation effects between the configurations, a final atomic state can be obtained by a linear combination of configuration state functions,

$$\Psi = \sum_k c_k \Phi_k(r_1, \dots, r_N), \quad (2.14)$$

where  $c_k$  are the configuration mixing coefficients. In this case, the atomic wavefunction is given by a superposition of CSFs. These coefficients can be determined with several methods, namely the multiconfiguration Dirac-Fock, where a variational method is applied (explained in 2.1.5). The inclusion of multiple configurations in the same atomic

wavefunction, extending the total wavefunction to reflect electron correlation between configuration, leads to the method known as Configuration Interaction (CI). A complete basis of CSFs cannot be used, as the total number of possible configuration states grows to infinity. Assuming a combination of a finite number of configurations, an arbitrary level of accuracy can be achieved by adding more configuration state functions into the mixture [18].

### 2.1.5 Multiconfiguration Dirac-Fock

The use of the CI wavefunction as a trial function in the Hartree-Fock and Dirac-Fock methods leads to the Multiconfiguration Hartree-Fock (MCHF) and Multiconfiguration Dirac-Fock (MCDF) methods. The total energy of the atomic wavefunction is given by

$$E = \frac{\langle \Psi | H | \Psi \rangle}{\langle \Psi | \Psi \rangle}. \quad (2.15)$$

Using the variational method, the CI wavefunction that better describes the system is such that the energy of the system is stationary in regard to small variations of the mixing coefficients  $c_k$  defined in the equation (2.14), i.e.

$$\frac{\partial \langle \Psi | H | \Psi \rangle}{\partial c_k \langle \Psi | \Psi \rangle} = 0. \quad (2.16)$$

The minimization of this quantity determines the atomic wavefunction that better approximates the system in the configuration basis chosen for the calculation. The result can be improved by increasing the number of configuration states included in the atomic wave function. For a given set of mixing coefficients, the system energy is evaluated using the standard Hartree-Fock or Dirac-Fock methods. In the MCDF case, the radial Dirac-Fock equations are obtained by minimizing the energy variation in respect to small variations of radial functions  $P_{n\kappa}(r)$  and  $Q_{n\kappa}(r)$

$$\frac{\partial (E[H] - \sum_{ij} \varepsilon_{ij} \langle \phi_i | \phi_j \rangle)}{\partial P_{n\kappa}(r)}, \quad (2.17)$$

$$\frac{\partial (E[H] - \sum_{ij} \varepsilon_{ij} \langle \phi_i | \phi_j \rangle)}{\partial Q_{n\kappa}(r)}, \quad (2.18)$$

where  $\varepsilon_{ij}$  are the Lagrange parameters, introduced to insure the orthonormality of the wavefunction. The Dirac-Fock set of equations for a particular radial wavefunction ( $P_i, Q_i$ ) are given by

$$\frac{d}{dr} \begin{pmatrix} P_i(r) \\ Q_i(r) \end{pmatrix} = \begin{pmatrix} -\frac{\kappa_i}{r} & 2c + \frac{\varepsilon_{ij} - V_i(r)}{c} \\ -\frac{\varepsilon_{ij} - V_i(r)}{c} & \frac{\kappa_i}{r} \end{pmatrix} \begin{pmatrix} P_i(r) \\ Q_i(r) \end{pmatrix} + \begin{pmatrix} X_i^P(r) \\ X_i^Q(r) \end{pmatrix}, \quad (2.19)$$

where  $V_i(r)$  is the sum of the nuclear potential with the direct part of the Coulomb repulsion and  $X_i^P$  or  $X_i^Q(r)$  are the generalized exchange potentials.

### 2.1.6 Many Body Perturbation Theory

An alternate approach to the variational principle is the use of perturbation theory. The Many Body Perturbation Theory (MBPT) [18] treats the single electron Hamiltonian as the unperturbed state and the electron-electron interactions as a perturbation. To make this approximation, the hamiltonian in the equation (2.2) is expanded in the form

$$H = H_0 + H_{\text{pert}}, \quad (2.20)$$

where  $H_0$  is defined by

$$H_0 = \sum_i^N h_i + V_i^C(r) \quad (2.21)$$

and

$$H_{\text{pert}} = \sum_{i<j}^N V_{ij}^{e-e} - \sum_i^N V_i^C(r). \quad (2.22)$$

Here, the unperturbed sates can be calculated beforehand with several methods, like the ones presented in 2.1.2 and 2.1.3. Let  $\Psi$  be the eigenstate of the Hamiltonian  $H$  with a corresponding eigenvalue  $E$ . The eigenstate can be decomposed into a unperturbed wavefunction  $\Psi^{(0)}$  that satisfies

$$H_0\Psi^{(0)} = E^0\Psi^{(0)} \quad (2.23)$$

and a perturbation  $\Delta\Psi$ . The resulting wavefunction is normalized by the intermediate normalization contidition  $\langle\Psi^0|\Psi\rangle = 1$ . If  $\Psi = \Psi^{(0)} + \Delta\Psi$  and  $E = E^0 + \Delta E$ , the eigenvalue equation of the problem may be rewritten as

$$(H^0 - E^0)\Delta\Psi = (\Delta E - H_{\text{pert}})\Psi. \quad (2.24)$$

From this equations follows that

$$\Delta E = \langle\Psi^0|H_{\text{pert}}|\Psi\rangle. \quad (2.25)$$

By expanding the wavefunction and the respective energy in the forms

$$\begin{aligned} \Psi &= \Psi^{(0)} + \Delta\Psi = \Psi^{(0)} + \Psi^{(1)} + \Psi^{(2)} + \dots, \\ E &= E^{(0)} + \Delta E = E^{(0)} + E^{(1)} + E^{(2)} + \dots, \end{aligned} \quad (2.26)$$

where  $\Delta\Psi$  and  $\Delta E$  are the wavefunction and energy corrections to the unperturbed system, the equation (2.1) can be expended in a set of inhomogeneous equations with the form of [69]

$$\begin{aligned} (H^{(0)} - E^{(0)})\Psi^{(1)} &= (E^{(1)} - H_{\text{pert}})\Psi^{(0)}, \\ (H^{(0)} - E^{(0)})\Psi^{(2)} &= (E^{(1)} - H_{\text{pert}})\Psi^{(1)} - E^{(1)}\Psi^{(0)}, \\ (H^{(0)} - E^{(0)})\Psi^{(3)} &= (E^{(1)} - H_{\text{pert}})\Psi^{(2)} - E^{(2)}\Psi^{(2)} - E^{(3)}\Psi^{(0)}, \\ &\vdots \end{aligned} \quad (2.27)$$

The indices of the correction terms indicate the correction order of the wavefunction and energy. These equations can be solved progressively to achieve a perturbation correction to any arbitrary order. Each order of the correction has a smaller impact on the overall correction value. The complexity of the solutions grows with the order of the equation, so the corrections to the wavefunctions and energies are usually made to the first or second order, depending on the application and accuracy requirements. As an example for a non degenerate system, the first order correction of the energy is given by

$$E^{(1)} = \langle \Psi_0 | H_{\text{pert}} | \Psi_0 \rangle, \quad (2.28)$$

while the first order of the wave function correction is given by

$$|\Psi^{(1)}\rangle = - \sum_{k \neq n} \frac{\langle \Psi_k^{(0)} | H_{\text{pert}} | \Psi_n^{(0)} \rangle}{E_k^{(0)} - E_n^{(0)}} |\Psi_k^{(0)}\rangle. \quad (2.29)$$

Here, the indices  $k$  and  $n$  indicate distinct atomic states. The first correction of the wavefunction is defined as a linear combination of the rest of the wavefunctions of the system. Although this is an infinite series, the energy difference between states in the denominator ensures that it converges, and a finite, sufficiently high, number of atomic states can be used to make a good approximation.

### 2.1.7 Continuum atomic wavefunction

Calculations of atomic processes involving electrons in the continuum, like ionization and recombination processes, require the knowledge of the atomic continuum state functions, defined as

$$\Psi^c(\varepsilon) = \sum_k \Phi_k(r_1, \dots, r_N) \phi_k^f(\varepsilon), \quad (2.30)$$

where  $\varepsilon$  is the free electron energy,  $\phi_k^f$  are the free electron orbitals and  $\chi_k$  are the atomic state wavefunctions. The free electron orbitals are solutions of the Dirac equations

$$[h_\alpha^K + \varepsilon] \phi_\alpha^f = \sum_{\alpha'} U_{\alpha\alpha'} \phi_{\alpha'}^f. \quad (2.31)$$

The quantity  $h_\alpha^K$  are the one-electron kinetic hamiltonians. The matrix potential  $U_{\alpha\alpha'}$  is defined by

$$U_{\alpha\alpha'} = \int dr_1 \dots dr_N \Phi_\alpha(r_1 \dots r_N) U(r_1 \dots r_N r_{N+1}) \Phi_{\alpha'}(r_1 \dots r_N), \quad (2.32)$$

where  $U$  is the sum of nuclear and electron-electron potentials acting on the  $N + 1$  electrons of the target-plus-free-electron system. Neglecting the interaction between different bound states, and consequently different continuum states

$$U_{\alpha\alpha'} = 0, \quad \alpha \neq \alpha', \quad (2.33)$$

gives the widely used Distorted Wave (DW) [18] approximation is obtained. This way, the set of equations (2.31) become decoupled and can be solved with previously mentioned methods, such as the central field approximation.

## 2.2 Decay processes

Once an atom is in an excited state, it can decay either radiatively, via photon emission, or decay non radiatively, via auger electron emission. The rate of decay for both processes is important to fully describe processes with an excited intermediate state, like dielectronic recombination, collisional excitation and excitation with subsequent autoionization.

### 2.2.1 Radiative decay

An atomic system can absorb or emit radiation, usually causing transitions of electrons between atomic states in such a way that the total energy of the system is conserved. These situations can be studied by analysing the interaction between an atom and the radiation and the time evolution of the system. To be composed of electromagnetic plane waves, radiation propagating in the direction  $\hat{k}$  is described by the transverse-gauge vector potential [69]

$$\mathbf{A}_{\pm}(\mathbf{r}, \omega) = \hat{\epsilon}_{\lambda} e^{\pm i\mathbf{k}\cdot\mathbf{r}}, \quad (2.34)$$

where  $\omega$ ,  $\hat{\epsilon}$  and  $\mathbf{k}$  are the radiation frequency, the polarization vector and the propagation vector, respectively. The polarization vector describes the direction of the electric field of the plane wave. The vector potential and the propagation potential are always orthogonal.  $\hat{\epsilon}_{\lambda}$  represent the two unit vector orthogonal between each other and with the propagation vector ( $\lambda = \pm 1$ ). The general solution to the time-dependent wave equation in the transverse gauge is a superposition of plane wavefunctions in the form

$$\mathbf{A}(\mathbf{r}, t) = \sum_i \left( c_i \hat{\epsilon}_{\lambda} e^{i\mathbf{k}\cdot\mathbf{r} - i\omega t} + c_i^* \hat{\epsilon}_{\lambda}^* e^{-i\mathbf{k}\cdot\mathbf{r} + i\omega t} \right), \quad (2.35)$$

where  $i$  is the set of parameters  $(\omega, \hat{k}, \hat{\epsilon}_{\lambda})$  and  $c_i$  are the Fourier expansion coefficients.

By considering a closed box of volume  $V$ , the number of possible vectors  $\mathbf{k}$  that allow the electromagnetic field to respect certain boundary conditions on the surface of the box is finite. If the coefficients  $c_i$  and  $c_i^*$  are interpreted as quantum mechanical operators, the electromagnetic field becomes quantized. This way a photon is described by the operator

$$\mathbf{A}_i(\mathbf{r}, t) = \sqrt{\frac{\hbar}{2\epsilon_0\omega V}} \left( c_i \hat{\epsilon}_{\lambda} e^{i\mathbf{k}\cdot\mathbf{r} - i\omega t} + c_i^{\dagger} \hat{\epsilon}_{\lambda}^* e^{-i\mathbf{k}\cdot\mathbf{r} + i\omega t} \right). \quad (2.36)$$

The coefficients  $c_i$  and  $c_i^{\dagger}$  are the photon annihilation and creation operators. The coefficient of the equation permits the energy of the radiation to be expressed in terms of the number of photons. Similarly to (2.35), the general expression for the vector potential is a superposition of the photon potentials (2.36),

$$\mathbf{A}(\mathbf{r}, t) = \sum_i \mathbf{A}_i(\mathbf{r}, t). \quad (2.37)$$

The Hamiltonian of the electromagnetic field is given by [69]

$$\begin{aligned} H_{EM} &= \frac{\epsilon_0}{2} \int d^3r \mathbf{E}(\mathbf{r}, \mathbf{t}) \cdot \mathbf{E}(\mathbf{r}, \mathbf{t}) + \frac{1}{2\mu_0} \int d^3r \mathbf{B}(\mathbf{r}, \mathbf{t}) \cdot \mathbf{B}(\mathbf{r}, \mathbf{t}) \\ &= \sum_i \hbar\omega \left( \mathcal{N}_i + \frac{1}{2} \right), \end{aligned} \quad (2.38)$$

where  $\mathcal{N}_i = c_i^\dagger c_i$  is the photon number operator. With this relation, one can show that the vacuum state is an eigenstate of  $H_{EM}$  with energy

$$E_0 = \frac{1}{2} \sum_i \hbar\omega_i. \quad (2.39)$$

This energy is referred to as the *zero-point energy* of the electromagnetic field. Since it is not measurable, the electromagnetic field Hamiltonian is modified to be

$$H_{EM} = \sum_i \hbar\omega \mathcal{N}_i. \quad (2.40)$$

The interaction between an electron and an external electromagnetic field is given by

$$\begin{aligned} h_I(\mathbf{r}, t) &= -ec\boldsymbol{\alpha} \cdot \mathbf{A}(\mathbf{r}, t) \\ &= \sum_i \left[ h_I(\mathbf{r}, \omega) c_i e^{-i\omega t} + h_I^\dagger(\mathbf{r}, \omega) c_i^\dagger e^{i\omega t} \right], \end{aligned} \quad (2.41)$$

with

$$h_I(\mathbf{r}, \omega) = -ec \sqrt{\frac{\hbar}{2\epsilon_0\omega V}} \boldsymbol{\alpha} \cdot \hat{\epsilon}_\lambda e^{i\mathbf{k}\cdot\mathbf{r}}, \quad (2.42)$$

where  $e$  is the fundamental charge constant and  $c$  is the speed of light. The many-electron interaction Hamiltonian in the Heisenberg representation becomes

$$H_I(t) = \sum_k \left[ H_I(\omega) c_k e^{-i\omega t} + H_I^\dagger(\omega) c_k^\dagger e^{i\omega t} \right], \quad (2.43)$$

where  $H_I(\omega)$  is the sum of  $N$  one-electron terms,

$$H_I(\omega) = \sum_{i=1}^N h_i(\mathbf{r}, \omega). \quad (2.44)$$

To study the time evolution of a system composed of an atom and an external electromagnetic field, one must consider the effect of adding the interaction Hamiltonian to the sum of the many-electron Hamiltonian  $H_0 + V_I$  and the electromagnetic Hamiltonian  $H_{EM}$ . The eigenvalue equations of the last two Hamiltonians are

$$(H_0 + V_I)\Psi_k = E_k\Psi_k \quad (2.45)$$

and

$$H_{EM}|n_k\rangle = n_k\hbar\omega|n_k\rangle. \quad (2.46)$$

$\Psi_k$  and  $E_k$  are the eigenfunctions and eigenvalues of  $H_0 + V_I$ , while  $|n_k\rangle$  and  $n_k$  are the eigenfunctions and eigenvalues of  $H_{EM}$ . If the total hamiltonian is represented by  $H = H_0 + V_I + H_{EM}$ , the eigenfunctions of  $H$  are given by

$$\Phi_k = \Psi_k |n_k\rangle, \quad (2.47)$$

with eigenvalues  $E_k + n_k \hbar \omega$ . Let  $S$  be the unitary operator that transforms states prepared at  $t = -\infty$ , when there is no interaction of the form  $H_I(t)$ , into states in the time  $t = \infty$ , where the interaction is once again assumed to vanish. This operator is expressed as  $S = U(-\infty, \infty)$ . It becomes

$$S = I + \sum_{n=1}^{\infty} S^{(n)}, \quad (2.48)$$

where

$$S^{(n)} = \frac{(-i)^n}{\hbar^n} \int_{-\infty}^{\infty} dt_1 \hat{H}_I(t_1) \int_{-\infty}^{\infty} dt_2 \hat{H}_I(t_2) \dots \int_{-\infty}^{\infty} dt_n \hat{H}_I(t_n). \quad (2.49)$$

and  $I$  is the identity matrix.

By retaining only the first order in  $H_I$  ( $n = 1$ ), the transition amplitude for a state  $\Phi_i$  in the past to evolve into the state  $\Phi_f$  in the future is given by

$$\begin{aligned} S_{fi}^{(1)} &= \langle \Phi_f | S^{(1)} | \Phi_i \rangle \\ &= -\frac{i}{\hbar} \int_{-\infty}^{\infty} dt \langle \Phi_f | \hat{H}_I(t) | \Phi_i \rangle. \end{aligned} \quad (2.50)$$

The probability of transition from the initial to the final stationary state is given by the square of  $S_{fi}^{(1)}$ . The transition probability per unit time can be evaluated for both emission and absorption of a photon to give

$$W_{fi} = \frac{2\pi}{\hbar} |T_{fi}|^2 \begin{pmatrix} n_i \\ n_i + 1 \end{pmatrix} \delta(E_f - E_i \mp \hbar \omega), \quad (2.51)$$

where  $|T_{fi}|^2$  is the transition amplitude is defined by

$$T_{fi} = \begin{cases} \langle \Psi_f | H_I | \Psi_i \rangle, & \text{for absorption of a photon} \\ \langle \Psi_f | H_I^\dagger | \Psi_i \rangle, & \text{for emission of a photon} \end{cases}. \quad (2.52)$$

The interaction Hamiltonian depends on  $e^{\mathbf{k} \cdot \mathbf{r}}$ . Since  $\mathbf{k} \cdot \mathbf{r} \ll 1$ , this quantity can be approximated as  $e^{\mathbf{k} \cdot \mathbf{r}} = 1 + i(\mathbf{k} \cdot \mathbf{r}) + \dots$ , where each term refers to a different multipole approximation of the electromagnetic field (e.g. taking the first order approximation  $e^{\mathbf{k} \cdot \mathbf{r}} \approx 1$  leads to the electric dipole transition, while taking the next approximation  $e^{\mathbf{k} \cdot \mathbf{r}} \approx 1 + i(\mathbf{k} \cdot \mathbf{r})$  leads to the magnetic dipole transition). For this reason, this operator is sometimes referred to as the multipole operator. In this thesis, the multipole operator of the order  $L$  will be referred to as  $O^L$ .

In a given interval of wave numbers  $d^3k$ , the number of photons of a particular polarization is

$$d^3n_i = \frac{V}{(2\pi)^3} d^3k = \frac{V}{(2\pi c)^3} \omega^2 d\omega d\Omega_k \quad (2.53)$$



where  $\Omega_k$  represents a solid angle in the wave number space. The number of transitions per second for this interval of wave number can be evaluated by the relation  $d^3w_{fi} = W_{fi}d^3n_i$ . By integrating over  $\omega$ , and considering that the spectral density can be defined as  $\rho(\omega) = \hbar\omega^3/\pi^2c^3$ , the photon emission probability per second of an excited state  $\Psi_i$  into a lower energy state  $\Psi_f$  can be defined as [69]

$$A_{if}^{r_{total}} = \left(1 + \frac{\pi^2c^3}{\hbar\omega^3}\rho(\omega)\right) \frac{\alpha}{2\pi} \sum_{\lambda} \int d\Omega_k |T_{fi}|^2. \quad (2.54)$$

From this equation, it is apparent that that only one of the two terms depends on the spectral density (stimulated emission). As such, the spontaneous emission (emission without the need for a prior spectral density) rate is

$$A_{if}^r = \frac{\alpha}{2\pi} \sum_{\lambda} \int d\Omega_k |T_{fi}|^2. \quad (2.55)$$

In the electric dipole approximation, where  $e^{i\mathbf{k}\cdot\mathbf{r}} \approx 1$ , the transition amplitude is given by

$$T_{fi} = \langle \Psi_f(\mathbf{r}) | \boldsymbol{\alpha} \cdot \hat{\boldsymbol{\epsilon}} | \Psi_i(\mathbf{r}) \rangle. \quad (2.56)$$

This quantity can also be expressed as

$$T_{fi} = i \frac{\omega_{fi}}{c} \langle \Psi_f(\mathbf{r}) | \mathbf{r} | \Psi_i(\mathbf{r}) \rangle \cdot \hat{\boldsymbol{\epsilon}}, \quad (2.57)$$

with

$$\omega_{fi} = \frac{W_f - W_i}{\hbar}. \quad (2.58)$$

Here, the quantity  $W = E - c^2$  in atomic units, where  $E$  is the energy of a state given by the Dirac equation.

### 2.2.2 Auger decay

If the transition energy of an excited electron surpasses the binding energy of another bound electron, the excited one can decay with the ejection of the other electron without the emission of radiation. The ejected electron is known as an Auger electron. Analogously to the radiate decay, the auger (or autoionization) decay rate can be expressed as [67]

$$A_{if}^a = 2 \sum_{\kappa} \left| \langle \Psi_f, \kappa; J_T M_T | \sum_{k<l} \frac{1}{r_{kl}} | \Psi_i \rangle \right|^2, \quad (2.59)$$

where  $\Psi_i$  and  $\Psi_f$  are the excited state and the final state with one less electron, respectively, and  $\kappa$  is the total relativistic angular momentum. The time inversed process is the dielectronic capture, where a free electron recombines with an ion with simultaneous excitation of another bound electron. The resonant strength (integral of the cross section) of this process, given in atomic units, is defined as

$$S^{DC} = \frac{g_i}{2g_f} \frac{\pi^2}{E_{if}} A_{if}^a, \quad (2.60)$$

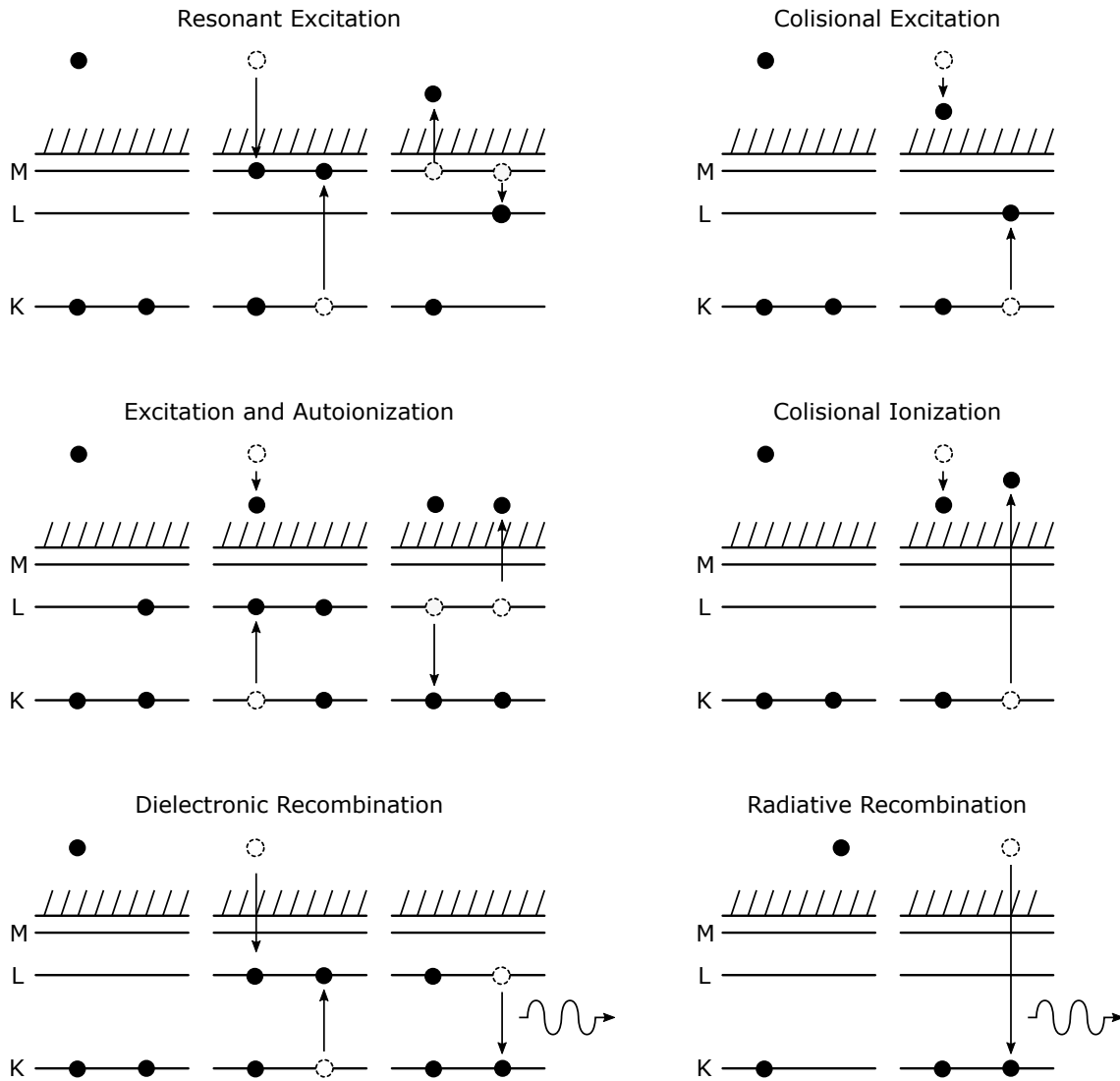


Figure 2.1: Schematic of several atomic processes: collisional and resonant excitation, excitation and autoionization, collisional ionization, dielectronic recombination and radiative recombination. In every individual scheme, each horizontal line represents an atomic shell (K, L and M) below the continuum threshold. The black dots represent an electron (free if above the continuum threshold) and the curvy line represents a photon. Every scheme is represented in either 2 or 3 moments in time and the circles with a dotted outline represent the previous position of an electron.

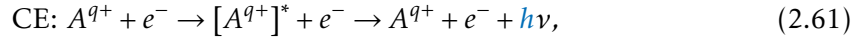
where  $g_i$  and  $g_f$  are the statistical weights of the initial and final states, given by  $g = 2J + 1$ , and  $E_{if}$  is the resonant energy.

### 2.3 Electron-ion collision processes

The most important electron-ion collisional processes are represented in figure 2.1.

### 2.3.1 Collisional excitation and ionization

Some of the most common processes in collisions of HCl with electrons are the collisional excitation (CE) and collisional ionization (CI) processes. The process of excitation take place when the kinetic energy of an incident electron is above the required threshold energy to excite the ion. If the kinetic energy is transferred to the ion, it becomes excited and can stabilize by either emitting a photon, or cascade of photons, or by emitting an electron through an Auger process. Schematically, the first case is described as



where  $A^{q+}$  denotes an ion of charge  $q+$ ,  $e^{-}$  represents a free electron,  $h\nu$  a photon and the superscript  $*$  denotes an excited state. The cross section of CE,  $\sigma_{CE}$ , with the collisional excitation from an initial state  $\Psi_0$  to a final state  $\Psi_1$  is related to the quantity collisional strength  $\Omega_{01}$  by [75]

$$\sigma_{CE} = \frac{\pi}{k_0^2 g_0} \Omega_{01}, \quad (2.62)$$

where  $g_0$  is the statistical weight of the initial state,  $k_0$  is the kinetic momentum of the incident electron, related to its kinetic energy  $\varepsilon_0$  by

$$k_0^2 = 2\varepsilon_0 \left( 1 + \frac{\alpha^2}{2} \varepsilon_0 \right), \quad (2.63)$$

with  $\alpha$  corresponding to the fine structure constant. Being the  $J_T$  and  $M_T$  as the total angular momentum and its z-projection when the target state is coupled to the continuum orbital, the collisional strength is written as

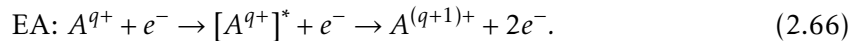
$$\Omega_{01} = 2 \sum_{\kappa_0 \kappa_1} \sum_{J_T} (2J_T + 1) \left| \langle \Psi_0^c(\varepsilon_0) \kappa_0, J_T M_T | \sum_{i < j} \frac{1}{r_{ij}} | \Psi_1^c(\varepsilon_1) \kappa_1, J_T M_T \rangle \right|^2. \quad (2.64)$$

Since the excited state has both the possibility to decay to a lower energy state or autoionize, the cross section associated to the process described in (2.61) must take into account the probability of radiative decay rather than Auger transition. The final cross section of CE from a state 0 into a state 1, leading to a radiative transition from state 1 to state 2 is

$$\sigma_{CE'}^{0 \rightarrow 2} = \sigma_{CE}^{0 \rightarrow 1} \frac{A_{12}^r}{\sum_f A_{1f}^r + \sum_{f'} A_{1f'}^a}, \quad (2.65)$$

where  $f$  and  $f'$  represent all the possible states to where the electron in the state 1 can decay into.

In the case of a subsequent Auger decay (EA), the process is represented by

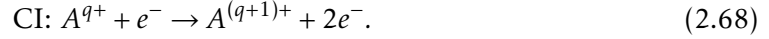


This process leads to a variation of charge state that can be much greater than direct CI and thus must be taken into account when modeling a plasma. Similarly to the previous

case, the EA cross section can be defined as

$$\sigma_{EA}^{0 \rightarrow 2} = \sigma_{CE}^{0 \rightarrow 1} \frac{A_{12}^a}{\sum_f A_{1f}^r + \sum_{f'} A_{1f'}^a}. \quad (2.67)$$

If the kinetic energy of the incident electron surpasses the binding energy of a bound electron, the ion might be ionized in the collision, leading to the CI process



This process can be calculated by an expression analogous to the equation (2.64), where the final state wavefunction is substituted with the continuum atomic wavefunction with the ejected electron in the DW approximation. The cross section of this process for few-electron ion systems can be estimated with the semi-empirical Lotz formula [76], which has proven to be sufficiently accurate when compared to experimental results. For electron energies  $E_e$  much larger than the binding energy  $P_i$  of an electron within the suborbital  $i$ , the Lotz formula is

$$\sigma_i = a_i q_i \frac{\ln(E_e/P_i)}{E_e/P_i}, \quad (2.69)$$

where  $a_i = 4.5 \times 10^{-14} \text{ cm}^2 \text{ eV}^2$  is an empirical constant and  $q_i$  is the number of equivalent electrons in the subshell  $i$ .

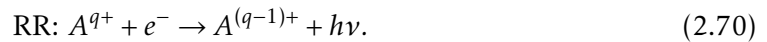
Both CI and EA processes have been studied for HCI in ion storage rings, such as the Test Storage Ring (TSR) in Heidelberg [47, 77, 78]. In multielectron systems, the EA can dominate the ionization process, particularly near the threshold of autoionizing states. TSR measurements and calculations of EA in this work are presented in chapter 4.

### 2.3.2 Electron-ion recombination

X-ray spectra of these systems are also dominated by structures originated by electron-ion recombination processes. These processes are divided in non resonant, namely radiative recombination (RR), and resonant, like the often mentioned DR.

#### 2.3.2.1 Radiative Recombination

The radiative recombination process is a non resonant process and can happen with any initial free electron with kinetic energy  $\varepsilon$ . A free electron can approach an ion and recombine in a state with binding energy  $E_b$ . As a result of the recombination, there is an emission of a photon with energy  $\omega = E_b + \varepsilon$  (conservation of energy principle),



Since this is a non resonant process, the resulting radiation can contribute to the background of the experimental spectra. The associated cross section  $\sigma_{RR}$  is related to the

photoionization (PI) cross section by the Milne relation [79],

$$\sigma_{RR} = \frac{\alpha^2}{2} \frac{g_i}{g_f} \frac{\omega^2}{\varepsilon(1 + \frac{1}{2}\alpha^2\varepsilon)} \sigma_{PI} \quad \text{and} \quad \sigma_{PI} = 2\pi\alpha \frac{df}{dE}. \quad (2.71)$$

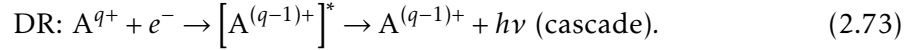
Here,  $g_i$  and  $g_f$  are statistical weights of the respective states,  $\omega$  is the photon energy in atomic units and  $\varepsilon$  is the energy of the free electron. The quantity  $df/dE$  is the differential oscillator strength and can be computed by

$$\frac{df}{dE} = \frac{\omega}{g_i} \frac{(\alpha\omega)^{2L-2}}{2L+1} \sum_{\kappa J_T} \left| \langle \Psi_f, \kappa; J_T | O^L | \Psi_i \rangle \right|^2. \quad (2.72)$$

The operator  $O^L$  is the multiple operator of rank  $L$  which induces the transition and  $\Psi_i$  and  $\Psi_f$  are the wavefunctions before and after the photoionization.

### 2.3.2.2 Dielectronic Recombination

The DR is a two-step process in which, similarly to the RR process, an incident electron recombines with an ion. A free electron is captured by an ion via a non radiative process with simultaneous excitation of a bound electron, leaving the ion in a doubly excited state. This can only happen when the kinetic energy of the incident electron equals the excitation energy of the bound electron, thus being a resonant process. Afterwards, the excited electrons can either decay radiatively or autoionize, the former corresponding to the DR process and the latter to the resonant excitation process (RE):



This process has a relatively high cross section and can dominate the spectra of these ion systems. It has an important role in the charge state balance and, with a good understanding of its underlying theory, can become an important diagnostic tool for astrophysical and fusion plasmas. It is usual to apply a nomenclature similar to the one found in the auger electron emission process to identify the DR process. It consists of three letters indicating the atomic shells where the bound electron belongs before and after the excitation and the shell where the free electron is captured, respectively. As an example, the KLL DR process corresponds to the capture of a free electron to the L-shell with an excitation of a bound electron from the K to the L-shell. This example is represented in figure 2.1.

The DR cross section can be expressed as [80]

$$\sigma_{idf}^{DR}(E_e) = \frac{\pi^2 \hbar^3}{m_e E_e} \frac{g_d}{2g_i} A_{di}^a \omega_{df} L_d(E_e), \quad (2.74)$$

where  $E_e$  is the free electron energy,  $A_{di}^a$  is the autoionization rate from an intermediate state  $d$  to an initial state  $i$ ,  $\omega_{df}$  is the fluorescence yield of the intermediate excited state  $d$  to a final state  $f$  and  $L_d(E_e)$  is the Lorentzian profile of the resonance. The quantities

$g_d$  and  $g_i$  are the statistical weights of the states after and before recombination. Here,  $J$  is the total angular momentum of a given state.

The Lorentzian profile is defined by

$$L_d(E_e) = \frac{\Gamma_d/2\pi}{(E_e - E_{id})^2 + \Gamma_d^2/4}, \quad (2.75)$$

where  $E_{id} = E_d - E_i$ .  $\Gamma_d$  is the width of the resonance, defined by the sum of all the possible autoionizing and radiative decays starting with the state  $d$ , i.e.  $\Gamma_d = \hbar \left( \sum_n A_{dn}^a + \sum_m A_{dm}^r \right)$ .

The fluorescence yield is given by

$$\omega_{df} = \frac{A_{df}^r}{\sum_n A_{dn}^a + \sum_m A_{dm}^r}, \quad (2.76)$$

where  $A_{df}^r$  is the rate of radiative decay between the states  $d$  and  $f$ . It determines the probability of decaying radiatively after a dielectronic capture.

The width of the resonance is often much smaller than the experimental width, so the Lorentzian profile can be approximated to a Dirac delta function  $\delta(E_e - E_{di})$ . With this in mind, the final cross section becomes

$$\begin{aligned} \sigma_{idf}^{DR}(E_e) &= \frac{\pi^2 \hbar^3}{m_e E_e} \frac{g_d}{2g_i} \frac{A_{di}^a A_{df}^r}{\sum_n A_{dn}^a + \sum_m A_{dm}^r} \frac{\Gamma_d/2\pi}{(E_e - E_{id})^2 + \Gamma_d^2/4} \\ &\approx \frac{\pi^2 \hbar^3}{m_e E_e} \frac{g_d}{2g_i} \frac{A_{di}^a A_{df}^r}{\sum_n A_{dn}^a + \sum_m A_{dm}^r} \delta(E_e - E_{di}). \end{aligned} \quad (2.77)$$

With this last approximation, the resonant strength can be easily computed, resulting in the relation

$$\begin{aligned} S_{idf}^{DR} &= \int_0^\infty \sigma_{idf}^{DR}(E_e) dE_e \\ &= \frac{\pi^2 \hbar^3}{m_e E_e} \frac{g_d}{2g_i} \frac{A_{di}^a A_{df}^r}{\sum_n A_{dn}^a + \sum_m A_{dm}^r}. \end{aligned} \quad (2.78)$$

This quantity is often used to make comparisons between different atomic theories and experimental result, as also done in this work and described in chapters 4 and 5.

In thermal plasmas, such as those studied in astrophysics and nuclear reactors, the free electron energy follow a Maxwellian distribution characterized by an electron temperature  $T_e$ . The modeling of this kind of plasmas is not related directly to the DR cross section, but by the convolution of the former with a Maxwellian distribution. The integral of this quantity constitutes the DR rate coefficient, and it is used in several plasma modeling codes, such as CLOUDY [81], XSTAR [82] and CHIANTI [83], to simulate charge state dynamics and also determine ion populations in steady-state conditions. The DR rate coefficient becomes

$$\alpha_{if}^{DR} = \frac{m_e}{\sqrt{\pi} \hbar^3} \left( \frac{4E_y}{K_B T_e} \right)^{3/2} a_0^3 \sum_d E_{id} S_{idf}^{DR} \exp\left\{ -\frac{E_{id}}{K_B T_e} \right\}, \quad (2.79)$$

where  $E_y$  is the Rydberg constant,  $K_B$  is the Boltzmann constant and  $a_0$  is the Bohr radius. This equation depends on the resonant strengths of the resonances, while in most references (e.g. [84]) it depends on the cross sections. This allows the possibility of measuring these values experimentally through the integral of the DR peaks of the spectra.

The RE process is calculated in a similar manner. In this case, if the final state has the same number of bound electrons as the initial state, the fluorescence yield is replaced by

$$\omega_{df} = \frac{A_{df}^a}{\sum_n A_{dn}^a + \sum_m A_{dm}^r} \quad (2.80)$$

so the final cross section becomes

$$\sigma_{idf}^{DR}(E_e) = \frac{\pi^2 \hbar^3}{m_e E_e} \frac{g_d}{2g_i} \frac{A_{di}^a A_{df}^a}{\sum_n A_{dn}^a + \sum_m A_{dm}^r} \frac{\Gamma_d/2\pi}{(E_e - E_{id})^2 + \Gamma_d^2/4} \quad (2.81)$$

As is the case for the DR process, the RE is a resonant process. While the DR happens when the electron energy is below the CE threshold, the RE is only possible above this threshold (a practical example of RE will be seen in chapter 5).

## 2.4 Charge exchange

Ion-atom and ion-ion collisions can lead to charge transfer between projectile and target. This is effective with slow atoms or molecules approaching HCl. Therefore, if one goal is to achieve a dominant population of a certain ion species, the chamber of an EBIT must be maintained at an Ultra High Vacuum (UHV), typically around  $10^{-12}$  mBar. At these pressures, the residual gas is mainly hydrogen due to the degassing of the chamber. Therefore, a charge exchange process of interest is



It was theoretically shown that the cross section of this process depends mainly on the atomic number  $Z$  and the collision velocity  $v$  for ions with  $Z \geq 16$  and  $0.04 \leq v \leq 1.8$  (values in  $\times 10^8$  cm/s) [85]. A valid fit from the theoretical results for this cross section (in  $\text{cm}^2$ ) is given by

$$\sigma_{CX} = 2.25 \times 10^{-16} Z \ln\left(\frac{15}{v}\right) \quad (2.83)$$

Since the cross section varies with  $v$  ( $10^8$  cm/s), different pressures yield different cross sections.

## 2.5 Polarization and anisotropy

The electron in an ion occupy atomic orbitals identified by the quantum numbers  $njm_j$ , where  $m_j$  in the magnetic sublevel, with  $m_j = -j, -j+1, -j+2, \dots, j-2, j-1, j$ . When the ions are excited by randomly oriented electrons, the populations of magnetic sublevel

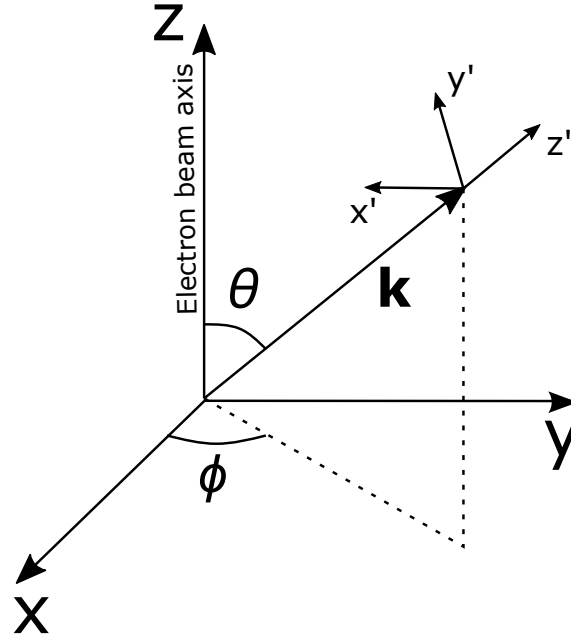


Figure 2.2: Axis of the electron beam and axis of the photon with direction  $\mathbf{k}$ . The direction of the photon is defined by the angles  $\theta$  and  $\phi$  and the radiation polarization is defined in the directions  $x'$  and  $y'$ . The beam direction is align with the  $z$  axis.

follows a statistical distribution that corresponds to the statistical weights  $g(m)$  of the respective levels ( $\sum_m g(m) = 1$ ). The deexcitation of these levels leads to the emission of isotropic and unpolarized radiation.

However, the EBIT has an unidirectional electron beam that interacts with the ion cloud (more details in chapter 3). The electron beam populates magnetic sublevels such that the magnetic dipole between  $-m_j$  and  $m_j$  are align with the beam. For that reason, the distribution of populations no longer follow the regular statistical weights, thus leading to emission of polarized and anisotropic radiation. The measurements at EBITs are generally done with a small solid angle at round  $90^\circ$  with respect to the electron beam, so the intensity distribution  $W(\theta, \phi)$  must be determined to infer the correct flux of the radiation. The representations  $J_i$  and  $J_f$  will be used to identify the total angular momentum of the ion excited by the collision with an electron and the ion after a radiative decay. The degree of polarization varies with the meridional and azimuthal angles  $\theta$  and  $\phi$  of the emitted photon. The polarization axis of the photon will be identified as  $x'$  and  $y'$  and their respective polarization components are the  $W_{x'}$  and  $W_{y'}$ . For the case of an electron beam with cylindrical symmetry, the distribution of the emitted radiation depends only on the  $\theta$  value.

The degree of polarization is defined as [86]

$$P(\theta) = \frac{W_{x'}(\theta) - W_{y'}(\theta)}{W_{x'}(\theta) + W_{y'}(\theta)}. \quad (2.84)$$

The distribution seen by an instrument insensitive to the polarization is given by  $W(\theta) = W_{x'}(\theta) + W_{y'}(\theta)$ .



The electromagnetic interaction operator can be expanded in a set of electromagnetic multipoles. By tracing the initial atomic wavefunction with free electron to the final state with no free electrons, the polarization components for a cylindrical source can be obtained:

$$W_{x'}(\theta) = \frac{W_0}{8\pi} \sum_{\lambda=\text{even}} \left( 1 + B_\lambda(J_i) \left[ A_\lambda(\gamma) P_\lambda(\cos \theta) + A_{\lambda 2}^\perp P_{\lambda 2}(\cos \theta) \right] \right), \quad (2.85)$$

$$W_{y'}(\theta) = \frac{W_0}{8\pi} \sum_{\lambda=\text{even}} \left( 1 + B_\lambda(J_i) \left[ A_\lambda(\gamma) P_\lambda(\cos \theta) - A_{\lambda 2}^\perp P_{\lambda 2}(\cos \theta) \right] \right). \quad (2.86)$$

In these expressions,  $W_0$  is the total probability of photon emission,  $P_\lambda(\cos \theta)$  are the Legendre polynomials and  $P_{\lambda 2}(\cos \theta)$  are the associated Legendre polynomials. The parameters  $B_\lambda$ ,  $A_\lambda$  and  $A_{\lambda 2}^\perp$  are the orientation parameter, angular distribution coefficient and the linear polarization parameter. The values of  $\lambda$  are even to describe linear polarization, while odd numbers are for describing circular polarization. The total angular distribution is given by [87]

$$W(\theta) = \frac{W_0}{4\pi} \sum_{\lambda=\text{even}} [1 + B_\lambda(J_i) A_\lambda(\gamma) P_\lambda(\cos \theta)]. \quad (2.87)$$

The orientation parameter only depends on the initial state, thus being described by the variables  $J_i$ ,  $m_i$  and  $g(m_i)$ . For a cylindrical symmetry, the simplest approximation of the EBIT system at the trap region, this parameter is given by [86]

$$B_\lambda(J_i) = \sum_m (-1)^{J_i+m} [(2\lambda+1)(2J_i+1)]^{1/2} \begin{pmatrix} J_i & J_i & \lambda \\ m & -m & 0 \end{pmatrix} g(m). \quad (2.88)$$

The quantity in big parentheses is the Wigner 3-j symbol. This parameter describes the distribution of the nonstatistical magnetic sublevel population of the intermediate state after a resonant capture.

The parameters  $A_\lambda$  and  $A_{\lambda 2}^\perp$  are related to the radiative decay of the ion, and both depend on the angular momentum of the initial and final state  $J_i$  and  $J_f$ . They also depend on the multipole operator used to describe the transition. The expressions of these parameters can be simplified by neglecting high-order multipoles. Considering only a single multipole transition, there is a dependence on the overlap between the initial and final orientation,

$$F_\lambda(LL'J_fJ_i) = (-1)^{J_f+J_i-1} [(2\lambda+1)(2L+1)(2L'+1)(2J_i+1)]^{1/2} \begin{pmatrix} L & L' & \lambda \\ 1 & -1 & 0 \end{pmatrix} \begin{Bmatrix} L & L' & \lambda \\ J_i & J_i & J_f \end{Bmatrix}. \quad (2.89)$$

The quantity in big brackets is Wigner 6-j symbol, an analogous quantity to the Wigner 3-j symbol but used to do a summation of 3 angular momenta. The values  $L$  and  $L'$  denote the order of the multipole. The parameters then become

$$A_\lambda = F_\lambda(LL'J_fJ_i), \quad (2.90)$$

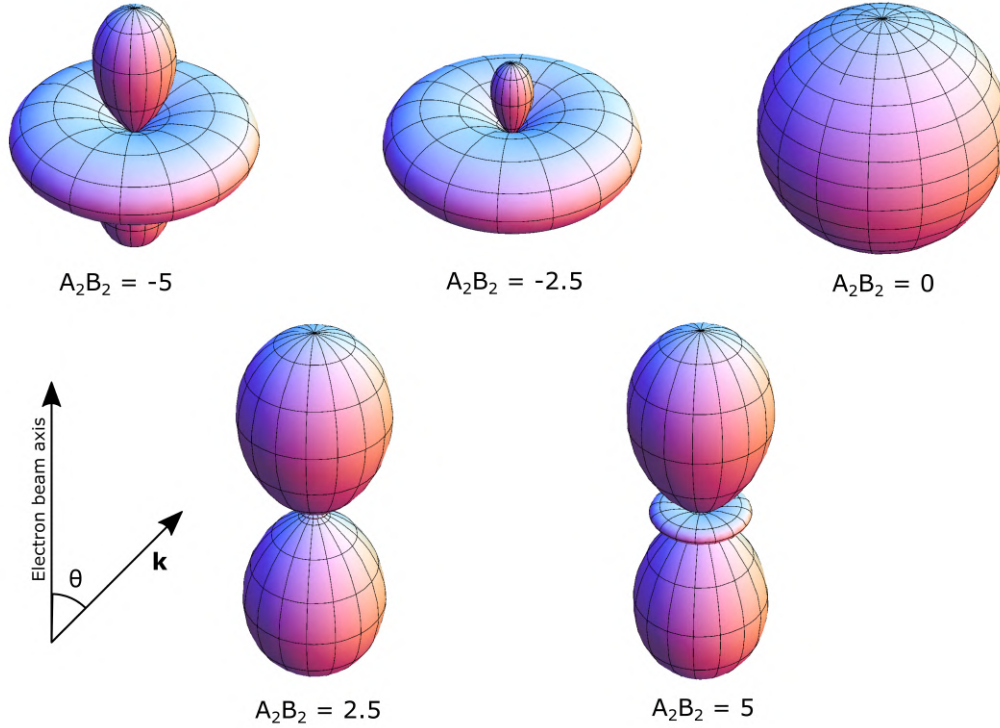


Figure 2.3: Representation of the relative value of  $W(\theta)$  in the electron beam frame of reference for several values of  $A_2B_2$ . All the cases are invariant to  $\phi$ . The vector  $\mathbf{k}$  is the direction of the photon.

$$A_{\lambda 2}^{\perp} = -\Lambda(\kappa)f_{\lambda}(L)A_{\lambda}, \quad (2.91)$$

where  $\Lambda(\kappa)$  is a signal factor, where  $\kappa$  is the type of multipole, i. e.  $\Lambda(E) = 1$  for electric multipoles and  $\Lambda(M) = -1$  for magnetic multipoles. The quantity  $f_{\lambda}(L)$  is defined as

$$f_{\lambda}(L) = -\left[\frac{(\lambda-2)!}{(\lambda+2)!}\right]^{1/2} \frac{\begin{pmatrix} L & L' & \lambda \\ 1 & -1 & 0 \end{pmatrix}}{\begin{pmatrix} L & L' & \lambda \\ 1 & -1 & 0 \end{pmatrix}}. \quad (2.92)$$

With this definitions, the degree of polarization can be rewritten as

$$P(\theta) = \frac{\sum_{\lambda=\text{even}} [B_{\lambda}(J_i)A_{\lambda 2}^{\perp}P_{\lambda 2}(\cos \theta)]}{\sum_{\lambda=\text{even}} [1 + B_{\lambda}(J_i)A_{\lambda}(\gamma)P_{\lambda}(\cos \theta)]}. \quad (2.93)$$

### 2.5.1 E1 and M1 transitions

The most commonly observed radiation in the EBIT is provided by electric dipole (E1) and occasionally by magnetic dipole (M1) transitions. For these transitions,  $A_4$  and higher order parameters vanish, thus there is only a dependence in  $A_2$  and  $B_2$ . The order of the

multipole is  $L = 1$  and  $f_2(L = 1) = -1/2$ . With this values, the polarization components become

$$W_{x'}(\theta) = \frac{W_0}{8\pi} [1 + A_2 B_2 (3 \cos^2 \theta - 2)] \quad (2.94)$$

$$W_{y'}(\theta) = \frac{W_0}{8\pi} [1 + A_2 B_2]. \quad (2.95)$$

Note that the  $y'$  component of the radiation is isotropic, while the  $x'$  component varies with  $\theta$ . As a result, the degree of polarization and total distribution for a E1 transition are given by [88]

$$P^{E1}(\theta) = \frac{-3A_2 B_2 \sin^2 \theta}{2 - A_2 B_2 (1 - 3 \cos^2 \theta)}, \quad (2.96)$$

$$W^{E1}(\theta) \propto 1 + \frac{1}{2} A_2 B_2 (3 \cos^2 \theta - 1). \quad (2.97)$$

The figure 2.3 shows examples of the relative distribution seen by an instrument insensitive to the polarization,  $W(\theta)$ , for various values of  $A_2 B_2$ . The value of  $A_2 B_2$  is specific for each transition.

Using these expressions, and considering that the observation is made at  $90^\circ$ , the degree of polarization and total relative distribution are given by

$$P^{E1}(90^\circ) = \frac{-3A_2 B_2}{2 - A_2 B_2} \quad (2.98)$$

$$W^{E1}(90^\circ) \propto 1 - \frac{1}{2} A_2 B_2. \quad (2.99)$$

By mixing these two equations, the polarization factor correction becomes

$$W^{E1}(90^\circ) \propto \frac{3}{3 - P^{E1}(90^\circ)}. \quad (2.100)$$

For the case of the M1 transitions, only the factor  $\Lambda(\kappa)$ , with  $\Lambda(M) = -1 = -\Lambda(E)$ . Thus, the polarization factor correction becomes

$$W^{M1}(90^\circ) \propto \frac{3}{3 + P^{M1}(90^\circ)}. \quad (2.101)$$

In the DR process, an intermediate state can radiatively decay to several close-lying different final states, all with distinct values of degree of polarization. EBIT measurements are usually done with silicon-based x-ray detectors, which do not have a sufficient resolution to resolve those transitions. To compensate for this effect, the  $A_2$  parameter used in equation (2.93) can be replaced by [88]

$$\overline{A_2} = \frac{\sum_f A_2 A_{df}^r}{\sum_f A_{df}^r}, \quad (2.102)$$

where  $A_{df}^r$  is the radiative transition rate from an intermediate state  $d$  into a final state  $f$ . This new parameter represents the effective anisotropy of the photon emission in the region. Note that for high- $Z$  ions, higher multipoles can contribute to significant deviations from the electric dipole approximation presented for the calculation of the polarization degree and anisotropy of the photon emissions.

## 2.6 Atomic codes

### 2.6.1 Flexible Atomic Code

Several codes were developed over the last decades, but most of the atomic structure calculations necessary to this work were performed using the Flexible Atomic Code (FAC) [67]. This code makes use of the fully relativistic Dirac-Coulomb Hamiltonian and a modified electron-electron central potential to approximate the atomic radial wave functions, and their respective energy is obtained with eigenvalues with the standard Numerov integration method. This code has the advantages of being open source and freely available to use, its relatively high computational efficiency and an optional Python interface facilitates the integration of this code in custom projects such as the present work.

Similarly to multi-configuration methods, the atomic state functions are defined as a mixing of basis of states as described in the equation (2.13). This code solves the Dirac equation for a local central field defined by the sum of the nuclear potential  $V^N(r)$  and the electron-electron interaction  $V^{ee}(r)$ . To make the wavefunctions more accurate, the finite size of the nucleus has to be taken into account. The nuclear potential can be written as [67]

$$V^N(r) = \begin{cases} \frac{Z}{2} \left( \frac{r}{R_N} \right) \left[ 3 - \left( \frac{r}{R_N} \right)^2 \right], & r \leq R_N \\ Z/r, & r > R_N \end{cases}, \quad (2.103)$$

where  $R_N$  is the nuclear radius. In the code, this radius takes the value of  $R_N = 2.2667 \times 10^{-5} A^{1/3}$ . The electron-electron potential is approximated with a central field that depends upon the occupation numbers and respective wavefunctions themselves. As is the case of the previously mentioned self consistent field methods, the potential is obtained iteratively.

Moreover, this framework uses the previous energies and wavefunctions to calculate bound-bound (like collisional excitation and radiative transitions) and bound-free atomic processes (like ionizations and recombinations), both convenient to the modeling of the plasmas. To calculate processes with an interaction between a free electron and an ion, this code uses the Distorted Wave Born approximation. Comparisons between the theoretical values obtained from this code and experimental results show an accuracy of few eV at  $\sim 1240$  eV for the energy levels and 10-20% for transition rates and cross sections [67].

Besides the use of the Configuration Interaction method to calculate the relevant energy states, the same framework was used to increase the precision of the calculations with the Many Body Perturbation Theory method. Results from the FAC calculations, as well as an example of the application of the FAC-MBPT correction, will be presented in chapter 4.

### 2.6.2 Multiconfiguration Dirac-Fock codes

Several codes leveraging the MCDF method to calculate atomic structure have been developed over the years. One of the most relevant is the Multiconfiguration Dirac-Fock and General Matrix Elements (MCDFGME) [89, 90]. As the name suggests, the code utilizes the MCDF method to calculate wavefunctions and their respective energy. In this case, the code uses a self-consistent field approach with the equations described in the subsection 2.1.5, and makes afterwards detailed Quantum Electrodynamics (QED) corrections in a perturbative way. This code was developed by P. Desclaux and P. Indelicato at Université Pierre et Marie Curie (now Sorbonne Université) and is mostly focused on high-accuracy determination of energy levels with QED, hyperfine and nuclear finite size effects. It is written in FORTRAN95. Results for the calculation of the DR-LMM structure of Fe XVII with this code were included in this work.

Another known MCDF code that is widely used is the General-Purpose Relativistic Atomic Structure Program (GRASP) [91]. It was developed by the I. P. Grant group at University of Oxford to make large-scale relativistic CI calculations. As is the case with MCDFGME, high order QED corrections are treated perturbatively. The GRASP2K [92] is an improved version of the initial GRASP92 code, developed by Jönsson et al.. This code was recently updated again by C. Froese Fischer et al., and released in the form of GRASP2018 [93].

Other examples of popular codes used to calculate atomic structure and transition probabilities are the RELAC [94], HULLAC [95] and RMBPT [96]. In contrast with the previous programs, these codes are not available publicly.



## EXPERIMENTAL SETUP

In order to investigate the proprieties of HCI, it is necessary to produce and maintain them long enough to be studied. During the decades of the 1970's and 1980's, experiments with merged beams were limited to the production of ions with charge  $q < 6$  [97], while experiments with tokamaks were only capable of producing highly charged ions with high ion temperature [98]. The radiation emitted from a moving source suffers a shift in frequency according to the Doppler effect, which means that radiation emitted by high temperature ions suffers an energy broadening that is a limiting factor in experiments. At the time, Electron Beam Ion Sources (EBIS) were used to provide ions to accelerators [99]. The concept of this device was adapted to create the Electron Beam Ion Trap (EBIT) [98], a device not only capable of producing ions with any positive charged state but also to trap them in a small ion cloud that can be probed with both photons and electrons. The resulting emitted radiation can also be observed on a side port.

In the present experiments, the FLASH-EBIT was used (at the Max-Planck-Institut für Kernphysik, in Heidelber) to study Fe XVII and Kr XXVIII (both Ne-like) and the PolarX-EBIT (at PETRA III Deutsches Elektronen-Synchrotron) was use to study Fe XVII, as well as the population dynamics. The basic functioning of EBIT systems is described, as well as specific characteristics of the FLASH-EBIT and PolarX-EBIT. The operations schemes of each experiment will also be presented. A small description of the Test Storage Ring will also be presented to give context to the TSR measurements also analysed in this work.

### 3.1 The Electron Beam Ion Trap

The EBIT is a device capable of producing highly charged ion plasmas. Inside it, an almost monoenergetic focused electron beam is used to interact with an injected gas

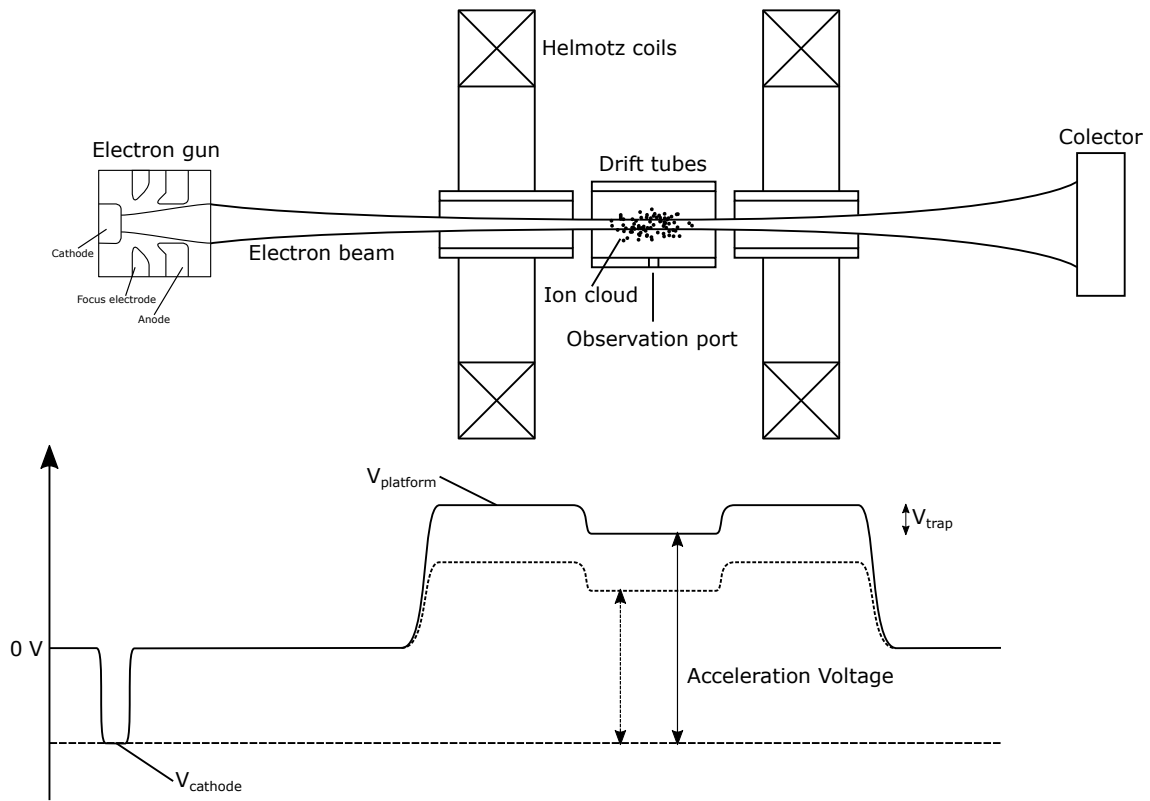


Figure 3.1: General representation of an electron beam ion trap. An electron gun produces an electron beam that is accelerated towards the drift tubes, where it is compressed by the Helmholtz coils and produces an ion cloud. The electron beam is stopped in the collector. The observation port allows the collection of the radiative emissions of the plasma. The electric potential along the system is represented below.

of the element to ionize it. This beam multi-ionizes the atoms with both CI and EA mentioned previously in chapter 2. The focused beam also produces a negative space-charge potential that confines the ions radially. The ions are further electrostatically confined along the beam axis with a set of drift tubes that can be adjusted according to the experiment needs. The electron beam can also be used to probe the system by doing energy scans periodically with any duty cycle. Different schemes of energy duty cycles were used to obtain the results of these work.

The electron beam is produced with an Pierce-type electron gun. This gun is usually shielded from the magnetic field of the trap by a Bucking coil to provide the electrons in a field free environment.

The ionization rate is proportional to the current density. To maximize this value, the electron beam is compressed in the central region of the drift tubes by a strong magnetic field generated either superconductive Helmholtz coils or arrangements of permanent magnets. Although the superconducting coils offer stronger magnetic fields, the permanent magnets may be sufficient for certain applications, while also being cheaper and easier to operate. These strong magnetic fields are enough to operate with electron beams with typical currents in the order of tens of  $mA$  with a beam diameter in the order of tens



of  $\mu\text{m}$ .

### 3.1.1 Electron beam dynamics

The electron beam is an essential part of the EBIT system. It is responsible for producing and trapping the ions and can be using to probe them in various schemes. The most important characteristics for the experiments are the electric current, electron kinetic energy and radial distribution. These proprieties are important to evaluate the interaction between the beam and the ion cloud. The electron gun is composed of a cathode, that emits electrons via termionic emission when an high voltage is applied, electrodes to focus the beam and an anode to further accelerate the electron beam. The current of the beam can be estimated by

$$I_e = p V_{\text{cathode}}^{3/2}, \quad (3.1)$$

where  $p$  is the perveance, a value that characteristic to each electron gun. The voltage of the cathode  $V_{\text{cathode}}^{3/2}$  can be adjusted.

To make a realistic evaluation of the radius of the electron beam, the non-laminar flow of the electrons and the finite temperature of the cathode have to be taken into account. In the theory by Herrmann [100], for an electron beam passing through a uniform magnetic field  $B$ , the beam has a Gaussian profile in the radial plane. Here, 80 % of the electrons are confined in a radius given by [101]

$$r_H = r_B \sqrt{\frac{1}{2} + \frac{1}{2} \sqrt{1 + 4 \left( \frac{8m_e K_B T_c r_c^2}{e^2 B^2 r_B^4} + \frac{B_c^2 r_c^4}{B^2 r_B^4} \right)}}. \quad (3.2)$$

where  $T_c$ ,  $B_c$  and  $r_c$  are the electron temperature and magnetic field at the cathode and the cathode radius. This radius is smaller for lower values of  $B_c$ . This is usually achieved by adjusting a bucking coil in the electron gun, compensating the magnetic field of the trap. This equation corrects the radius  $r_B$  obtained from the simplistic, where is assumed laminar flow, no electron temperature and a zero magnetic field at the cathode:

$$r_B [\mu\text{m}] = \frac{150}{B[\text{T}]} \sqrt{\frac{I_e[\text{A}]}{E_e[\text{keV}]}}. \quad (3.3)$$

The radius is important o evaluate the current density  $j_e = I_e/(\pi r_H^2)$ , the value that is desirable to maximise to improve the ionization rate. The EBIT systems usually operate with an electron beam radius around 35  $\mu\text{m}$ .

The interaction between the electron beam and the ions only occurs in the region were the electron beam and the ion cloud overlap. Since the ion cloud mean radius is bigger than the beam radius, the effective electron density is smaller than the current density with the previous radius. Figure 3.2 shows an artistic 3D representation of the overlap volume, while the figure 3.3 represents a simulation of an ion trajectory in an EBIT, which corresponds to elliptical orbits. Studies have been done in the past to measure

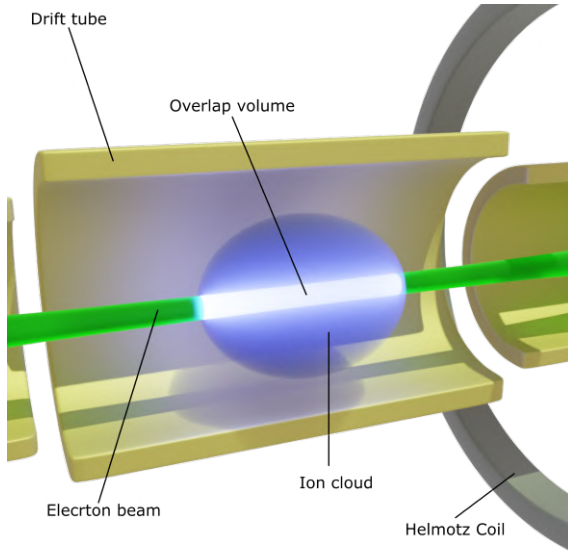


Figure 3.2: 3D artistic representation of the ion cloud expanding beyond the electron beam. The bright white glow in the center represents the overlap between the ion cloud and the electron beam.

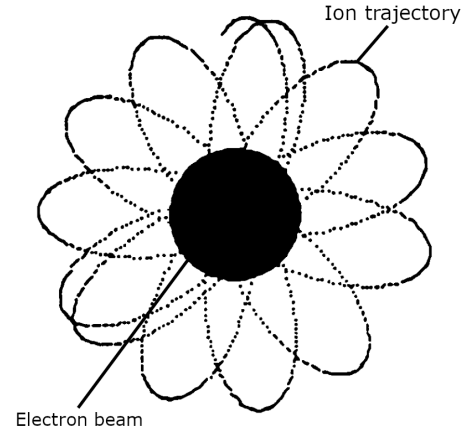


Figure 3.3: Cross sectional view along the electron beam axis of a simulation of the trajectory of an ion influenced by the electron beam in the EBIT environment. Figure adapted from [22].

experimentally the overlap factor by measuring UV forbidden and allowed transitions. In the current work, the effective electron density was evaluated by adjusting this value as a free input parameter in simulations. This value was also estimated by fitting the spectral time evolution of the data obtained in the polarX-EBIT. The details about the EBIT energy schemes will be described in the next sections.

The electrons leave the cathode with a finite thermal energy transverse to the electron beam direction. Therefore, the interaction of the electron beam with magnetic field results in a gyromagnetic motion and a helical motion along the magnetic lines. The energy of the perpendicular motion can have systematic effects [41, 88]. These effects were not accounted in the current work.

The energy of the electron beam is defined by

$$E_e \approx |V_{\text{cathode}}| + |V_{\text{platform}}| + |V_{\text{trap}}| - |V_{\text{space}}|. \quad (3.4)$$

In this context,  $V_{\text{cathode}}$  is the bias voltage given to the cathode,  $V_{\text{trap}}$  is the voltage given to the central drift tube,  $V_{\text{platform}}$  is the additional bias given to the other tubes and the space charge is the potential generated by the electrons of the beam and trapped ions. The space charge potential counteracts the external positive potentials and the acceleration of the beam, trapping the ions radially. This potential varies through the radius of the beam. For a beam with a radius of 35  $\mu\text{m}$ , the variation of the potential across the beam is between 20 V and 50 V.

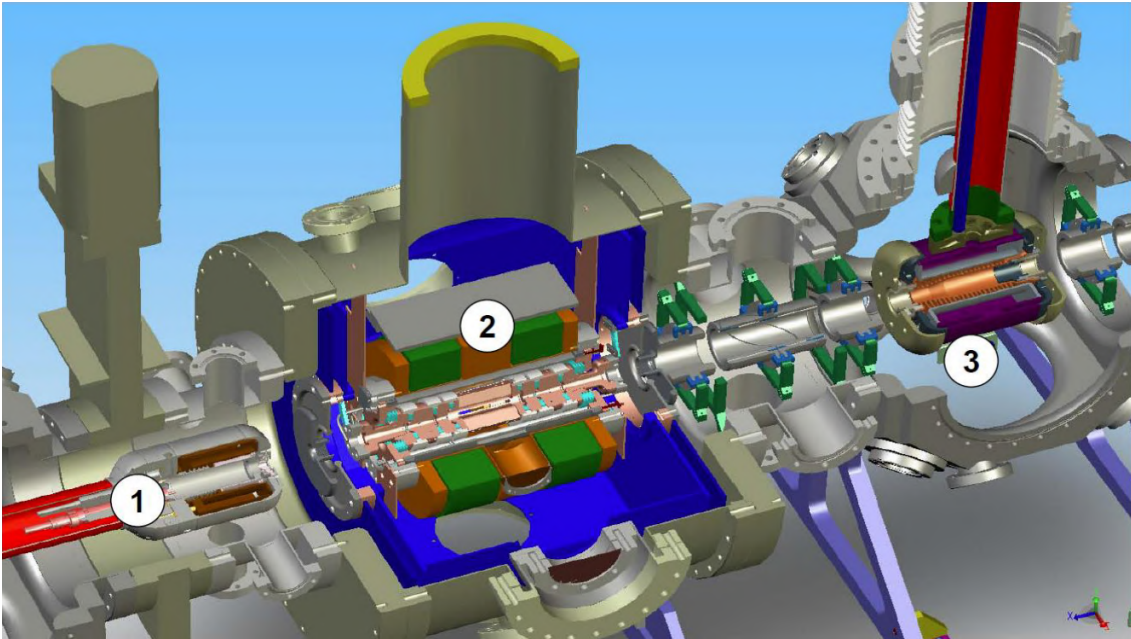


Figure 3.4: Cross-sectional view from the FLASH-EBIT. The numbers in the figure indicate: (1) the electron gun, (2) the ion trap surrounded by the drift tubes and de Helmholtz coils, (3) the electron beam collector. Figure adapted from [88].

## 3.2 FLASH-EBIT

### 3.2.1 Specifications

Most of the experimental data analysed in this work was obtained in the FLASH-EBIT (mechanical representation in figure 3.4) at the Max-Planck-Institut für Kernphysik, in Heidelberg [102]. This device is design for interactions of external high-brightness x-ray sources with HCI. Although it has a length of approximately 3 m and weights roughly 1 Ton, it is still movable and was already used in several x-ray source facilities, like synchrotrons and free electron lasers. Figure 3.4 illustrates the configuration of the device, basically composed of an electron gun, a set of drift tubes, superconducting magnetic coils and an electron collector. The electron gun is capable of producing an electron beam with several hundreds of  $mA$  that is further compressed to a diameter below  $50 \mu m$  at the trap region by a 6 T magnetic flux density. In order to avoid charge exchange of the ions with hydrogen atoms during operation, the trap is kept in ultra high-vacuum, with a pressure of around  $10^{-11}$  mbar.

The electron gun is represented in the Figure 3.5 (a). The cathode is made of a tungsten filament coated with Barium Oxide. The low work function of the surface matrix  $\Phi_{W,BaO} = 2$  eV leads to a low operating temperature, between 1300 and 1500 K, which increases the lifetime of the cathode. The cathode is encapsulated in the focus electrode, that helps extract the electrons from the cathode. Adjusting the potential of this electrode also allows to control the electron beam current. The anode provides the extraction filed.

The electron beam energy is roughly defined by the potential difference between the cathode and the drift tube assembly. All this setup is surrounded by the trimming coil and bucking coil. Adjusting the current of these coils allow to compensate the magnetic field generated superconducting magnets at the electron gun region. Having a low magnetic field on the cathode is important to reduce the beam diameter at the trap region.

The collector is represented in the figure 3.5 (b). After the electron beam has passed through the trap, it goes into the collector. The collector has a magnetic coil that decreases the residual magnetic field generated by the superconduction magnets. As the magnetic field decreases, the beam radius increases and the electrons repel each other, being deposited in the collector walls. The extraction electrode has a high voltage compared to the electron gun cathode, ensuring that most electrons cannot pass the collector. The excess energy deposited in the walls is carried way by a water cooling system. Ions that enter the collector can sputter the inner face of the electrodes and eject secondary electrons. The suppressor electrode prevents them from escaping back to the trap. Furthermore, this electrode can also be used to separate incoming ions from the trap from the electrons, giving the EBIT the ability to extract the produced ions for experiments that are made externally.

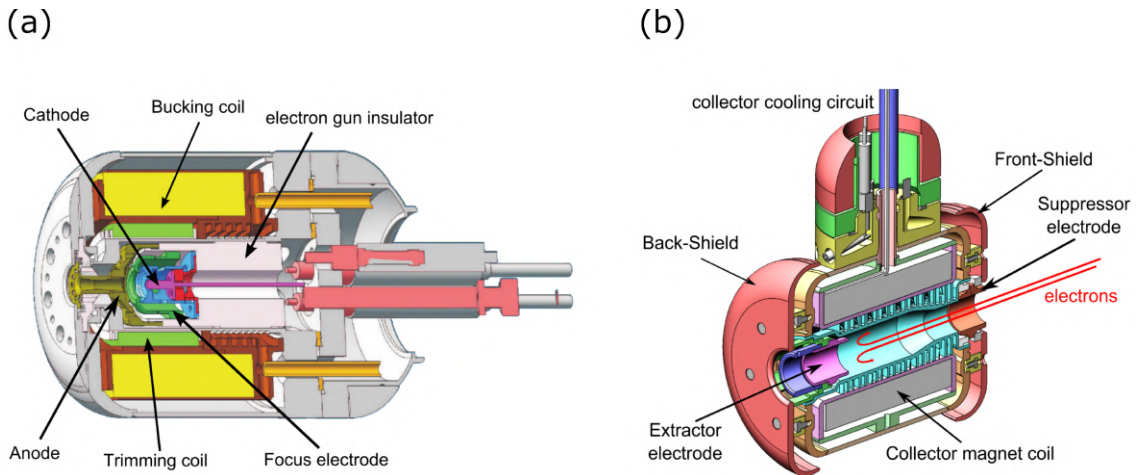


Figure 3.5: Cross-sectional view of the electron gun (a) and collector (b) of the FLASH-EBIT. Figure adapted from [88].

### 3.2.2 Fe XVII measurement

This EBIT was used to produce and study an high purity plasma of Fe XVII. A beam of iron pentacarbonyl was used to introduce the iron in the trap. In order to make measurements in a high-purity Fe XVII plasma, the electron beam energy scan was comprised of a 0.5 s breeding time (an periode of constant electron beam energy to produce the Fe XVII plasma) at 1.15 keV and 40 ms linear down-scan from 1.1 to 0.5 keV and a time symmetric linear up-scan relative to the down-scan (represented i figure 3.6). As the Fe XVII ionization threshold is about 1.26 keV, a high population of this ion is expected

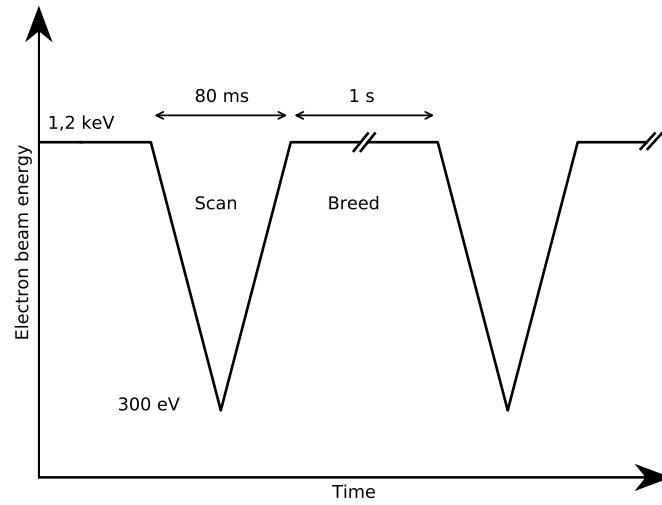


Figure 3.6: Energy scheme of the electron beam used in the FLASH-EBIT measurements. It is composed of a 1 s breeding period of 1.2 keV followed by a 40 ms long linear sweep to 300 eV and another 40 ms linear sweep back to 1.2 keV. This scheme was repeated in loop, with typical measurements of several hours.

to be produced during the breeding time. The energy scans are performed repeatedly during a small fraction of time to ensure a low depletion of the population of interest during the recombination processes present at this period, the latter being compensated afterwards during the next breeding time. The electron current  $I_e$  was measured at high energies to be around 20 mA during the experiment. This current was adjusted according to  $n_e \propto I_e/\sqrt{E}$  to keep the electronic density  $n_e$  constant, where  $E$  is the electron beam energy. The x-ray emission were measured with a Silicon Drift Detector (SDD), position at  $90^\circ$  in respect to the electron beam axis. The photon energy-resolution of the SDD was around 120 eV at 6 keV and the electron beam has an energy spread of around 5 eV at 800 eV. The down-scan and up-scan were recorded as separate data. This gives the possibility to analyse the potential differences between the spectra in these two stages. If there is a population depletion due to the DR process during the downwards scan, i.e. DR recombination of Ne-like into Na-like ions, it is expected that the upwards scan present a spectrum that indicates an higher presence of lines of Fe Na-like ions. A comparison between these two spectra is presented in the next chapter.

A very similar scheme was used to record the Kr XXVII spectra. In this case, the breeding energy was around 2500 eV (the ionization threshold of this ion is around 2929 eV). The scan was made between 2500 eV and 40 eV.

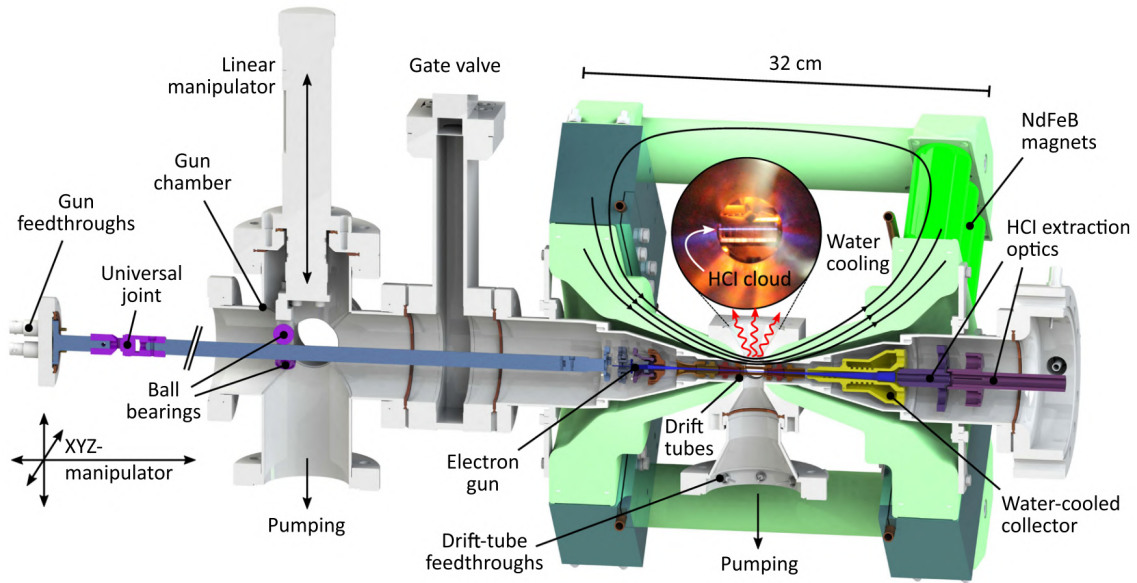


Figure 3.7: Cross-sectional view from the Heidelberg compact EBIT design. Apart from the gas chamber design, the NdFeB magnet assembly is visible with superimposed magnetic lines. The electron gun and the collector are visible right besides the left and right of the central trap, where radiation emission is indicated with curly arrows. Figure adapted from [103].

### 3.3 PolarX-EBIT

#### 3.3.1 Specifications

Additional data of Fe XVII, recorded at the PolarX-EBIT, was also analysed in this work. The PolarX-EBIT is one of several systems built at the Max-Planck-Institut für Kernphysik in Heidelberg with the Heidelberg Compact EBIT (HC-EBIT) design [103]. This design allows the construction of portable EBITs with a compact footprint that operate at room-temperature without superconducting magnets. Figure 3.7 shows a representation of the HC-EBIT design. Similarly to the FLASH-EBIT design, it has an electron gun, a drift tube assembly and an electron collector. Instead of a pair of superconducting Helmholtz coils, this design utilizes  $8 \times 3 \times 3$  arrays of NdFeB permanent magnets (magnetic flux diagram in the figure) that achieve a magnetic density flux of 0.86 T at the center of the trap.

The electron gun of the PolarX is represented in the figure 3.8 (a). In contrast with the original, the PolarX-EBIT features an off-axis electron gun. This configuration has the advantage of giving an unobstructed path to photon beams that maximizes the overlap volume between the beam and the ion cloud. This, in conjunction with the compact profile, makes this device ideal to take to high intensity x-ray source facilities, like synchrotrons and free electron lasers. In case of previous measurements in FLASH-EBIT, the photon beam is slightly misaligned with the electron beam in order to not hit the cathode, but still having overlap at the trap. Like the FLASH-EBIT, the cathode is made of tungsten impregnated with barium. The rear anode defines the extraction potential

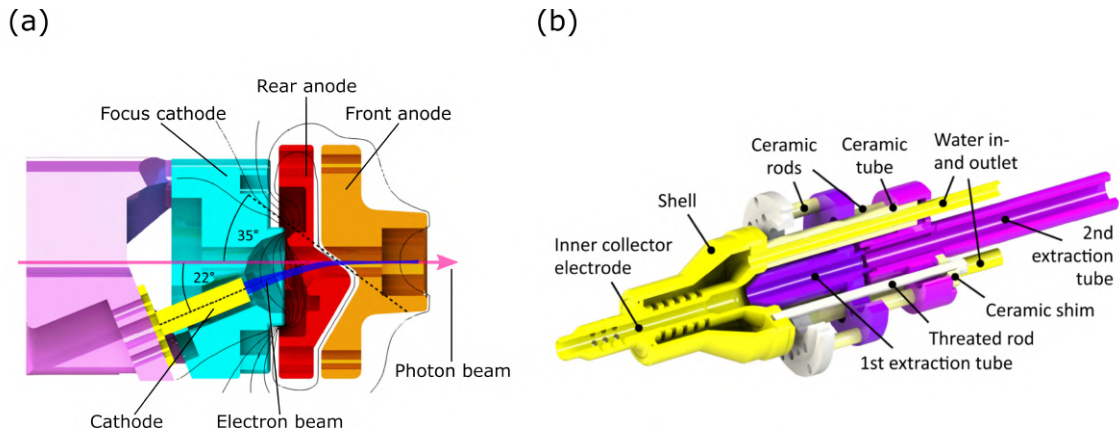


Figure 3.8: Cross-sectional view of the electron gun (a) and collector (b) of the PolarX-EBIT. The off-axis cathode allows the positioning of photon beams in the same axis as the electron beam. Figure adapted from [103]

and the front anode steers the electron beam to the central trap. The focus cathodes are used to compensate the electron motion due to the residual magnetic field. These two cathodes are split in two halves to adjust the compensating potential. These electrons are also used to regulate the electron emission current.

The collector is represented in the figure 3.8 (b). The magnetic field diminishes inside the collector, so the radius of the beam increases and the electrons are collected in the walls. The extraction tubes are used to prevent the passage of electrons and extract positive ions. The collector is connected to an ampere-meter to evaluate the electron beam transmission, which is around 99 %. This measurement is used during the adjustment of the voltages of the drift tube assembly to evaluate the quality of the beam and detect possible undesired current losses. The heat from the collected electrons is once again extracted with a water cooling system.

### 3.3.2 Fe XVII measurement

The Fe XVII photon emission was also studied in this EBIT system. The operation of the Electron beam energy scheme is fundamentally different from the case of the FLASH-EBIT. A slow triangle signal (40 min period) with an energy between 300 eV and 500 eV, that was used for the probing of the ion cloud, was superimposed with a fast square wave (4 s period with a 50 % duty cycle) with energies of 1.5 keV and 0.3 keV (represented in figure 3.9). This was accomplished with a fast behlke switch<sup>1</sup> between a power supply with constant voltage for the breeding energy and a slow scanning power supply for the probing energy. Effectively, the net result is an approximate square wave, where the low energy varies slowly. With this configuration, not only the photon emission for each electron energy is registered, but also the evolution of this emission for a specific electron energy in a time axis. With this scheme, there is the possibility to obtain the

<sup>1</sup><http://www.behlke.com/>

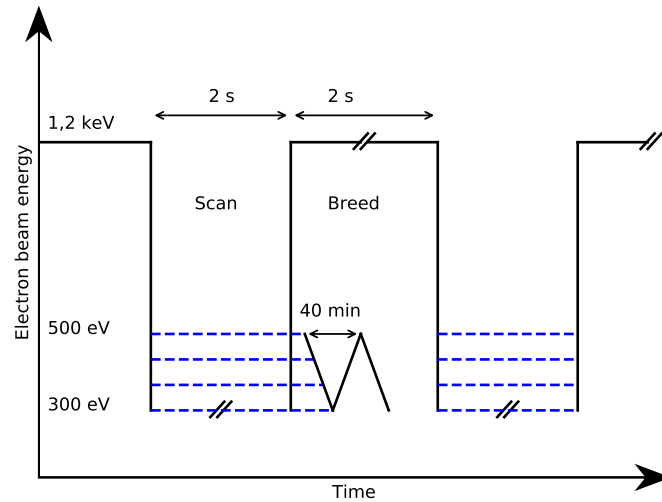


Figure 3.9: Energy scheme of the electron beam used in the PolarX-EBIT measurements. It is composed of a 2 s breeding period of 1.2 keV followed by a 2 s period of constant low energy (probing period). The low energy varied between 500 eV and 300 eV with a slow triangular function with a period of 40 min. The blue dashed line represents the low energy moving with time. This scheme was repeated in loop for a very long time.

time evolution of the spectrum thus observing the DR-LMM process of the Fe XVII and the subsequent decay of this population for the Na-like, Mg-like and Al-like ions. The x-ray photons were measured with a SDD similar to the one used in the FLASH-EBIT. Furthermore, PolarX-EBIT measurements were made with a lower electron current of around 2 mA, resulting in an energy spread of around 3.5 eV at 400 eV.

### 3.4 Test Storage Ring

The Test Storage Ring (TSR) is an heavy ion storage ring constructed at the Max-Planck-Institut für Kernphysik, in Heidelberg. The ring was designed for investigations in atomic and molecular physics by holding a beam of cold ions and molecules for large intervals of time. A scheme of the device is represented in Figure 3.10. It stores the beam by redirecting and refocusing it in a series of dipole and quadrupole magnets. This device can store ions in periods up to hours. This is an important feature, as it guarantees that most of the ions analysed in the experiments are in the ground state, as opposed to possible metastable states that can have an unwanted presence in another experimental setups. High purity of a given charge state is also always present.

After injecting the highly charged ions for storage, the ion beam is cooled by electron cooling to reduce transversal and longitudinal temperatures that thus reducing Doppler broadening in spectroscopy observations. In this process, the beam is merged with a cold dense electron beam. The ion beam energy spread is dissipated by the coulomb interactions with the electron beam. A second merged electron beam, placed in another location of the TSR, is used as an electron target. By tuning the energy of the ion beam



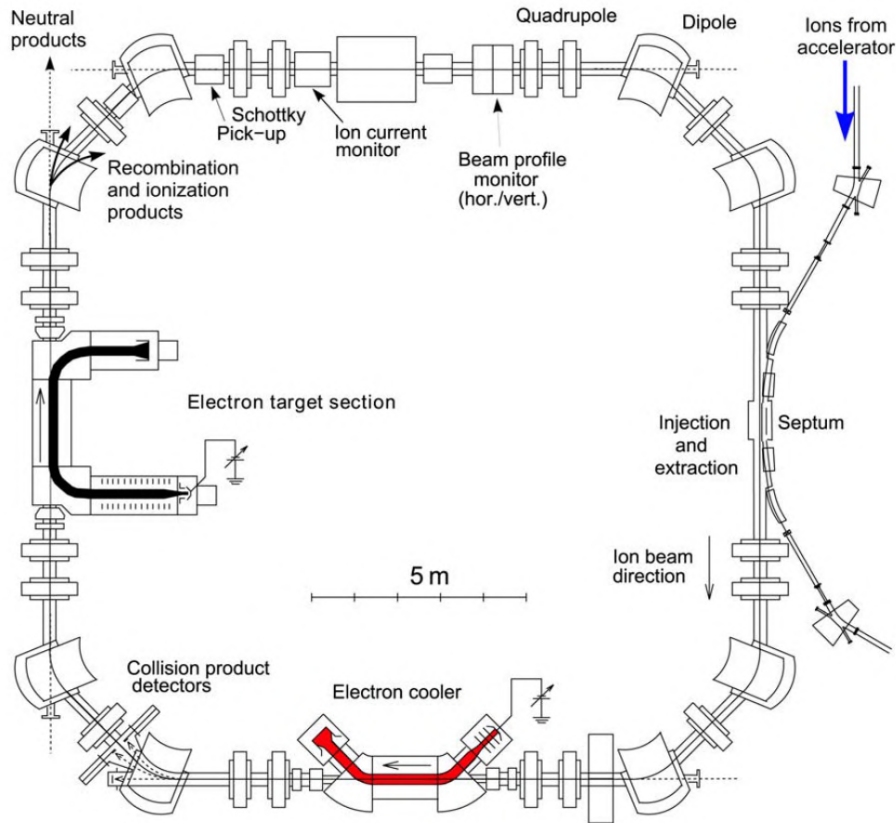


Figure 3.10: Scheme of the Heidelberg heavy ion Test Storage Ring. The ion beam is injected at the top left corner (blue arrow) and travels clockwise in the ring. On the bottom linear section, there is the electron cooler that attenuates the energy spread of the ion beam. On the left linear section, there is an electron beam that interacts directly with the ion beam as a collision target. Products of the collision with a different charge state are collected at the end of the same linear section, separated by a dipole magnet. Figure adapted from [27].

and this second electron beam, ionization and recombination processes can be induced with electron-ion collisions. Ions with different charge states can then be selected with a magnetic dipole into a charge-plate detector. By measuring the rate of ionization/recombination and the ion beam current simultaneously, the absolute values of the ionization or recombination rates can be obtained. This technique has been used extensively to measure several the cross sections of recombination and ionization of various highly charged ions [27].

In order to improve the reliability of the plasma simulations developed in this work, the ionization cross sections for the Na-like, Mg-like and Al-like ions were compared with previous TSR measurements [47, 78, 104]. In contrast to the recombination processes, the ionization processes were not fully calculated theoretically due to their complexity in the energy region due to EA ionization. In the next chapter, we provide calculations of these processes obtained with FAC.

Measurements of the DR structure of Ne-like iron have been done in the past in

the TSR [105]. The experiment has an high ion-electron collision energy resolution, with an energy spread below 0.63 eV. The measured recombination rate coefficient had an uncertainty of around 20%, higher than usual due to the use of a continuous ion injection scheme, that led to an higher uncertainty in the current measurement. In the more typical setups, the ions are accumulated and cooled in the storage ring before the recombination starts. Furthermore, the presented DR cross sections were also subjected to a background removal that also increased the said uncertainty. The background was composed mostly of RR and charge exchange with residual gas. This data was broadened to the experimental energy resolution of the EBIT experiments and was used in this work to make comparisons with theory and between experimental setups.

## COMPUTATIONAL CALCULATIONS AND SIMULATIONS

In this chapter, the atomic data calculations performed during this work are presented. The Flexible Atomic Code calculations are detailed and the methods used for the relevant calculations are specified. The method for simulating the charge state dynamics of an EBIT plasma, with atomic processes calculations mentioned in chapter 2, is presented, as well as specific results regarding the simulation of the experimental conditions. As the charge state dynamics of the plasma was directly recorded at the PolarX-EBIT, the time dynamic spectrum is compared to a simulated one. Further studies of preliminary results for Kr measurements are also overviewed.

### 4.1 Cross section calculations

In order to aid the identification of all the structures present in the experimental spectra, the most of the relevant experimental features were simulated. To simulate an experimental spectrum, one of the most important steps is to determine the population of each charge state. To this end, all the important cross sections of dielectronic and radiative recombination, collisional ionization and charge exchange were calculated. For this work, all of these cross-sections were performed using the FAC and FAC-MBPT. All the physical theory involved in these atomic processes was already discussed in chapter 2.

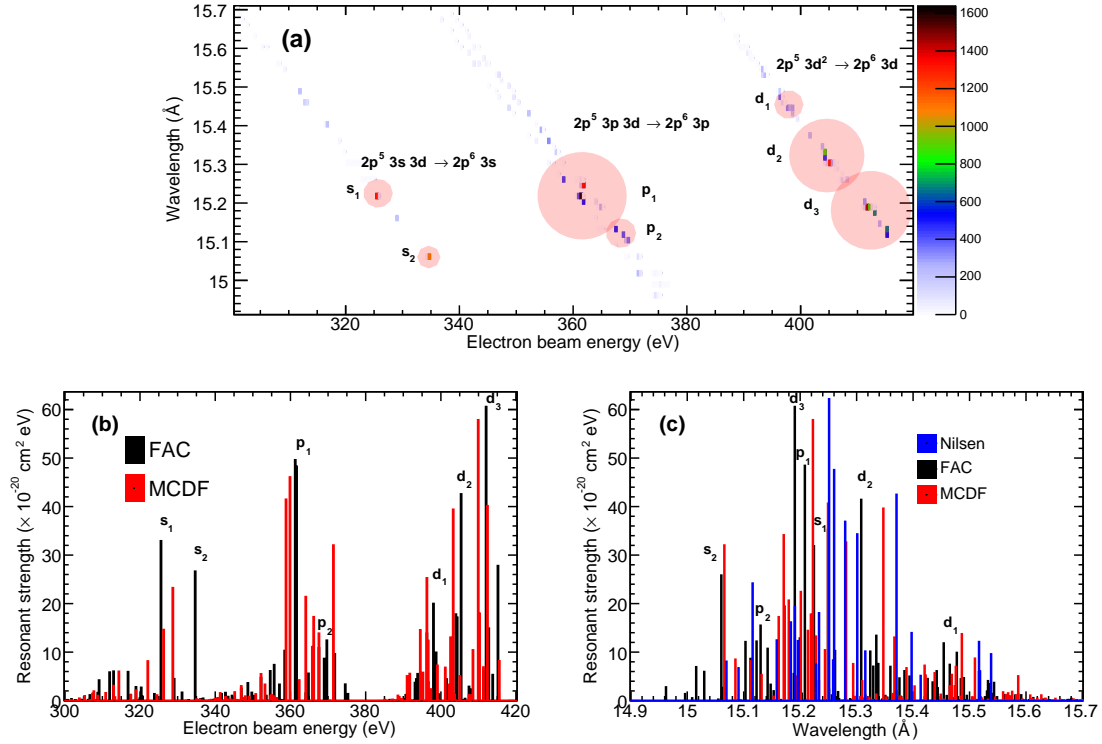


Figure 4.1: Top plot: theoretical resonant strengths obtained from FAC. Abscissa: electron beam energy; ordinate: emitted wavelength. Experimentally resolved spectral lines are labelled as  $s_1$ ,  $s_2$ ,  $p_1$ ,  $p_2$ ,  $d_1$ ,  $d_2$ ,  $d_3$  and  $d_4$ , where the first letter is the  $l$  of the spectator electron in the  $2p^5 3l 3d \rightarrow 2p^6 3l$  transition. The circle diameter shows the relative resonance strength of the channels contributing to these spectral lines. Projection onto both axes are displayed in bottom left (b) and right (c) plots, respectively, and compared with our (MCDF) and Nilsen’s calculations [106].

#### 4.1.1 LMM DR calculations

In the context of this work, the DR LMM structure of Fe XVII had to be calculated to compare to the experimental results, since this process was the focus of the experimental analysis. FAC was used to calculate the atomic structure of the ion, the respective radiative transition rates and auger rates. For this case, taking as atomic number  $Z = 26$ , structure calculations were performed for the configurations  $1s^2 2s^2 2p^6$  (initial states),  $1s^2 2s 2p^6 3l 3l'$  and  $1s^2 2s^2 2p^5 3l 3l'$  (intermediate states) and  $1s^2 2s^2 2p^6 3l$  (final states), where  $l$  and  $l'$  can be any valid orbital quantum number. 236 individual intermediate atomic states were calculated. The possible DR channels are given by the combinations of autoionizing transitions from the initial to intermediate states (around 236 individual resonances, most with multiple radiative decay channels). The radiative transition rates from the intermediate to the final states were calculated and used, combined with the auger rates, to calculate the resonant strength of each DR resonance. The same results were used to calculate the resonance width and an histogram was filled with the resonances in a Lorentzian shape, where the electron beam energy position is

given by the energy difference of the respective initial and intermediate states and the photon energy is given by the energy difference between the respective intermediate and final state. The widths of the resonances are usually very small. When these values were smaller than the bin width of the histogram, the respective bin was filled with the value of the resonant strength divided by the bin width. The results of these calculations are highlighted in the figure 4.1. In the subfigure (a), 3 diagonal lines are distinguishable in the histogram. These lines correspond to the five possible final states  $(1s^2 2s^2 2p^6 3s)_{J=1/2}$ ,  $(1s^2 2s^2 2p^6 3p)_{J=1/2,3/2}$  and  $(1s^2 2s^2 2p^6 3d)_{J=3/2,5/2}$  (each of the two latter lines are actually two lines very close to each other, corresponding to the several  $J$  values). Within those lines, resonances with a radiative transition of an electron from a  $3d$  orbital into a  $2l$  orbital were found to be dominant. Seven clearly distinguishable structures were identified and, from now on, will be referred to by their spectator electron orbital and order of appearance in the electron beam energy axis ( $s_1, s_2, p_1, p_2, d_1, d_2, d_3$ ). Each structure is observed as only one peak at the experimental spectra due to the electron beam energy spread being much larger than the DR resonant width. Subfigure (b) shows a projection on the electron beam axis. Atomic structure, auger rates and radiative transition rates calculated with MCDF were provided to compare with FAC and the experimental results. A similar procedure to the FAC calculations was applied to obtain the MCDF DR resonant strengths. The results are also present in this subfigure. Subfigure (c) is a projection of (a) in the photon wavelength axis. Here, a comparison is made between FAC, MCDF and values from Nilsen [106]. The latter are relatively old tabulated results of DR calculations for Ne-like ions that are still used in some databases.

The FAC also includes methods to refine atomic structure calculations with Many Body Perturbation Theory. As seen in chapter 2, the wavefunction corrections depend upon all the other possible unperturbed wavefunctions of the system. Due to the time consumption of this method, it was only applied to calculate the DR LMM structure of Fe XVII. For the final calculation virtual states with principal quantum number until  $n = 32$  were included. As an example of this application, the figure 4.2 (left) shows the energy of the first excited state of Fe XVII in relation to the energy of the respective ground state, as a function of the maximum principal quantum number of the virtual state. Figure 4.2 (right) shows, for the same set of calculations, the difference between the energy with a maximum principal quantum number of  $n$  and  $n - 1$ . For  $n = 32$ , the energy change is less than 0.001 eV, a value well under the experimental uncertainty.

The most important results of the DR-LMM calculations are represented throughout the tables 4.1 to 4.4. To make the results more readable, only the resonances with a resonant strength (given by FAC) above 10% of the value of the most intense resonance were tabulated. Note that in the simulations and experimental analysis, all the resonances were considered. They are organized by the resonant energy given by the FAC and linked to the resolved spectral lines mentioned early. All the resonances came from an initial state  $(1s^2 2s^2 2p^6)_{J=0}$ . The intermediate and final states, given in  $jj$  notation, derives from the FAC-MBPT calculation, with the corresponding LSJ term coming from the MCDF.

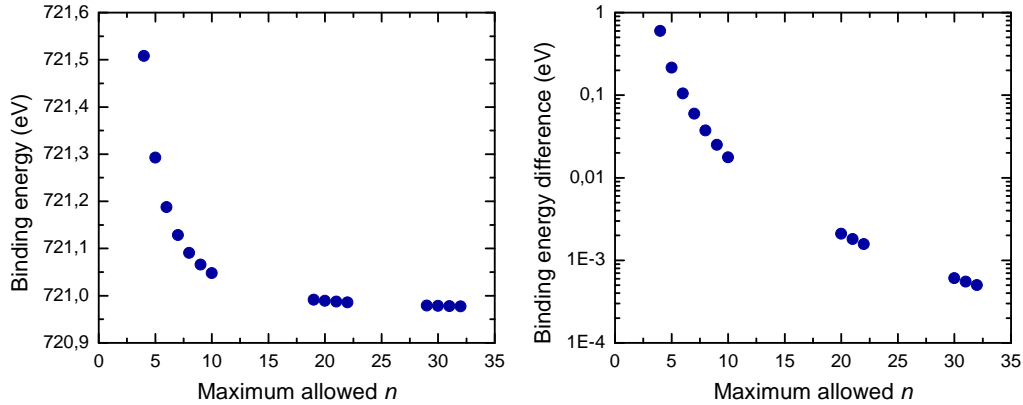


Figure 4.2: Energy of the first excited state of Fe XVII calculated with FAC-MBPT. The several results are represented as a function of the maximum allowed principal quantum number  $n$  in the virtual states. Left figure represents the value of the energy in relation to the ground state, while the right figure represents the relative difference between consecutive calculations in a logarithmic scale.

The tables 4.1 and 4.2 show the resonant free electron energy of each resonance, as well as the respective resonant strength. A general shift in energy is present when going from FAC to FAC-MBPT. Apart from that, there is a good agreement between all the calculations within mostly less than 5 eV. Although without an expected big resonant strength, the resonance with intermediate state  $[(2s_{1/2}2p_{1/2}^22p_{3/2}^4)_{1/2}3s_{1/2}^2]_{1/2}$  was not found in the MCDF calculations. The resonances that mostly contributed to the resolved peaks have as intermediate state:

- $[(2p_{1/2}2p_{3/2}^4)_{1/2}3s_{1/2}]_1 3d_{5/2}]_{3/2}$  for the  $s_1$  structure;
- $[(2p_{1/2}2p_{3/2}^4)_{1/2}3s_{1/2}]_1 3d_{3/2}]_{3/2}$  for the  $s_2$  structure;
- $[(2p_{1/2}2p_{3/2}^4)_{1/2}3p_{1/2}]_1 3d_{3/2}]_{3/2}$  and  $[(2p_{1/2}^22p_{3/2}^3)_{3/2}3p_{3/2}]_2 3d_{5/2}]_{5/2}$  for the  $p_1$  structure;
- $[(2p_{1/2}2p_{3/2}^4)_{1/2}3d_{3/2}^2]_{5/2}$  for the  $d_2$  structure
- $[(2p_{1/2}2p_{3/2}^4)_{1/2}3d_{3/2}]_1 3d_{5/2}]_{7/2}$  for the  $d_3$  structure.

The peaks  $p_2$  and  $d_1$  do not have a dominant resonance, and are instead formed by a mixture of resonances with relatively low intensity. All the mentioned resonances complete the DR process with an electric dipole transition ( $\Delta J = \pm 1$ ). This translates into high fluorescence yields, as the radiative rate becomes much higher than the auger rate, therefore resulting in high resonant strengths relative to the remaining resonances. The MCDF calculation reveals an unexpectedly low resonant strength for the  $s_1$  resonance in comparison with other theories, while the opposite situation is apparent for the resonances forming the  $p_2$  structure. On the other hand, FAC and MCDF suggests that the  $d_2$  structure is dominated mainly by a single resonance, while the FAC-MBPT calculations

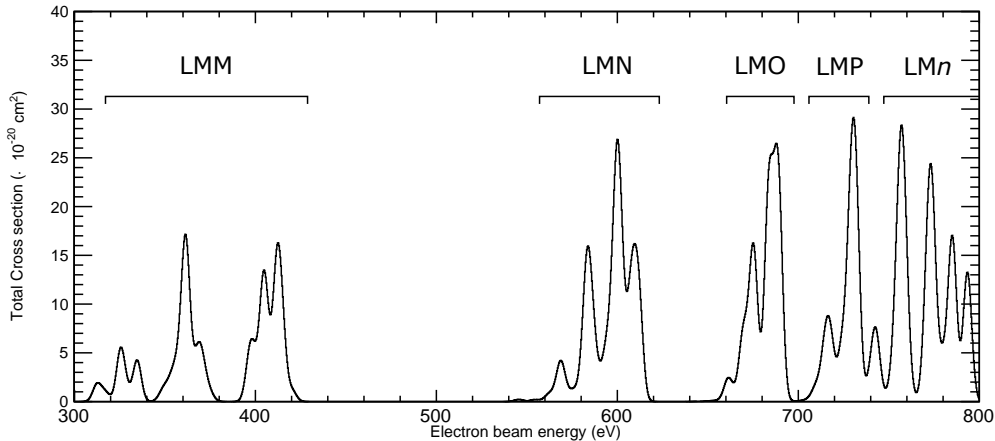


Figure 4.3: Projection of the DR  $LMn$  structure for Ne-like Fe calculated with FAC.

have this structure being composed by several resonances with resonant strengths more evenly distributed. Another noteworthy feature is that all the dominant resonances have an intermediate state with at least one electron in the  $3d$  orbital, being this the one who always decays radiatively while the second excited one is always a spectator.

The tables 4.3 and 4.4 list the wavelength of the radiative transitions of the resonances presented in the previous tables. Besides the FAC, FAC-MBPT and MCDF, results from Nilsen [106] and Beiersdorfer [58] are also presented. Beiersdorfer's paper provided a limited number of resonances, so the respective column lacks values for some transitions. There is a good agreement between theories regarding the wavelengths all across the board.

#### 4.1.2 Collisional cross-section calculations

To make a reliable simulation of the EBIT plasma, which is one of the goals of this work, all the recombination and ionization processes of the important ionic species need to be calculated. A similar process to the DR described above was used to calculate the DR  $LMn$  sequence, with  $n = M, N, O, \dots, T$ , for the Ne-like and Na-like ions. The figure 4.3 shows a projection in the electron beam energy axis of the DR  $LMn$  structure for Ne-like Fe. The results in this figure have been broadened to facilitate the comparison with the experimental results. For the Mg-like and Al-like ions, only the LMM, LMN and LMO structures were calculated, since it is expected residual population of these charge states. Furthermore, as the number of electrons increases, the number of possible resonances and time of computation also increases significantly, making impractical large scale calculations beyond the ones mentioned.

The FAC includes packages to calculate the cross sections of RR and CI. RR cross sections for Ne-like, Na-like, Mg-like and Al-like ions were calculated, with the recombining ion resting on all possible shells, from  $n = 3$  to  $n = 15$ . The figure 4.5 shows the FAC

Table 4.1: Theoretical values of the peak resonant energies  $E$  (eV) and strengths  $S$  ( $10^{-20}$  cm<sup>2</sup>eV) obtained in this work with FAC, FAC-MBPT and MCDP. The resonant and final states are given in  $jj$  and LSJ notations.

Label	Intermediate state	Final state	$E_{\text{FAC}}$	$E_{\text{MBPT}}$	$E_{\text{MCDP}}$	$S_{\text{FAC}}$	$S_{\text{MBPT}}$	$S_{\text{MCDP}}$
$s_1$	$[(2p_{1/2}^2 2p_{3/2}^3)_{3/2} 3s_{1/2}]_2 3d_{5/2} [1]_{1/2}$	$^4D_{1/2}$	313.06	310.23	313.08	6.04	6.42	2.74
	$[(2p_{1/2} 2p_{3/2}^4)_{1/2} 3s_{1/2}]_1 3d_{5/2} [3]_{3/2}$	$^2D_{3/2}$	325.70	322.21	321.98	31.91	29.54	7.34
$s_2$	$[(2p_{1/2} 2p_{3/2}^4)_{1/2} 3s_{1/2}]_1 3d_{3/2} [3]_{3/2}$	$^2P_{3/2}$	334.62	330.72	328.60	25.89	23.22	20.61
	$[(2p_{1/2}^2 2p_{3/2}^3)_{3/2} 3p_{1/2}]_2 3d_{5/2} [3]_{3/2}$	$^4P_{3/2}$	341.50	338.94	339.95	1.04	1.11	0.24
$p_1$ <sup>a</sup>	$[(2p_{1/2}^2 2p_{3/2}^3)_{3/2} 3p_{3/2}]_0 3d_{5/2} [5]_{5/2}$	$^2D_{5/2}$	354.47	351.41	352.30	6.16	7.99	4.59
	$[(2p_{1/2} 2p_{3/2}^4)_{1/2} 3p_{1/2}]_1 3d_{5/2} [5]_{5/2}$	$^4F_{5/2}$	355.8	353.04	354.05	5.14	4.95	0.04
$p_2$	$[(2p_{1/2} 2p_{3/2}^4)_{1/2} 3p_{1/2}]_1 3d_{3/2} [2]_{3/2}$	$^4F_{3/2}$	353.65	355.05	352.28	1.06	9.70	0.16
	$[(2p_{1/2} 2p_{3/2}^4)_{1/2} 3p_{1/2}]_1 3d_{3/2} [3]_{3/2}$	$^4F_{3/2}$	353.65	355.05	352.28	0.008	0.22	0.32
$p_1$	$[(2p_{1/2} 2p_{3/2}^4)_{1/2} 3p_{3/2}]_2 3d_{5/2} [5]_{5/2}$	$^2D_{5/2}$	358.36	355.09	356.22	0.03	0.61	0.48
	$[(2p_{1/2} 2p_{3/2}^4)_{1/2} 3p_{1/2}]_1 3d_{3/2} [3]_{3/2}$	$^2D_{3/2}$	361.25	357.38	358.83	48.50	47.02	38.59
$p_1$	$[(2p_{1/2}^2 2p_{3/2}^3)_{3/2} 3p_{3/2}]_2 3d_{5/2} [5]_{5/2}$	$^2D_{5/2}$	361.67	358.04	359.77	35.26	34.74	30.35
	$[(2p_{1/2} 2p_{3/2}^4)_{1/2} 3p_{1/2}]_1 3d_{3/2} [2]_{3/2}$	$^2S_{1/2}$	361.71	358.42	367.70	12.90	12.36	12.68
$p_2$	$[(2s_{1/2} 2p_{1/2}^2 2p_{3/2}^4)_{1/2} 3s_{1/2}^2]_{1/2}$	$^3P_{3/2} \ ^2P_{3/2}$	364.85	361.80		5.56	4.45	
	$[(2p_{1/2} 2p_{3/2}^4)_{1/2} 3p_{3/2}]_2 3d_{3/2} [1]_{1/2}$	$^2P_{1/2}$	367.42	363.36	364.06	10.77	11.87	19.61
$p_1$	$[(2p_{1/2} 2p_{3/2}^4)_{1/2} 3p_{3/2}]_1 3d_{3/2} [2]_{5/2}$	$^2D_{5/2}$	368.99	364.74	371.33	8.69	4.43	29.69
	$[(2p_{1/2} 2p_{3/2}^4)_{1/2} 3p_{3/2}]_1 3d_{5/2} [3]_{3/2}$	$^2D_{3/2}$	369.50	365.35	366.12	12.17	11.39	16.64

<sup>a</sup>Peak used for energy calibration



Table 4.2: Continuation of table 4.1.

Label	Intermediate state	Final state	E <sub>FAC</sub>	E <sub>MBPT</sub>	E <sub>MCDF</sub>	S <sub>FAC</sub>	S <sub>MBPT</sub>	S <sub>MCDF</sub>
d <sub>1</sub>	$[(2p_{1/2}^2 2p_{3/2}^3)_{3/2} 3d_{3/2} 2)_{2} 3d_{5/2}]_{5/2}$	$^4G_{5/2}$	396.39	393.3	396.73	9.42	11.46	11.37
	$[(2p_{1/2}^2 2p_{3/2}^3)_{3/2} 3d_{5/2}^2]_{7/2}$	$^4D_{7/2}$	397.93	394.65	396.22	11.89	13.96	12.55
d <sub>2</sub>	$[(2p_{1/2} 2p_{3/2}^4)_{1/2} 3d_{5/2}^2]_{7/2}$	$^2G_{7/2}$	404.14	400.95	402.46	13.45	12.08	11.92
	$[(2p_{1/2} 2p_{3/2}^4)_{1/2} 3d_{3/2} 2)_{2} 3d_{5/2}]_{5/2}$	$^2F_{5/2}$	404.45	401.05	402.21	10.19	24.19	1.33
	$[(2p_{1/2} 2p_{3/2}^4)_{1/2} 3d_{3/2} 2)_{2} 3d_{5/2}]_{5/2}$	$^2F_{5/2}$	404.45	401.05	402.21	7.00	6.27	1.78
d <sub>3</sub> <sup>a</sup>	$[(2p_{1/2} 2p_{3/2}^4)_{1/2} 3d_{3/2}^2]_{5/2}$	$^2F_{5/2}$	405.22	401.98	403.14	41.48	23.62	35.91
	$[(2p_{1/2} 2p_{3/2}^4)_{1/2} 3d_{5/2}^2]_{1/2}$	$^2P_{1/2}$	411.16	407.57	408.61	6.25	7.53	9.59
	$[(2p_{1/2} 2p_{3/2}^4)_{1/2} 3d_{3/2} 1)_{3} 3d_{5/2}]_{7/2}$	$^2F_{7/2}$	411.90	407.96	410.07	60.63	58.13	52.73
	$[(2p_{1/2} 2p_{3/2}^4)_{1/2} 3d_{3/2} 1)_{3} 3d_{5/2}]_{5/2}$	$^2D_{5/2}$	412.85	408.75	410.29	14.74	13.79	16.84
	$[(2p_{1/2} 2p_{3/2}^4)_{1/2} 3d_{3/2} 1)_{3} 3d_{5/2}]_{3/2}$	$^2P_{3/2}$	415.20	411.12	412.39	12.26	12.66	17.84
	$[(2p_{1/2} 2p_{3/2}^4)_{1/2} 3d_{3/2} 1)_{3} 3d_{5/2}]_{3/2}$	$^2P_{3/2}$	415.20	411.12	412.39	15.55	16.92	18.24
	$[(2p_{1/2} 2p_{3/2}^4)_{1/2} 3d_{3/2}^2]_{1/2}$	$^2P_{1/2}$	420.27	416.73	415.67	6.01	5.39	7.49

<sup>a</sup>Peak used for energy calibration

Table 4.3: Theoretical values of emitted wavelengths ( $\text{\AA}$ ) obtained in this work with FAC, FAC-MBPT, and MCDP. The resonant and final states are given in  $j-j$  and LSJ notations. Respective data provided by Nilsen [106] and Beiersdorfer et al [58] are also listed for comparison.

Label	Intermediate state	Final state	$W_{\text{FAC}}$	$W_{\text{FAC-MBPT}}$	$W_{\text{MCDP}}$	Ref. [106]	Ref. [58]
$s_1$	$[[[(2p_{1/2}^2 2p_{3/2}^3)_{3/2} 3s_{1/2})_2 3d_{5/2}]_{1/2}]_{1/2}$	$^4D_{1/2}$	15.47	15.52	15.46	15.52	15.49
	$[[[(2p_{1/2} 2p_{3/2}^4)_{1/2} 3s_{1/2})_1 3d_{5/2}]_{3/2}]_{3/2}$	$^2D_{3/2}$	15.23	15.29	15.29	15.28	15.27
$s_2$	$[[[(2p_{1/2} 2p_{3/2}^4)_{1/2} 3s_{1/2})_1 3d_{3/2}]_{3/2}]_{3/2}$	$^2P_{3/2}$	15.06	15.13	15.17	15.12	15.11
	$[[[(2p_{1/2}^2 2p_{3/2}^3)_{3/2} 3p_{1/2})_2 3d_{5/2}]_{3/2}]_{3/2}$	$^4P_{3/2}$	15.59	15.63	15.61	15.58	
$p_1$ <sup>a</sup>	$[[[(2p_{1/2}^2 2p_{3/2}^3)_{3/2} 3p_{3/2})_0 3d_{5/2}]_{5/2}]_{5/2}$	$^2D_{5/2}$	15.38	15.44	15.42	15.63	
	$[[[(2p_{1/2} 2p_{3/2}^4)_{1/2} 3p_{1/2})_1 3d_{5/2}]_{5/2}]_{5/2}$	$^4F_{5/2}$	15.36	15.41	15.39	15.41	15.41
$p_1$ <sup>a</sup>	$[[[(2p_{1/2} 2p_{3/2}^4)_{1/2} 3p_{1/2})_1 3d_{3/2}]_{3/2}]_{3/2}$	$^4F_{3/2}$	15.35	15.32	15.37	15.40	15.30
	$[[[(2p_{1/2} 2p_{3/2}^4)_{1/2} 3p_{1/2})_1 3d_{3/2}]_{3/2}]_{3/2}$	$^4F_{3/2}$	15.40	15.38	15.42	15.45	
$p_2$	$[[[(2p_{1/2} 2p_{3/2}^4)_{1/2} 3p_{3/2})_2 3d_{5/2}]_{5/2}]_{5/2}$	$^2D_{5/2}$	15.26	15.37	15.35	15.37	
	$[[[(2p_{1/2} 2p_{3/2}^4)_{1/2} 3p_{1/2})_1 3d_{3/2}]_{3/2}]_{3/2}$	$^2D_{3/2}$	15.21	15.27	15.25	15.26	15.26
$p_2$	$[[[(2p_{1/2}^2 2p_{3/2}^3)_{3/2} 3p_{3/2})_2 3d_{5/2}]_{5/2}]_{5/2}$	$^2D_{5/2}$	15.25	15.31	15.28	15.55	15.29
	$[[[(2p_{1/2} 2p_{3/2}^4)_{1/2} 3p_{1/2})_1 3d_{3/2}]_{3/2}]_{3/2}$	$^2S_{1/2}$	15.20	15.26	15.08	15.25	15.07
$p_2$	$[[[2s_{1/2} 2p_{1/2}^2 2p_{3/2}^4)_{1/2} 3s_{1/2}^2]_{1/2}]_{1/2}$	$3p_{3/2}^2 P_{3/2}$	15.19	15.24		15.23	15.24
	$[[[(2p_{1/2} 2p_{3/2}^4)_{1/2} 3p_{3/2})_2 3d_{3/2}]_{1/2}]_{1/2}$	$^2P_{1/2}$	15.14	15.21	15.20	15.19	15.19
$p_2$	$[[[(2p_{1/2} 2p_{3/2}^4)_{1/2} 3p_{3/2})_1 3d_{3/2}]_{5/2}]_{5/2}$	$^2D_{5/2}$	15.11	15.18	15.07	15.17	
	$[[[(2p_{1/2} 2p_{3/2}^4)_{1/2} 3p_{3/2})_1 3d_{5/2}]_{3/2}]_{3/2}$	$^2D_{3/2}$	15.10	15.17	15.16	15.20	15.16

<sup>a</sup>Peak used for energy calibration

Table 4.4: Continuation of table 4.3.

Label	Intermediate state	Final state	$W_{\text{FAC}}$	$W_{\text{FAC-MBPT}}$	$W_{\text{MCDF}}$	Ref. [106]	Ref. [58]
$d_1$	$[(2p_{1/2}^2 2p_{3/2}^3)_{3/2} 3d_{3/2}^2 3d_{5/2}]_{5/2}$	${}^4G_{5/2}$	15.48	15.53	15.47	15.54	15.50
	$[(2p_{1/2}^2 2p_{3/2}^3)_{3/2} 3d_{5/2}^2]_{7/2}$	${}^4D_{7/2}$	15.45	15.51	15.49	15.52	15.49
$d_2$	$[(2p_{1/2} 2p_{3/2}^4)_{1/2} 3d_{5/2}^2]_{7/2}$	${}^2G_{7/2}$	15.34	15.39	15.37	15.40	15.37
	$[(2p_{1/2} 2p_{3/2}^4)_{1/2} 3d_{3/2}^2 3d_{5/2}]_{5/2}$	${}^2F_{5/2}$	15.32	15.38	15.36	15.38	15.38
	$[(2p_{1/2} 2p_{3/2}^4)_{1/2} 3d_{3/2}^2 3d_{5/2}]_{5/2}$	${}^2F_{5/2}$	15.33	15.39	15.37	15.39	15.39
	$[(2p_{1/2} 2p_{3/2}^4)_{1/2} 3d_{3/2}^2]_{5/2}$	${}^2F_{5/2}$	15.31	15.36	15.35	15.37	15.35
$d_3^1$	$[(2p_{1/2} 2p_{3/2}^4)_{1/2} 3d_{5/2}^2]_{1/2}$	${}^2P_{1/2}$	15.20	15.26	15.24	15.26	15.24
	$[(2p_{1/2} 2p_{3/2}^4)_{1/2} 3d_{3/2}^2 3d_{5/2}]_{7/2}$	${}^2F_{7/2}$	15.19	15.26	15.22	15.25	15.23
	$[(2p_{1/2} 2p_{3/2}^4)_{1/2} 3d_{3/2}^2 3d_{5/2}]_{5/2}$	${}^2D_{5/2}$	15.17	15.24	15.22	15.23	15.22
	$[(2p_{1/2} 2p_{3/2}^4)_{1/2} 3d_{3/2}^2 3d_{5/2}]_{3/2}$	${}^2P_{3/2}$	15.12	15.19	15.17	15.35	15.18
$d_3^2$	$[(2p_{1/2} 2p_{3/2}^4)_{1/2} 3d_{3/2}^2 3d_{5/2}]_{3/2}$	${}^2P_{3/2}$	15.13	15.20	15.18	15.36	15.18
	$[(2p_{1/2} 2p_{3/2}^4)_{1/2} 3d_{3/2}^2]_{1/2}$	${}^2P_{1/2}$	15.03	15.09	15.11	15.09	15.08

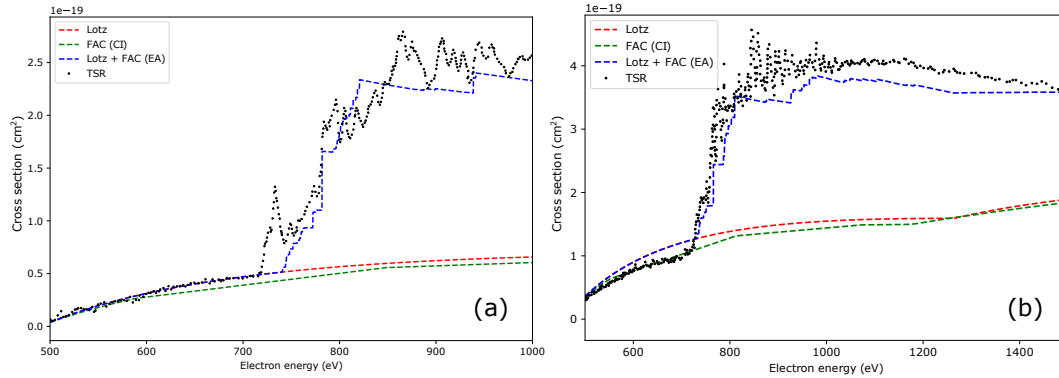


Figure 4.4: Cross section of electron impact ionization for: (a) Na-like iron, (b) Mg-like iron. The dashed red line represents the result given by the Lotz formula, dashed green is the FAC collisional ionization calculation, dashed blue is the Lotz result with the addition of the excitation and autoionization process calculated with FAC and the black dotted line is a TSR measurement [47, 104].

calculation of the RR cross section for Fe Ne-like. The CI for this four ion species were calculated with the standard FAC procedure. However, the EA process plays a prominent roll on the ionization, specially on the breeding energy chosen in the experimental setup. The EA cross section was calculated based on the collisional excitation cross section and the autoionization channels from the intermediate states, as in equation 2.67. Results comparable to experimental cross sections from TSR measurements [47, 78, 104] were obtained (figure 4.4). Nevertheless, the resonant excitation with double autoionization (REDA) process was not taken into account and final results still have room for improvement. This last process is characterized by dielectronic capture followed by an ejection of two electrons. This process is resonant and is responsible for the peaks visible in the TSR measurements after the excitation threshold. The overestimation in the case of the Na-like ion may also be attributed to possible decay paths that were not taken into account. Since this was not the main scope on this work, the experimental data from the TSR measurements was used directly in the plasma simulations as ionization cross sections. The rest of the ion species do not play an important role in the plasma dynamics, so their respective cross sections of ionization and recombination were calculated with the semi-empirical formulas presented in chapter 2.

## 4.2 Charge state dynamics simulations

The acquired spectra in an EBIT depends on the different populations of ionic species present in the plasma. Although the conditions of the plasma environment are stationary during the breeding stage, there is a big variation in the electron beam energy during the probing stage, possibly resulting in a non negligible variation of populations. This

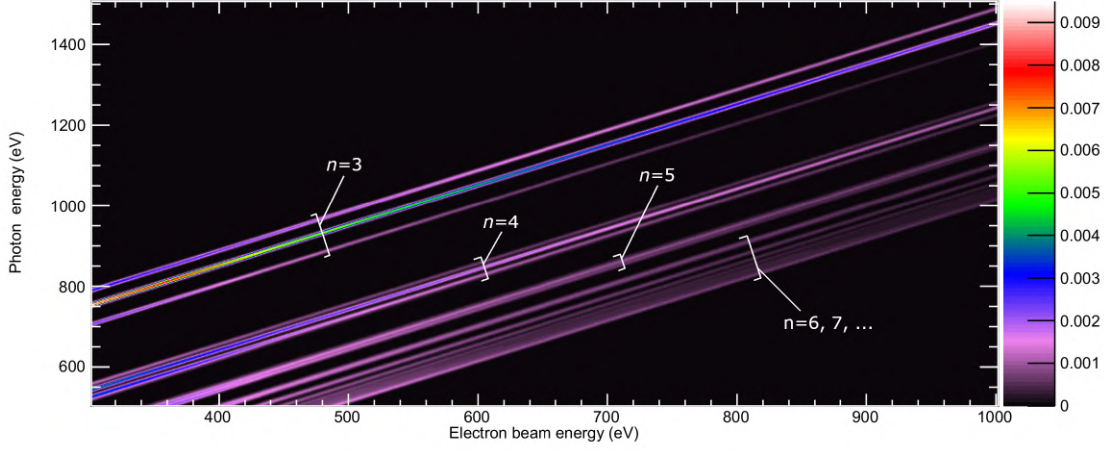


Figure 4.5: FAC cross section of radiative recombination as a function of electron beam energy and photon energy for Fe Ne-like. The calculation included the recombination of an electron in all the available shells, from  $n = 3$  to  $n = 15$ . The cross sections have been broadened for viewing purposes.

variation results in spectra where each charge state population may have a different contribution throughout the all the electron energy range, therefore distorting the structures that are object of study. To account for these systematics, the plasmas from all the experiments present in this work were modeled computationally.

The populations of the different charge states in a plasma have a certain distribution that varies through time as a function of all atomic processes of ion rate formation and destruction, as described in chapter 2. These rates depend on the cross-sections, current density, initial population distribution and temperature of the free electrons. As such, the dynamics of this system in an EBIT, where an incident almost monoenergetic electron beam interacts with an ionized gas of elements with atomic number  $Z$ , can be modeled with  $Z$  coupled differential equations given by

$$\begin{aligned} \frac{dN_q}{dt} = \frac{J_e}{e} \left[ N_{q-1} (\sigma_{q-1}^{CI} + \sigma_{q-1}^{EA}) + N_{q+1} (\sigma_{q+1}^{RR} + \sigma_{q+1}^{DR}) - N_q (\sigma_q^{CI} + \sigma_q^{EA}) - N_q (\sigma_q^{RR} + \sigma_q^{DR}) \right] \\ - N_0 N_q \sigma_q^{CX} \bar{v}_q + N_0 N_{q+1} \sigma_{q+1}^{CX} \bar{v}_{q+1}, \end{aligned} \quad (4.1)$$

where  $N_q$  is the population of ions with charge  $q$ ,  $J_e$  is the electric current density and  $e$  is the elementary electric charge. The variables  $\sigma_q^{XX}$  denote the cross section associated to a atomic process  $XX$  and a charge state  $q$ . As the values of the cross sections depend on the energy of the incident electron (see figures 4.1 and 4.4), their values are dependent on the energy of the electron beam that can be set to be dynamic, i.e. it may have different values over time. Therefore, the integration over time is solved numerically. During this work, all the dynamical calculations were performed with a *Python* code which loads pre-calculated theoretical atomic data of the relevant cross sections and solves the  $Z$  equations iteratively with the Runge-Kutta of 4<sup>th</sup> order method.

Firstly, the code loads the the appropriate CI, EA, DR and RR cross section files previously calculated corresponding to the main ionic species present during the probing stage. To take into account the rest of the possible ions in the initial stage of the simulation, their corresponding ionization and recombination cross sections are calculated on the fly with well known semi-empirical formulas mentioned in chapter 2. These cross section values are then converted into rate values in units of  $s^{-1}$  by the relation

$$R = \frac{J_e}{e} \sigma, \quad (4.2)$$

where  $\sigma$  and  $R$  are a given cross section value and the corresponding rate value. DR lines have a very thin profile and experimentally are usually broadened by the energy width of the quasi monoenergetic electron beam of the EBIT. Therefore, the DR cross sections are convoluted with a Gaussian function (the usual profile of the energy of an electron beam) to better approximate the experimental results. As previously mentioned, the Runge Kutta method is used to solve the Z coupled equations numerically. The 4<sup>th</sup> order of this method is described as follows: for a given differential equation of the form

$$\frac{dy}{dx} = f(x, y) \quad , \quad y(0) = y_0, \quad (4.3)$$

each iteration of an  $x$ , separated by a step  $h$ , can be approximated by

$$y_{i+1} = y_i + \frac{1}{6} (k_1 + 2k_2 + 2k_3 + k_4) h, \quad (4.4)$$

where

$$\begin{aligned} k_1 &= f(x_i, y_i), \\ k_2 &= f\left(x_i + \frac{1}{2}h, y_i + \frac{1}{2}hk_1\right), \\ k_3 &= f\left(x_i + \frac{1}{2}h, y_i + \frac{1}{2}hk_2\right), \\ k_4 &= f(x_i + h, y_i + hk_3). \end{aligned} \quad (4.5)$$

This general procedure is adapted to calculate the variation of the population of each ion according to equation (4.1), value which is calculated every time step. Since this simulation can be performed across several different orders of magnitude of time, the time step of the simulation is dynamic. It starts as a very small value. Each iteration, the sum of the population variations is checked against a certain threshold. If the variation is sufficiently small, the time step is increased by a user definable percentage, allowing the simulation to carry on faster during the time intervals where the population derivatives are negligible.

As an example for this type of simulations, figure 4.7 shows the simulation of an Fe plasma in an EBIT system for several electric current and pressure conditions. It is important to note that the ionization energy threshold of the ground state of an ion increases as the number of electrons of a specific element decreases. This is partially due

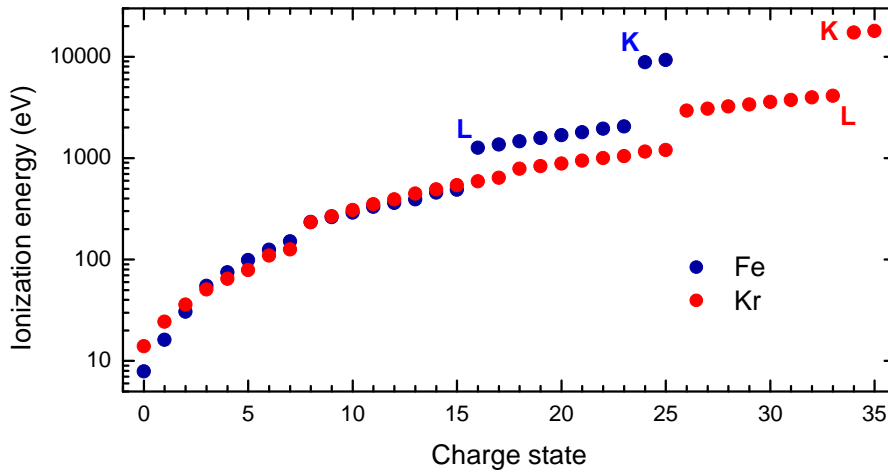


Figure 4.6: Ionization energy threshold for every positive Fe (blue) and Kr (red) ion in the ground state. The values were retrieved from the NIST ionization database [107].

to the fact that the higher the number of electrons for the same nucleus, the greater is the screening potential that the most outer electron feels. Figure 4.6 represents the ionization energy threshold for the Fe and Kr electrons, according to the NIST database [107]. Apart from the increasing energy of the ionization thresholds with charge state, the energy jumps are due to close-shell configurations. These gaps are more apparent between the 15+ and 16+, and 23+ and 24+ charge states for the Fe case. The same gaps are present in the Kr case for the charge states that correspond to the same number of electrons as the charge states mentioned for iron. The first energy gap is related to Fe XVII (16+) where both the K and L shells are fully closed, while the second gap refers to the case of Fe XXV (24+), where only the K shell is fully closed. The ionization energies of Fe XVI and Fe XVII are around 489 eV and 1263 eV. In the simulations of figure 4.7, the electron beam energy is set to either 1150 eV or 490 eV. These simulations show the dependence of the population purity on the electron beam energy and pressure values. The objective is to maximize the Fe XVII population. In every case, the simulation started with only neutral Fe ions. Each simulation represents the population fraction of charge state at a given time. By setting a constant electron energy beam between the ionization energies of the Na-like and Ne-like ions, each charge state population raises and falls through time, each being converted to the next charge state until an equilibrium is reached. The Ne-like ions cannot be ionized, thereby a high level of purity of this species is found in the ion cloud when the equilibrium is reached.

As seen in the figure 4.7, when the pressure is low enough and the electron beam energy is just below the Fe XVII threshold, the purity of the population is almost 100%. When the electron beam energy is lowered, but still above the Na-like threshold, some purity is lost, as the Na-like ions represent around 20% of the total population. This is expected, as the collisional direct ionization cross section increases with the incident free

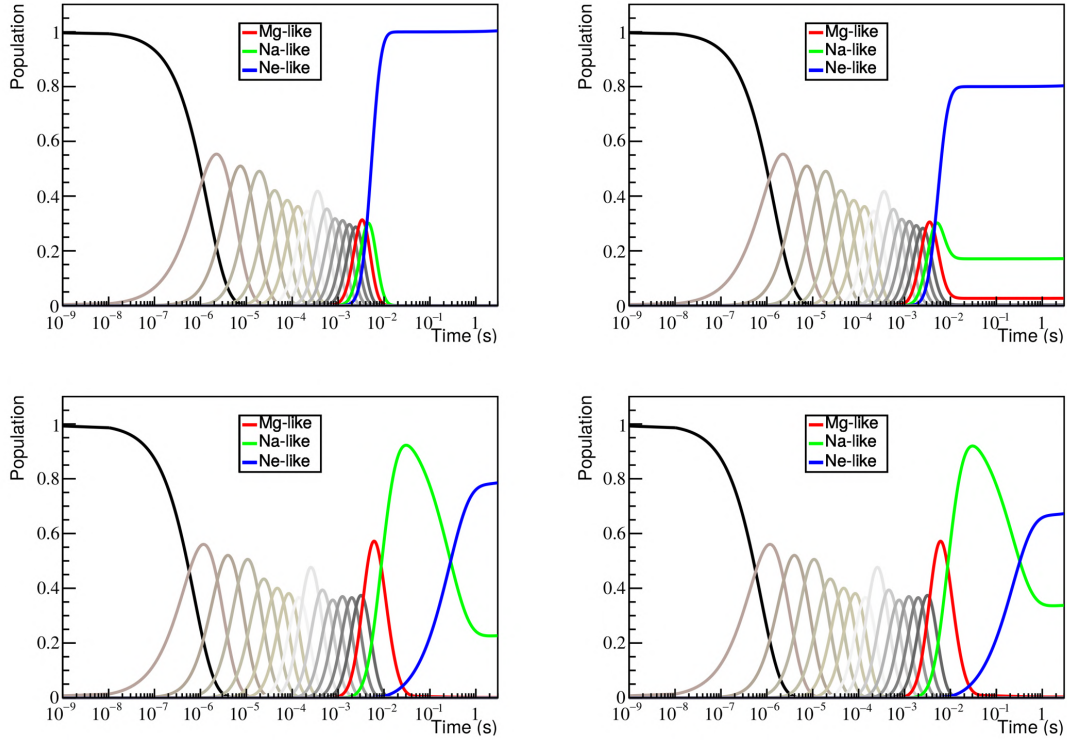


Figure 4.7: Populations of charge states of Fe as a function of time. The top and bottom figures correspond to beam energies of 1.15 keV and 0.49 keV, respectively. Left and right figures correspond to pressure conditions of  $P_{\min}$  and  $P_{20\%}$ .

electron kinetic energy, thus the process being more efficient with high energies. On the other hand, increasing the pressure conditions also increases the charge change between Ne-like ions and hydrogen atoms, leading to a smaller population purity as well. Since the charge exchange process affects all the ion species, the Na-like population not only increases from Ne-like ions with CX, but also transfer ions to the Mg-like population. This effect is apparent in this figure, as the simulation with 1150 eV and high pressure presents a small, but non negligible, amount of Mg-like ions in equilibrium conditions.

#### 4.2.1 EBIT plasma and spectra simulations

During the probing stage of the EBIT experiments, the DR process dominates the resulting spectra. The DR process is a recombination process, so the population of the ion that is being studied decreases during the time that the electron beam spends with the respective energy near the DR resonant energy. If this time is too long, the population of the ion charge state in study may decrease significantly, compromising the DR measurements, since the DR emissions collected in the EBIT are proportional to the ion population. This effect is known as dielectronic recombination depletion, and has to be accounted for to make an accurate analysis of the results. The charge state dynamics simulations are a useful tool to study the impact this effect on the ion populations and



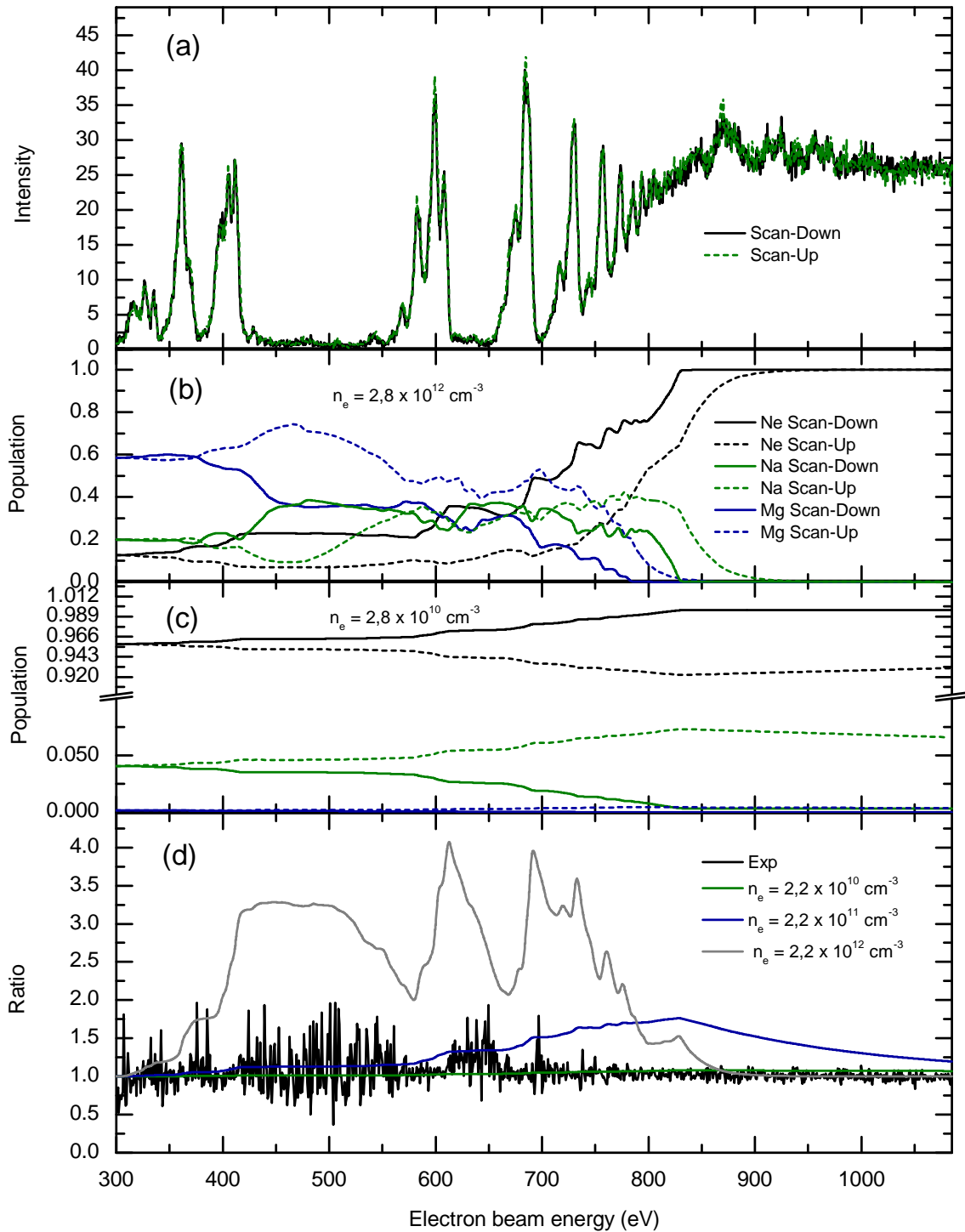


Figure 4.8: (a) Spectral maps observed at FLASH-EBIT by scanning upwards and downwards the electron beam energy. Simulations of Fe charge-state distributions as a function of the electron beam energy for effective electron densities of (b)  $2.8 \times 10^{12} \text{ cm}^{-3}$  and (c)  $2.8 \times 10^{10} \text{ cm}^{-3}$ . (d) Experimental ratio between downwards and upwards scans compared with simulations for different effective electron densities.

evaluate the impact of each experimental parameters in the resulting spectra. Figure 4.8 represents the results from several simulations of the population dynamics for the measurements of Fe Ne-like in the FLASH-EBIT. Subfigure (a) contains the experimental results obtain during the downwards and upwards scanning. The two types of measurement seem to be visually very similar, but the ratio between them was taken as a metric to evaluate the population depletion. Since both spectra were obtain in the same conditions, and the cross section of the atomic processes is the same, the ratio is only dependent on differences in the populations. In the subfigure (d), this ratio is very close to 1 in all the spectra structures, deviating only in the regions were there is only background in the spectra. This deviations can be attributed to variations in the background noise and may not be related to any difference in population. According to the equation (4.3), the rate of the DR process is proportional to the electron current density  $J_e/e$ . Although the electron beam current is measured in the experiment, from which the electron density can be derived, several works demonstrated that the effective electron density affecting the ions is usually a few orders of magnitude below the one measured experimentally through the current [22, 108, 109]. This phenomenon is explained by the fact that the ion cloud is much bigger than the electron beam volume and the effective interaction volume is given by the overlap between the cloud and the beam. The previously mentioned simulations were performed for several electron densities. High values lead to noticeable population depletions, as is the case present in the subfigure (b). The case present in the subfigure (c) represents the maximum electron density that results in DR depletion sufficiently low to be comparable to experimental results. This is apparent on the last subfigure, where only the ratio of the latter case can accommodate the experimental results. As such, not only there were no observable DR depletion, as the simulations demonstrated that the effective experimental electron density of the plasma was less than  $2.8 \times 10^9 \text{ cm}^{-3}$ .

Another important parameter to the model of the plasma is the pressure and the respective charge exchange cross section. The simulations output a simulated spectra by multiplying the population by all the radiative emission cross sections. Since all the charge states have different DR spectral lines, the relative intensities of every line can be used to evaluate the relative population in equilibrium and by knowing the electron density and doing multiple simulations, the pressure value can be estimated. In this case, several pressure values were used to simulate the experimental spectrum. Figure 4.9 shows the experimental spectrum in the LMM region, two simulations with different values of pressure and the relative resonant strengths for every line of the DR LMM process for Ne-like, Na-like and Mg-like ions. One of the most intense DR lines of the Na-like ion is located around the 380 eV region. This line is not resolved in the experimental results. With this is mind, several simulations with progressively lower values of pressure were performed until the resulting spectrum peaks of Ne-like and Na-like LMM DR matched the ones observed experimentally. This procedure allowed to infer that the experimental pressure conditions were such that the corresponding Ne-like charge exchange rate was less than  $0.046 \text{ s}^{-1}$ .

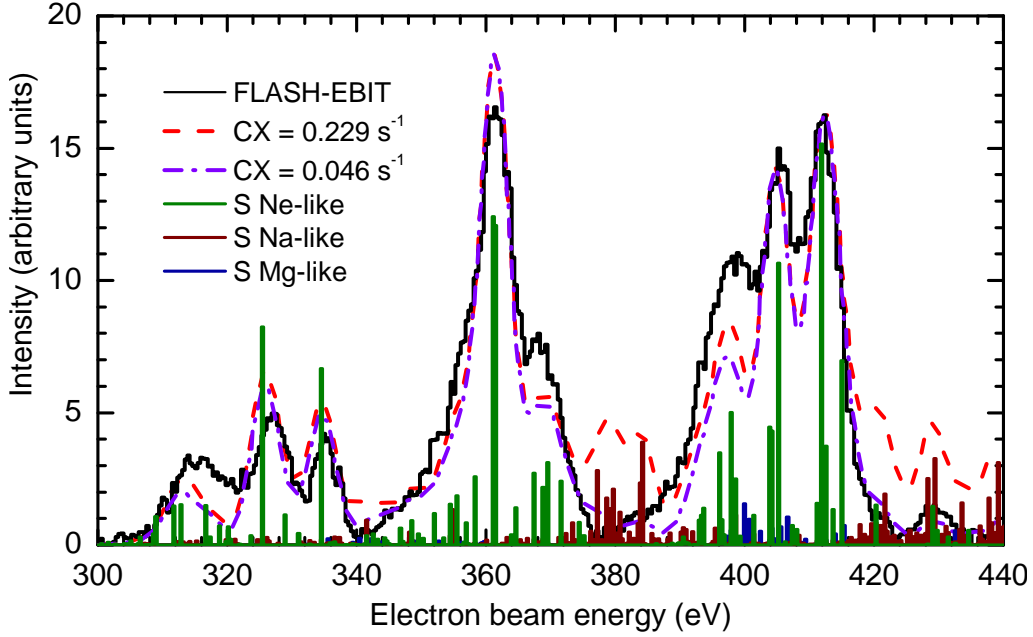


Figure 4.9: Theoretical resonant strengths for Ne-like, Na-like and Mg-like Fe ions and simulated fluorescence yield under charge-exchange rates of  $0.229 \text{ s}^{-1}$  and  $0.046 \text{ s}^{-1}$  in comparison with FLASH-EBIT data.

These simulations and procedures allow to derive all the important experimental parameters of the experiment and produce a realistic plasma model, capable of producing theoretical spectra comparable to experimental results.

#### 4.2.2 Spectral time evolution simulations

The experimental setup of the PolarX experiment opens the door to study the charge state dynamics directly from the obtained spectra, as its evolution is recorded as a function of time. When the electron beam energy is stationary in a DR resonant energy, the population of Ne-like ions decays due to the recombination process. By approximating the rate of population change to a value only dependent on the DR process,

$$\frac{dN_{Ne}}{dt} \approx -\frac{J_e}{e} \sigma_{Ne}^{DR} N_{Ne}. \quad (4.6)$$

In this case, this approximation is reasonable because in the LMM region, there is no Ne-like population loss due to ionization, so only the recombination and charge exchange terms of the equation (4.1), in respect to the Ne-like population, are non-zero. Furthermore, there are no F-like ions and the population of Na-like ions at  $t = 0\text{s}$  is relatively small. Moreover, the DR cross section, in the respective resonances, is much greater than the RR and CX cross section. This approximation can only be done for initial small periods, as the recombination of Ne-like ions produces Na-like ions that have x-ray emissions not accounted for in equation (4.7). The population, and consequently the radiative

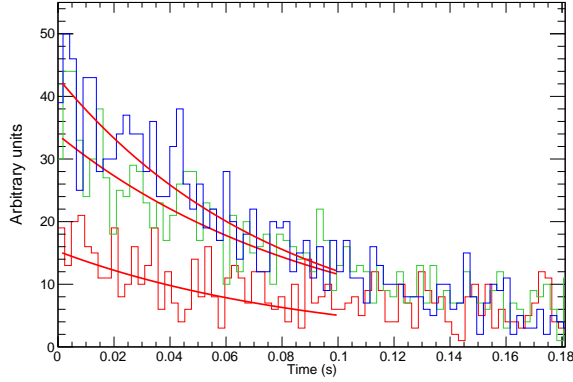


Figure 4.10: Example of the projection of 3 of the most intense DR peaks of the PolarX-EBIT experiment over time with exponential fits (red).

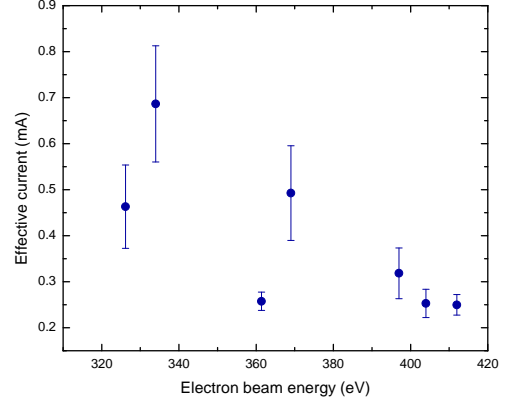


Figure 4.11: Effective current extracted from each of the exponential fits of the several resonant structures.

emission, decays in an exponential manner:

$$I \approx I_0 \exp\left[-\frac{J_e}{e} \sigma_{Ne}^{DR} t\right], \quad (4.7)$$

where  $I$  and  $I_0$  are the radiative emissions at a time  $t$  and at a time  $t = 0$ . An exponential fit was adjusted to the decay of every major Ne-like LMM DR peak of the experimental data.

Figure 4.10 shows the projections of the decay of the 7 most intense peaks of the experimental data along the time axis. As the evolution of the Ne population can only be approximated by the equation (4.6) when the ion cloud purity is high, the exponential fits were only applied to the first 100 ms of the decay. The red curves represent the result of the fitted functions. Using the relation (4.7), the effective electron current was determined for each peak. For this calculation, the cross section values were calculated with FAC. The obtained effective currents are represented in figure 4.11, where the uncertainty is derived from the uncertainty of the fit procedure. The values corresponding to the peaks with a more intense DR cross section seem to agree with each other, while the remaining appear to deviate. As the uncertainty varies greatly between measurements, a weighted average was taken to get an overall electric current value. The mean value was defined as

$$\bar{I} = \frac{\sum_i \frac{I_i^2}{\mu_i^2}}{\sum_i \frac{1}{\mu_i^2}}, \quad (4.8)$$

where  $\bar{I}$  is the average electric current and  $I_i$  and  $\mu_i$  are the individual values of electric current and the respective uncertainty. The uncertainty of the weighted average is given by

$$\bar{\mu} = \sqrt{\frac{1}{\sum_i \frac{1}{\mu_i^2}}}. \quad (4.9)$$

The obtained value of electric current is

$$\bar{I} = (0.27 \pm 0.02) \text{ mA.}$$

For an electron beam with a radius of  $30 \mu\text{m}$  with a mean energy of 400 eV, this value of current corresponds to an electron density of  $5.02 \times 10^{10} \text{cm}^{-3}$ .

The previous simulations were modified to attend the experimental conditions of the PolarX measurements. After achieving equilibrium with the breeding energy at 1.2 keV, the energy was set to a probing energy during 2 s to record the charge state dynamics and the corresponding radiative emissions. This setup was repeated to cover all the electron beam energy from 300 to 500 eV with a 1 eV resolution. The resulting two-dimensional map of the emission in function of electron beam energy and time is compared in the Figure 4.12 to the experimental results (a). This new simulation was performed with different values of pressure until the population decay was similar in both cases. To make these results more accurate, the DR-LMM process of the Al-like iron were also included.

The results of this simulation demonstrate that this kind of simulations are capable of producing realistic plasma models with spectra comparable to the experimental measurements. All the 7 Ne-like peaks have a realistic decay, with a decay time of around 100 ms. After this time, the Na-like emissions have a growth until around 600 ms, beginning to decay afterwards. At the higher end of the energy spectrum, there is a steady growth of emissions from Mg-like and Al-like ions, also observed in the experimental spectrum. The experimental results have an initial background that also decays over time. This characteristic is not present in the simulations, and there is no clear explanation for this phenomenon.

### 4.3 Preliminary Kr charge state simulations

Preliminary calculations and simulations were also performed for the Kr plasma. This included CI, EA and RR calculations for Kr Ne-like, Na-like, Mg-like and Al-like. The DR process was also calculated for this set of ions. For the Ne-line, these calculations extended from LMM to LMT, while for the rest was only LMM, LMN and LMO.

The experimental scheme of the FLASH-EBIT was simulated, with an energy breeding of 2500 eV and a scan from 2500 eV to 400 eV. In the experimental results in the next chapter, there is no significant difference between the upwards and downwards scans, thus the electric current in the simulations was such that there was no DR depletion (0.2 mA). Figure 4.13 shows four simulations of the Kr plasma, with the population fraction evolving from neutral to mostly composed of Ne-like, Na-like and Mg-like ions. The only difference between the several simulations was the pressure and, consequently, the CX rates.

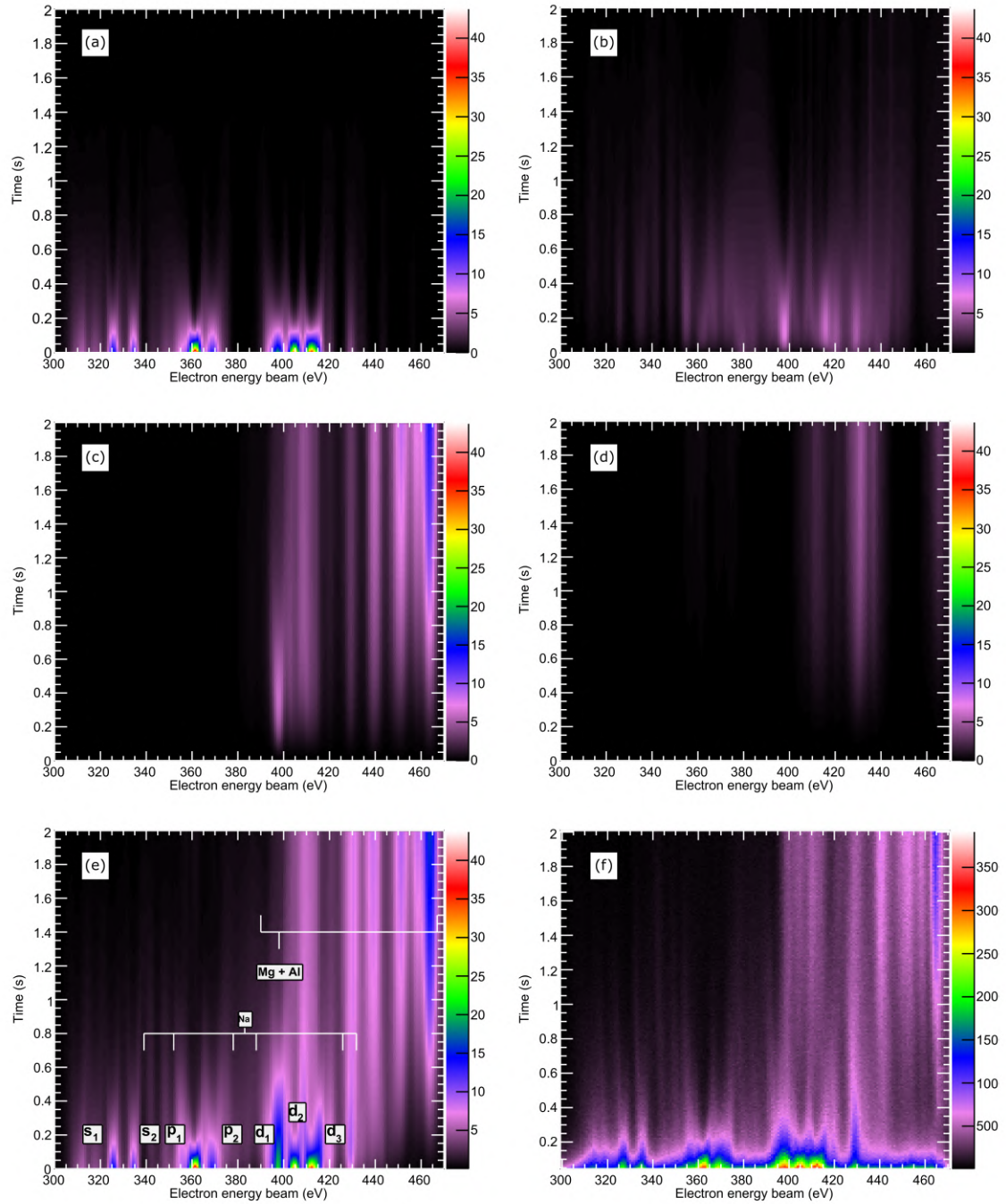


Figure 4.12: Simulation of the DR emission at the experimental conditions of the PolarX-EBIT for (a) Ne-like, (b) Na-like, (c) Mg-like, (d) Al-like Fe. (e) represents the simulations of the total emission and (f) is the measured experimental spectrum over time. The simulations confirmed the identification of lines caused by Na-like, Mg-like and Al-like Fe ions that appeared as the Ne-like ions decayed over time.

### 4.3. PRELIMINARY KR CHARGE STATE SIMULATIONS

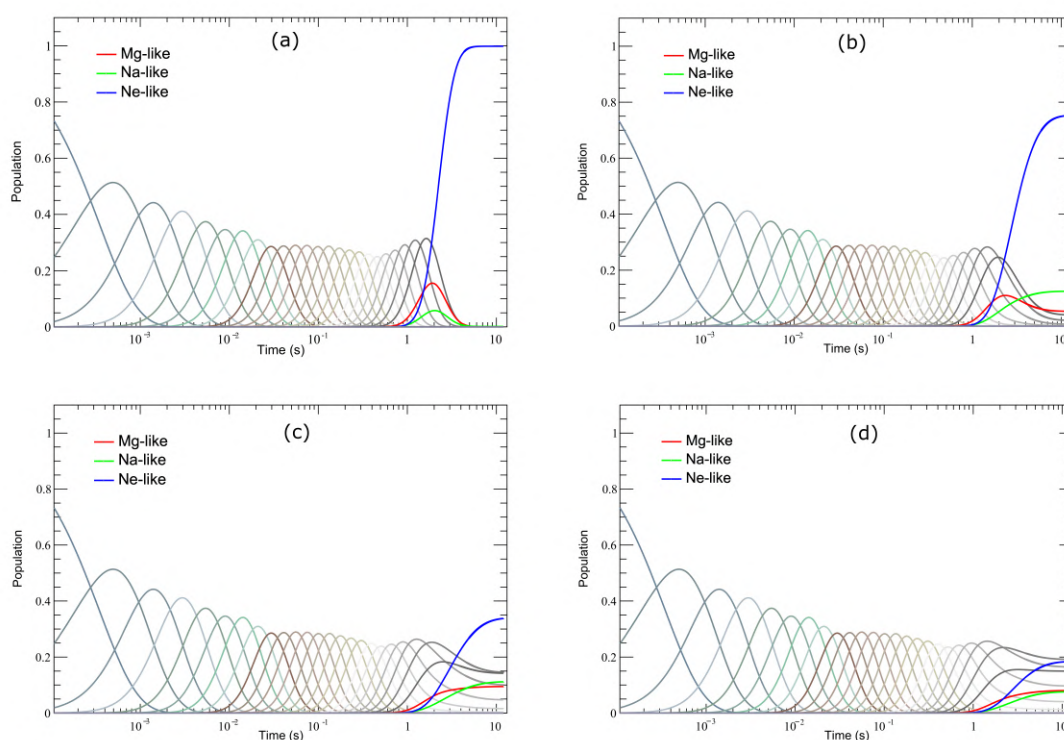


Figure 4.13: Simulation of the several charge state populations of Kr over time in the FLASH-EBIT conditions. The subfigures (a), (b) (c) and (d) correspond to simulations with pressures of  $2.5 \times 10^{-10}$  mBar,  $2.5 \times 10^{-8}$  mBar,  $1.0 \times 10^{-7}$  mBar and  $2.0 \times 10^{-7}$  mBar, respectively.





## EXPERIMENTAL RESULTS AND DISCUSSION

In this chapter, the methods to analyse the spectra obtained from both the FLASH-EBIT and PolarX-EBIT are presented, as well as to the previously-obtained data at the TSR.

Partial results were already presented in the last chapter to compare to the time-dynamic simulations of the plasma at the PolarX experiment. Given that the SDD is sensitive to photon energy, 2d spectra of the emission as a function of the electron beam energy and the photon energy were also available. Figures 5.1 and 5.2 represent these maps obtained in the FLASH and PolarX EBITs, respectively.

In the first case, resonant structures are visible in the region between 300 eV and 1000 eV of beam energy and between 600 eV and 1400 eV of photon energy. At the photon energies between 700 eV and 900 eV, the DR-LM $n$  (with  $n = 1, 2, 3, \dots$ ) spans until around 800 eV of beam energy. In particular, the LMM structure is isolated and clearly resolved between 300 eV and 500 eV. The energy difference between consecutive LM $n$  structures diminishes for each  $n$  until several structures cannot be resolved as the binding energy of the  $n$  shell approaches the continuum. At this energy, the CE threshold is reached.

This threshold is represented by the right diagonal line in figure 5.1. At this line, the incident electron has a kinetic energy that is equal to the excitation energy of a bound electron. Therefore, the second one can excite with kinetic energy being totally transferred and barely above electron recombination. The excited electron then emits a photon with the same energy as the initial kinetic energy. It is observed in the figure that at the CE threshold the photon energy is the same as the kinetic energy. From this point onwards, the incident electron has always higher and enough energy to directly excite a bound electron. In this case, the scattered electron carries the remaining energy. As the deexcitation path of the bound electron remains the same, the direct excitation process

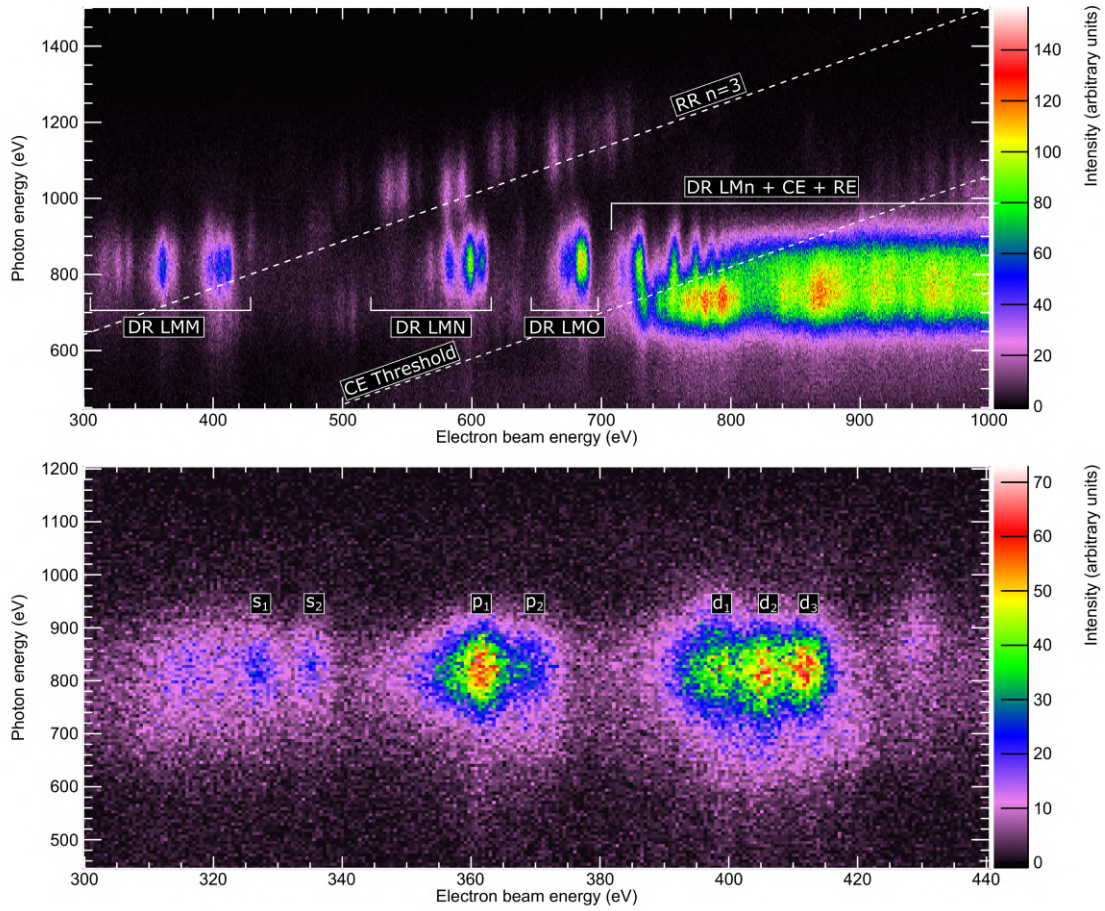


Figure 5.1: Experimental results from the FLASH-EBIT experiment. It is displayed in the form of a 2D map of the fluorescence yield as a function of the electron beam energy and photon energy. The top plot shows the complete measurements, while the bottom plot is an amplification of the DR-LMM region.

creates a band of emission on the right side of the CE threshold line. Here, it corresponds to the  $n = 3$  to  $n = 2$  transitions in the photon energy region (750 to 850 eV).

The direct CE has a non-resonant cross section, yet some resonant structures are superimposed in this band in the 2D map. Those structures are given by the resonant excitation process. In this process, the free electron is recombined by dielectronic capture, but the resulting ion subsequently autoionizes into an excited state instead of a radiatively decay, as in DR process. The net result is the excitation of the initial ion in a resonant manner, resulting in resonant structures with photon emissions superimposed on the CE structure.

The bottom subfigure is an enlargement of the FLASH-EBIT measurements on the DR-LMM region. The seven peaks mentioned in the last chapter are clearly resolved and labeled in the figure. Figure 5.3 shows the FAC calculation broadened to the FLASH-EBIT experimental widths. A first look shows a good agreement between them and a deep analysis was made with a fit procedure. More peaks with lower intensity are present in

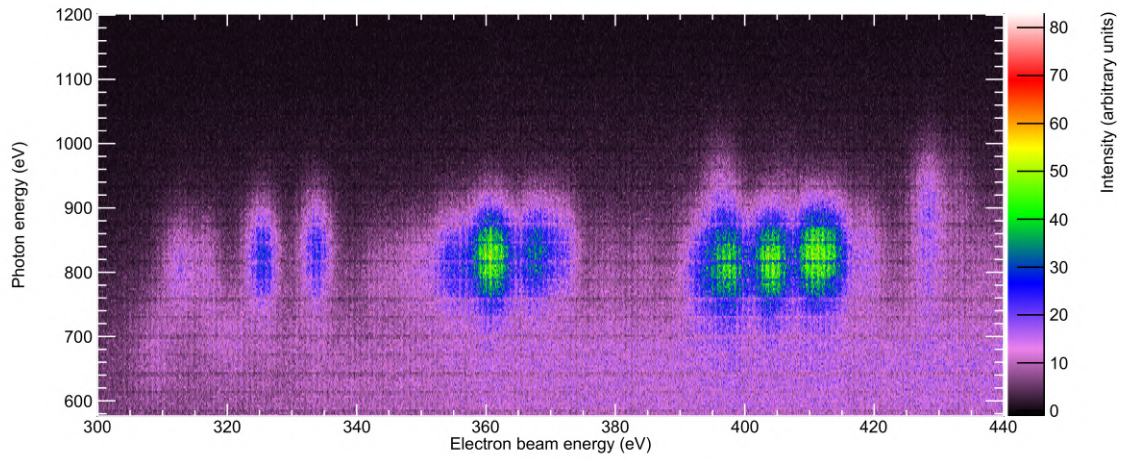


Figure 5.2: Experimental results from the PolarX-EBIT experiment, displayed in the form of a 2D map of the fluorescence yield as a function of the electron beam energy and photon energy. It only contains the first 50 ms of the probing period to maintain an high Ne-like pure population spectrum

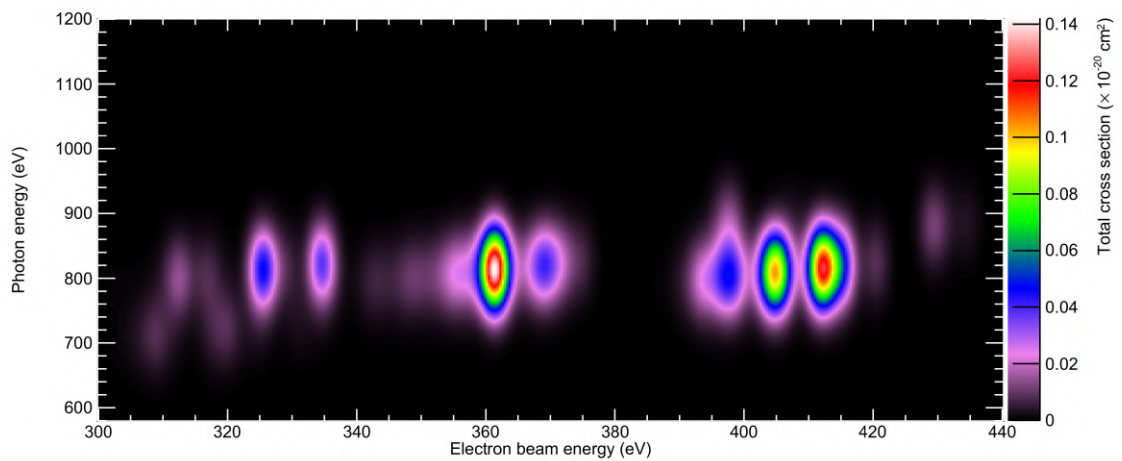


Figure 5.3: FAC calculations presented in the same format as the results from the PolarX-EBIT experiment. The 2D histogram has been broadened to match the experimental spread of the photon energy and electron beam energy.

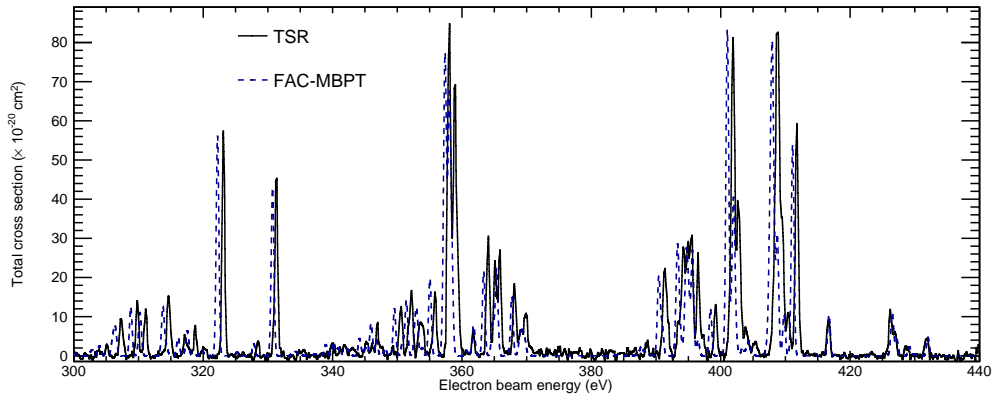


Figure 5.4: Original TSR measurement on the LMM region, plotted against the FAC-MBPT calculation broadened to a similar energy spread. Note that the TSR values retained the original calibration and broadening.

the theoretical results. However, the measured statistics and resolution were not enough to resolve them, e.g. the ones between 300 eV and 320 eV. These measurements have an electron beam energy spread with a FWHM (Full-Width-Half-Maximum) of around 5.4 eV. The SDD had a photon energy spread around 100 eV, which precludes a precise analysis in this axis.

Figure 5.2 shows the DR-LMM measurements performed at the PolarX-EBIT, where the electron beam energy spread was smaller than the FLASH-EBIT counterpart. In this case, the FWHM of the electron beam energy was around 3.5 eV. The photon energy resolution was similar to the FLASH-EBIT case. The same structures are present in this case. It is worth noting that in this case the  $p_2$  and  $d1$  structures are more clearly resolved. Nevertheless, the energy scheme of this experiment resulted in higher content of Na-like ions overall. The scheme was more focused on the dynamics of the charge state populations over time, so an increase of Na-like ions is expected over time. To have a spectrum corresponding only to the Ne-like Fe, the time of acquisition has to be cut short to exclude the presence of other types of ions. Consequently, there is a compromise between the amount of data used to have a good statistical measurement and the time at which the data acquisition is restricted. For this case, only the events registered in the first 50 ms of the probing time were considered.

Due to the directionality of the electron beam, a correction factor had to be taken into account. As explained in chapter 2, the emitted radiation is polarized and anisotropic, thus the correction factor  $W(90^\circ) = 3/(3 - P)$  was applied, where  $P$  is the polarization for a specific radiative transition. The total cross section was then obtained by

$$\sigma = 4\pi \frac{I^{90^\circ}}{W(90^\circ)}, \quad (5.1)$$

where  $I^{90^\circ}$  is the observed DR intensity. The calculated values of  $P$  were taken from the paper preceding this work [37], which are in agreement with the measurements made by

Chen et al. [110].

Previous measurements of the DR in Fe XVII taken by [105] in the TSR were also included in this analysis. Figure 5.4 shows the TSR data with the original energy calibration compared to the FAC-MBPT calculations (broadened accordingly). This figure presents a reasonable agreement between the new calculations and the old measurements, apart from the energy shift present across all the spectrum. To make these results more comparable to the EBIT ones, the spectrum was broadened to have a similar energy spread, resulting in a spectrum where, similarly to the rest of the results, only 7 resonances are clearly resolved.

## 5.1 Fit procedure

To analyse the LMM region, the 2D spectra were projected in the electron beam energy axis. Only the region of interest of this region on the photon energy axis was considered. The resulting 1D spectra were fitted with linear combination of Gaussian functions,

$$f_{\text{fit}} = \sum_i A_i \exp\left\{-\frac{1}{2} \frac{(E_e - \mu_i)^2}{\sigma^2}\right\}. \quad (5.2)$$

The subscript  $i$  identifies a specific Gaussian and  $A_i$  and  $\mu_i$  are the respective amplitude and mean value. Although the DR process has a Lorentzian profile, the electron beam energy has a gaussian distribution. For this cases, a Voigt profile, which is defined by the convolution of the Lorentz distribution and the Gaussian distribution, would be suitable for the fit function. Nevertheless, the electron beam energy spread is several orders of magnitude greater than DR natural width, resulting in a profile close to the Gaussian. To simplify the fit procedure, only Gaussian profiles were used. From now on, these Gaussians will be referred to as peaks or lines. The quantity  $\sigma$  is the same for all the constituents, as it is defined by the standard deviation of the electron energy profile.

Due to the high number of resonances present in the region (more than 300), the number of lines can be determined with the help of the FAC calculations. For each spectrum, the theoretical histogram is rebinned in such way that the bin width is equal to the FWHM of the experimental peaks. The number of bins corresponds to the number of Gaussian functions included in the fit function. The number of free parameters is high, and certain constraints have to be applied to avoid unrealistic results. The well resolved experimental peaks were considered as free lines, and the rest were considered as fixed energies. For the case of the free lines, their respective position was a free parameter restricted to the respective theoretical bin limits. As for the other lines, their position was fixed at a random position inside their respective bin. The fit procedure was applied several times, generating random positions for the fixed lines for every fit. It was taken as the final fit the result that yielded the smallest  $\chi^2$ . On both the EBIT's measurements, a small linear background was removed before the fit procedure was applied.

In past works, the RR theoretical cross section was used to calibrate the intensity of experimental spectra [111, 112]. In this case, this was not possible, as RR cross section is too negligible to be measured. The spectra intensities were thereby calibrated with the most intense theoretical DR-LMM resonance. The energy calibration was also made with those calculations. As a result, there were multiple possible calibrations for each of the theoretical calculations.

The best fit for each of the experimental spectra is represented in Figure 5.5. Note that the different data was obtained with different electron energy spread, so the number of resonances varies between subfigures. The green lines represent the peaks with a free positional parameter, labeled in the subfigure (b). To simplify the extracted data, only the values for these lines were tabulated. The red lines represent the peaks with a fixed position in the fit procedure.

## 5.2 DR resonant energy and strengths

As stated previously, calculations of the DR-LMM structure were made with FAC, as well as FAC-MBPT and MCDF. The best fits of the experimental data were calibrated with these three calculations. The intensity was always calibrated by the  $d_3$  peak and the electron energy axis was calibrated with the  $p_1$  and  $d_3$  lines. For each of the experimental measurements, all the theoretical results were broadened with a width corresponding to the respective experimental data. The same fit procedure was applied to the theoretical results. This was made to facilitate the comparison between theory and experiment. Due to the energy spread of the electron beam, the resolved lines are actually composed by the corresponding free line and several fixed lines. The fit of the broadened theoretical calculations ensures that the same mixing of lines is present in both theoretical and experimental results, enabling a fair comparison between them. Figure 5.5 represents the fit results for the measurements in the FLASH-EBIT, PolarX-EBIT and TSR. The green lines are the free peaks and the red lines are the fixed peaks.

Table 5.1 displays the energy positions of the resonances in all the experiments, as well as the ones obtained by fitting the theoretical calculations of FAC, FAC-MBPT and MCDF. The term Combined Energy (CE) was used to refer to the energy of the resonance after broadening, which is affected by all the surrounding small resonances. In these last columns, the percentage values inside the parentheses indicate the relative difference between the experimental and theoretical resonant energy, i.e.  $(E_{\text{exp}} - CE_{\text{theo}})/E_{\text{exp}}$ . The Nilsen calculation data was not included in this table because the resonance energy was not provided in the original reference work [106]. Since the measurements need an energy calibration before the fit, and the peak positions are different for every type of calculation, the experimental results were calibrated with every theory presented. After each calibration and fit process, the values of the different experiments for each peak were average weighted by the uncertainty and the respective relative difference from the respective theory was calculated. The peaks  $p_1$  and  $d_3$  have no relative difference, as they were

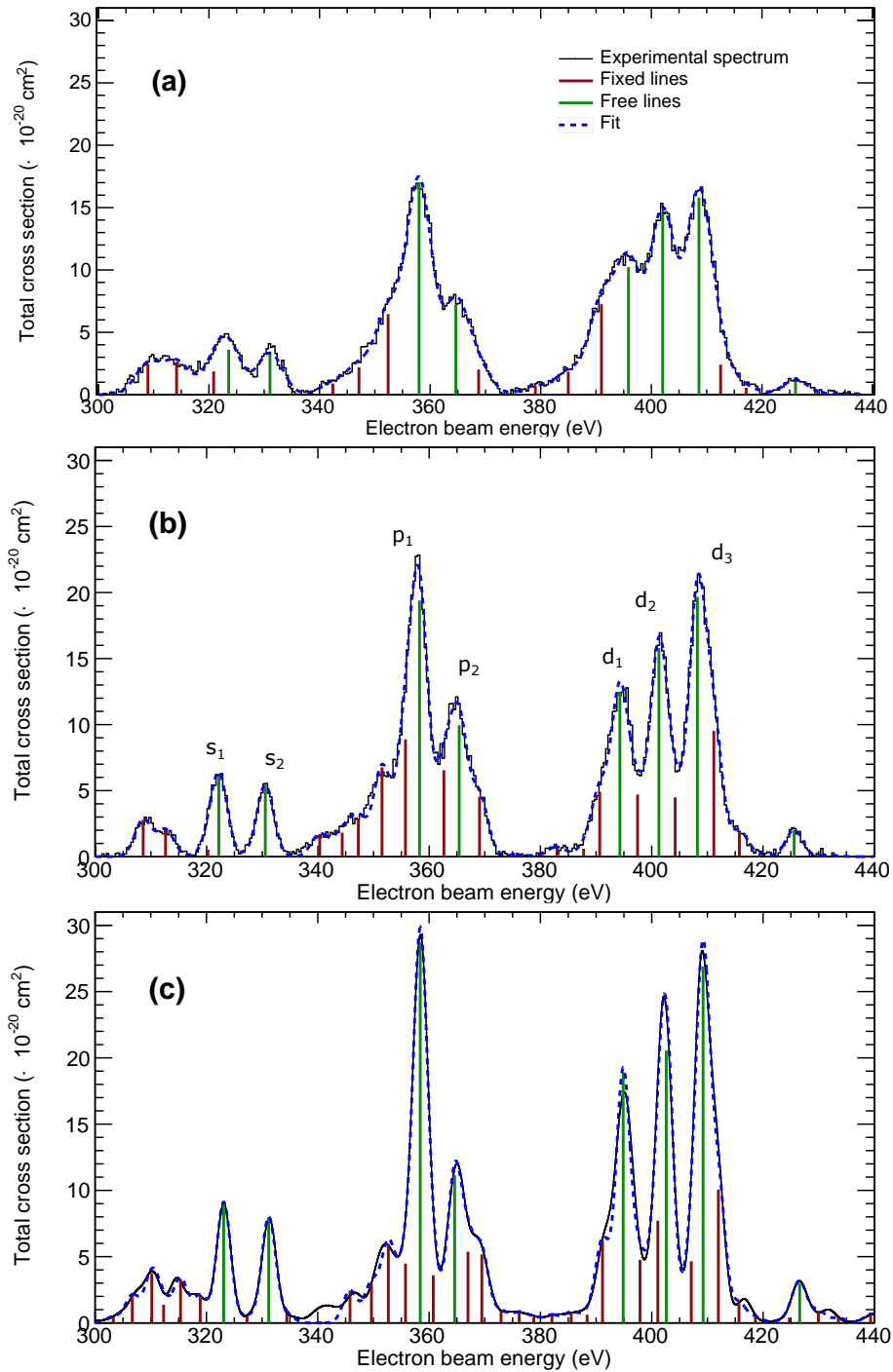


Figure 5.5: Experimental results from (a) FLASH-EBIT, (b) PolarX-EBIT, and (c) TSR measurements, respectively. Black curves represent the experimental spectra, the fitting model is shown in blue. Vertical lines mark position and amplitude of each DR LMM resonance (red: fixed energies, green: free energies in the fitting procedure).

Table 5.1: Experimental and theoretical (FAC-Cl, FAC-MBPT, and MCDF) DR resonance energies. Round brackets: relative difference in percent between measured and theoretical positions, with each measurement calibrated to the respective  $d_3$ -feature calculation.  $CE$  stands for combined energy values obtained by fitting the synthetic spectra (all energies given in eV).

Label	$E_{\text{FLASH}}$	$E_{\text{PolarX}}$	$E_{\text{RSR}}$	$CE_{\text{FAC}}$	$CE_{\text{FAC-MBPT}}$	$CE_{\text{MCDF}}$
$s_1$	$322.8 \pm 0.9$	$321.5 \pm 0.03$	$323.2 \pm 0.2$	$325.64$ (-0.15%)	$322.24$ (-0.23%)	$321.81$ (0.74%)
$s_2$	$330.7 \pm 0.3$	$330 \pm 0.03$	$331.2 \pm 0.1$	$334.75$ (-0.31%)	$330.65$ (-0.18%)	$328.55$ (1.24%)
$p_1^a$			$358.3 \pm 0$	$361.52$	$357.8$	$359.60$
$p_2$	$364.1 \pm 0.3$	$364.7 \pm 0.02$	$364.73 \pm 0.1$	$369.18$ (-0.2%)	$365.31$ (-0.17%)	$364.93$ (0.62%)
						$371.52$
$d_1$	$395.7 \pm 0.4$	$394.1 \pm 0.03$	$394.7 \pm 0.03$	$397.71$ (0.05%)	$394.44$ (-0.08%)	$395.95$ (0.005%)
$d_2$	$401.9 \pm 0.3$	$401.6 \pm 0.02$	$402.6 \pm 0.1$	$404.87$ (0.13%)	$401.32$ (0.06%)	$402.95$ (0.01%)
$d_3^1$			$409.14 \pm 0.04$	$412.37$	$408.55$	$410.18$

<sup>a</sup>Peak used for energy calibration.



Table 5.2: Experimental resonant strengths ( $10^{-20}$  cm<sup>2</sup>eV) compared to values obtained with FAC, MCDF (this work) and reported by Nilsen [106]. Listed experimental cross-sections were calibrated with the FAC-MBPT theoretical value of line d<sub>3</sub>. Round brackets: relative difference in percent between measured and theoretical resonant strengths, with each measurement calibrated to the respective d<sub>3</sub> - feature calculation.

Label	S <sub>FLASH</sub>	S <sub>PolarX</sub>	S <sub>TSR</sub>	S <sub>EXP</sub>	S <sub>FAC</sub>	S <sub>FAC-MBPT</sub>	S <sub>MCDF</sub>	Ref. [106]
s <sub>1</sub>	23 ± 5	26 ± 4	28 ± 6	25 ± 3	33.99 (-31%)	28.72 (-13%)	8.17 (71%)	36.95 (-35%)
s <sub>2</sub>	18 ± 4	21 ± 4	25 ± 5	21 ± 2	27.87 (-31%)	23.28 (-12%)	26.27 (-10%)	24.24 (-7%)
p <sub>1</sub>	87 ± 16	82 ± 13	98 ± 20	87 ± 9	96.62 (-8%)	85.18 (2%)	84.4 (15%)	73.58 (22%)
p <sub>2</sub>	34 ± 7	41 ± 8	35 ± 7	37 ± 4	29.53 (21%)	24.12 (34%)	73.94 (-83%)	17.95 (54%)
d <sub>1</sub>	53 ± 10	48 ± 8	54 ± 11	50 ± 5	41.67 (20%)	47.29 (7%)	53.63 (6%)	21.68 (60%)
d <sub>2</sub>	76 ± 14	63 ± 11	64 ± 13	67 ± 7	74.29 (-9%)	68.44 (-3%)	60.2 (19%)	56.85 (20%)
d <sub>3</sub> <sup>a</sup>			90 ± 18	87 ± 9	88.76 (0.3%)	86.14 (1%)	101.96 (-4%)	95.84 (-2%)

<sup>a</sup>Peak used for cross-section calibration.

the reference for the calibration, therefore implying a 0% expected relative difference. The experimental values displayed in the table correspond to the ones calibrated with FAC-MBPT. The TSR spectrum was not recalibrated. This provides experimental results with an independent energy and intensity calibration. In general, all theories presented appear to be in good agreement with the experimental results, with the absolute value of most of the relative differences always within 1%. The MCDF calculations seems to describe better the positions of the  $d$  – manifold, while both FAC and FAC-MBPT show improvements on the  $s$  – manifold structure, region where MCDF presents the biggest differences. The experimental uncertainties were based on the error of the parameters that resulted from the fitting procedure.

Table 5.2 completes the analysis of the same resonances by describing the results of the resonant strengths. The integral of a gaussian function takes the general form

$$\int_{-\infty}^{\infty} A \exp\left\{-\frac{1}{2} \frac{(E_e - \mu)^2}{\sigma^2}\right\} dE_e = A\sigma\sqrt{2\pi}, \quad (5.3)$$

with which the value of resonant strength and the respective uncertainty can be extracted from the parameters of the fit function and the propagation of their respective uncertainties. The column  $S_{\text{exp}}$  corresponds to the average of the experimental values weighted by the uncertainty. The FLASH-EBIT resonant strengths uncertainties were estimated to be on the level of around 20%, 17% for the case of the PolarX-EBIT. Once again, the TSR values retained the original calibration, and the respective uncertainties correspond to the 20% uncertainty in cross section quoted by the authors. In the combined experimental values, the uncertainty was on the level of  $\sim 10\%$ . Similarly to the last case, the FLASH-EBIT and PolarX-EBIT results were calibrated for each of the theoretical results in order to compute the relative difference expressed in side the parentheses. In this case, the accuracy of the calculation varies significantly between them. This aspect is important, since the resonant strengths dictates the dielectronic recombination rate of an ion in a plasma, therefore playing an important roll in plasma modeling. The Nilsen calculation has the greater differences across the board, having most of the values in the order of tens per cent. There seems to be a tendency where the less intense lines are in less agreement with experiments then the rest of the resonances. The FAC calculations present a small improvement in all resonances except  $s_2$ . Intense lines, namely  $p_1$  and  $d_2$ , have a relative difference below 10%. FAC-MBPT shows improvements to the FAC overall. The  $s_1$  and  $s_2$  present less then half of the difference relative to the last case, the  $p_1$  resonance has nos a difference of just 2% and the  $d_1$  and  $d_2$  lines are now much closer to the experimental results. Meanwhile, the  $p_2$  resonance persists to be not well described. As for the MCDF case, there seems to be a reasonable agreement between experiment and theory, except for the  $s_1$  and  $p_2$  lines, where the absolute relative difference, for both cases, surpasses 70%. The reason for the problems of the MCDF calculations might reside in the MCDFGME package used not being able to generate reliable Auger rates to other configurations beyond single coupling, something that would be necessary to improve

both the centroid positions and the DR resonant strengths.

Figure 5.6 summarizes all the results. The first subfigure represents the relative difference values of every peak for each of the theoretical calculations, where the error bars represent the relative uncertainty of the theoretical fits, as a function of the electron beam energy. The blue transparent rectangles that vertically align with the horizontal axis represent the experimental results, i.e. vertically represent the relative uncertainty of the resonant strength and horizontally the peak position uncertainty. Note that the widths were multiplied by a constant to be more clear, the real position uncertainties are much smaller, as seen in the table 5.1. It appears that all the theories overestimate the strengths of all the  $s_n$  resonances, but underestimate the  $p_n$  resonances, while mostly agree with experiment in the  $p_n$  resonance region. The subsequent 4 subfigures represent the PolarX data calibrated by the FAC, FAC-MBPT, MCDF and Nilsen results. The cross section of each of the respective theories is also present, as well as the TSR measurements (not recalibrated in any way). In general, all theories fail to represent the  $p_2$  line adequately, always underestimating the respective strength. In addition, both the EBIT experiments disagree with the TSR measurements in this resonance. As the simulations exclude possible population dynamics influencing the observed spectra, there is no available explanation for this problem at the moment. In the transition from FAC to FAC-MBPT, the  $d_1$  line, which initially is poorly described, reaches a reasonable level of agreement. The MCDF subfigure reveals some problems embedded in the previously mentioned calculation. Firstly, the  $s_1$  and  $s_2$  lines are closer than expected, and the  $s_1$  line has an amplitude much lower than the experimental one. Secondly, the resonances that form the  $p_2$  peak appear to be divided into two separate peaks rather than one, as is the case for the remaining theories. In this case, the tabulated relative difference for the  $p_2$  peak was calculated using the sum of these two new peaks, hence the large  $-83\%$  difference present in the table. Finally, the  $p_1$  and  $d_2$  lines are greatly underestimated, which contrasts with the fairly good agreement achieved in the FAC and FAC-MBPT calculations. There is also a resonance around 430 eV present in all the experiments and theoretical calculations that is absent in the MCDF cross section. The FAC-MBPT calculations are the ones that better describe the experimental results, giving resonant strengths that are within the error bars of the experimental measurements.

### 5.3 DR rates

The resonant strengths, combined with the resonant energies, were used to extract experimental DR rate coefficients with the aid of the expression (2.81). The experimental energies and strengths have been calibrated with FAC-MBPT. Three different electron temperatures ( $T_e = 100, 300, 2000$  eV) were chosen to calculate the the DR rate coefficients at several typical conditions (temperature below, close to and above the DR resonant energy). All the rate coefficients were summed, as individual resonances are blended and cannot be adequately distinguished. Table 5.3 summarizes the results. The

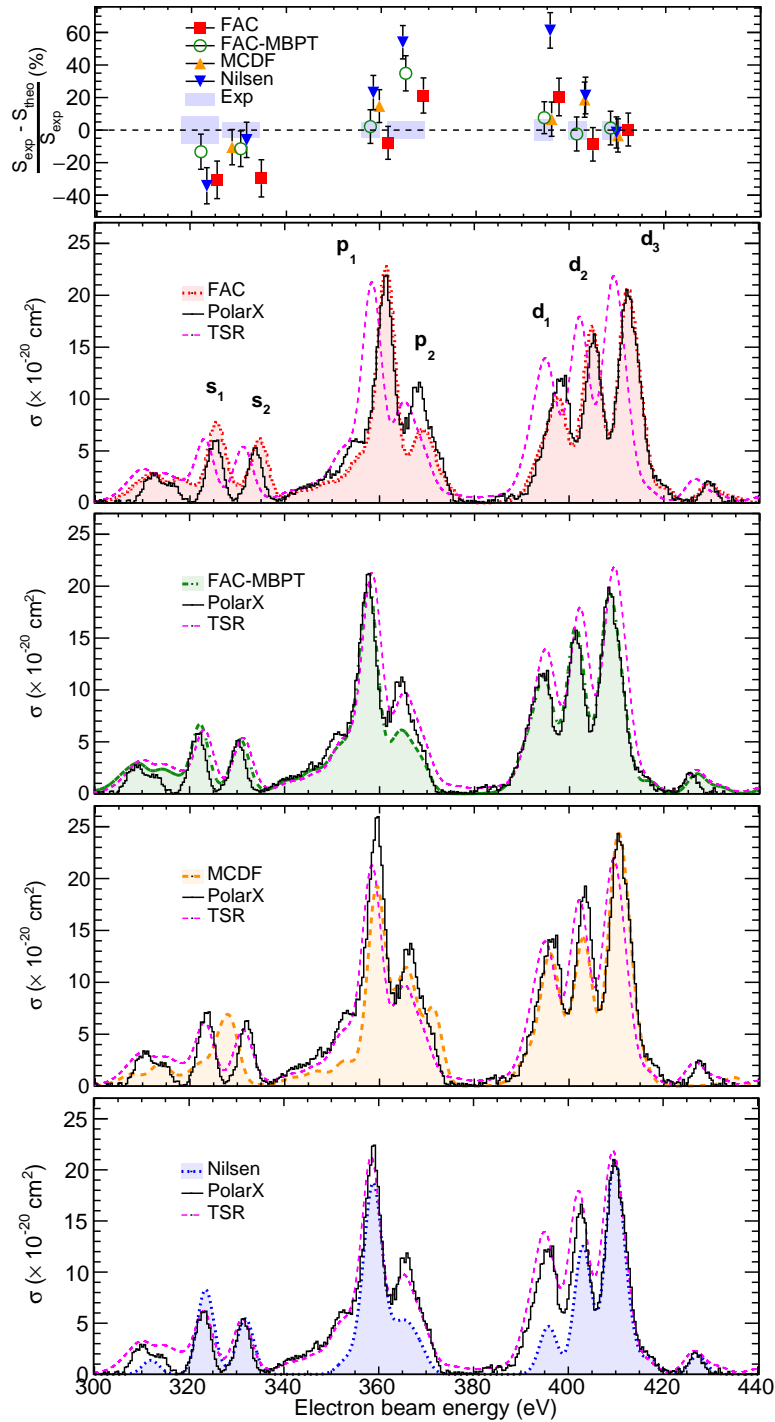


Figure 5.6: PolarX-EBIT and TSR measurements and theoretical total DR cross sections obtained using FAC, FAC-MBPT, MCDF, as well as literature values from [106]. Calculations were convolved with a Gaussian of 4.5 eV FWHM for the comparison. The top scatter plot compares theory and experiment.

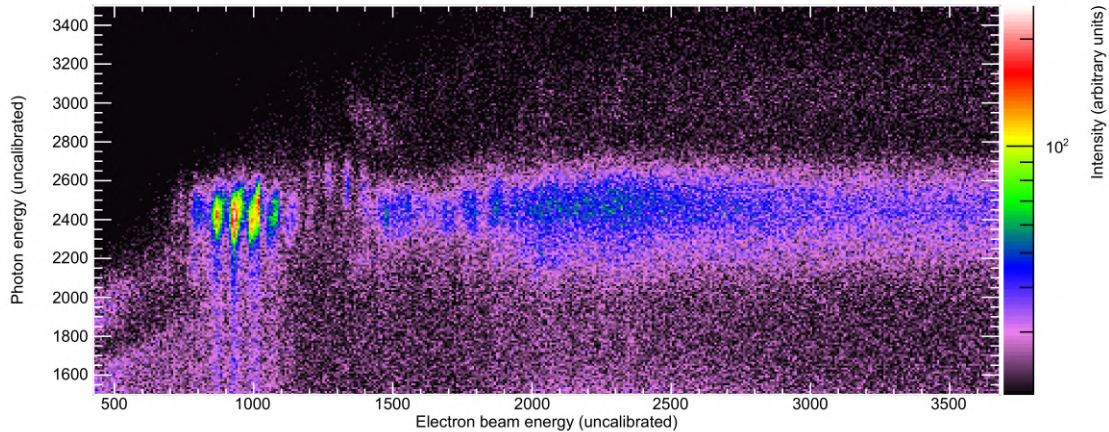


Figure 5.7: Experimental results from the FLASH-EBIT experiment with Kr, displayed in the form of a 2D map of the photon emission as a function of the electron beam energy and photon energy.

experimental values were compared with theoretical rate coefficients given by FAC-MBPT and MCDF, as well as the values available at the OPEN-ADAS<sup>1</sup> and AtomDB<sup>2</sup> databases. Calculations obtained with the AUTOSTRUCTURE [113] code were also included. To make a more in depth comparison, the theoretical calculations and database values were combined by the respective final-state configuration of the Na-like ion ( $3s$ ,  $3p$  and  $3d$ ). The total DR coefficient rates, resulting from the sum of all the resonances, are presented at the end of the table. The AUTOSTRUCTURE code calculations only provided the total values, instead of the separation by final-state configuration available at the AtomDB and OPEN-ADAS databases.

The MCDF and FAC-MBPT calculations agree with the experimental results within 3 to 8%. Discrepancies, however, have been found between OPEN-ADAS and the experimental results. The OPEN-ADAS overestimates the total value by as much as 40% compared to the experimental results. Comparing to the theoretical calculations, this overestimation is apparent for the  $p$  and  $d$  resonances, particularly in the temperature near the resonance energies. The AtomDB spectral modeling database also presents some significant discrepancies, showing as much as 49% of underestimation in respect to the experiments. Once again, this discrepancy is valid for both the  $p$  and  $d$  resonances. The calculations given by the AUTOSTRUCTURE code are more in line with FAC-MBPT and MCDF, giving relative differences around 10%.

Table 5.3: Experimental DR rate coefficients ( $\times 10^{-13} \text{ cm}^3 \text{ s}^{-1}$ ) for a few electron temperatures  $T_e$  (eV) compared to values obtained with OPEN-ADAS, FAC-MBPT, MCDF, by Nilsen [106] and by Zatsarinny *et al* [113]. The label indicates the orbital of the decoupled electron in the final state after DR emission.

Label	$T_e$	Exp	OPEN-ADAS	FAC-MBPT	MCDF	Ref. [106]	Ref. [113] <sup>a</sup>
s	100		5.88	7.69	5.45	5.65	
	300		11.7	12.8	9.71	9.51	
	2000		1.97	1.89	1.48	1.39	
p	100		14.0	15.7	14.2	8.97	
	300		42.8	31.9	30.0	19.1	
	2000		9.11	5.12	4.86	3.08	
d	100		13.5	15.4	13.4	8.94	
	300		52.6	41.3	37.5	25.9	
	2000		12.2	7.46	6.86	4.75	
total	100	36 ± 2	33.4	38.8	33.1	23.6	38.0
	300	81 ± 5	107.1	86.0	77.2	54.5	90.3
	2000	14 ± 1	23.3	14.5	13.2	9.22	15.3

<sup>a</sup>Only total DR rates are provided.

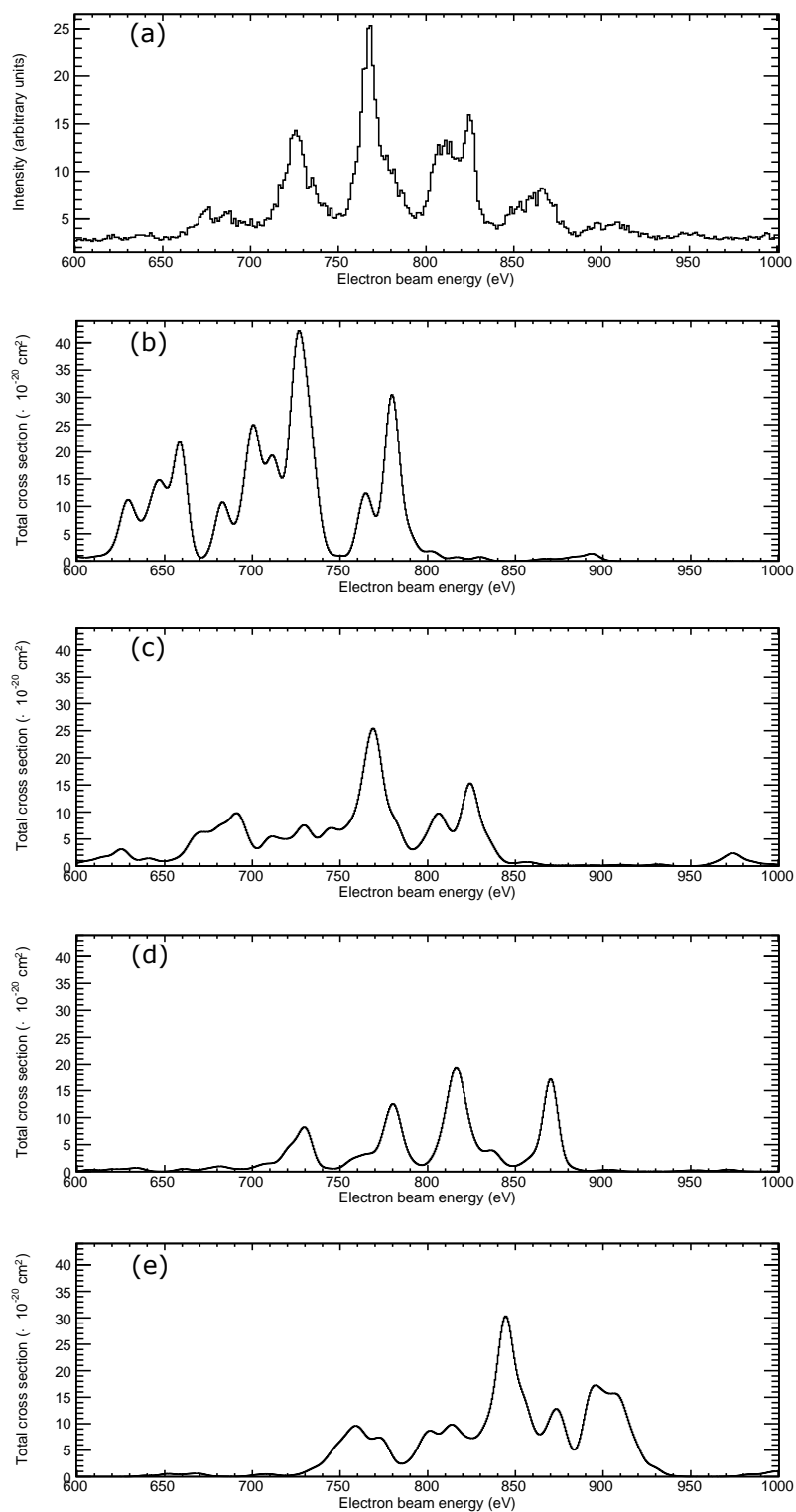


Figure 5.8: (a) Projection of the Kr spectra onto the electron beam axis. The subfigures (b), (c), (e) and (e) correspond to the FAC calculation of DR-LMM for Ne-like, Na-like, Mg-like and Al-like Kr, respectively.

## 5.4 Preliminary Kr results

Although no full analysis was done in the Kr case, the experimental results are presented as preliminary results. Figure 5.7 show the photon emission as function of the electron beam energy and photon energy (the spectrum is not calibrated). On the left end side, a resonant structure is clearly distinguishable. This structure should correspond to the DR-LMM structure. It was expected that, as was the case for the iron, the entire  $LMn$  would be visible. Instead, low intensity peaks are visible throughout the  $n = 3 - 2$  transition band, far smaller than what is expected from the DR structures of the Kr DR process. On the left end side of the spectrum, a non resonant structure is apparent, possibly attributed to the CE and RE of the Kr ions. Additionally, there is a faint diagonal line that crosses the LMM structure, corresponding to the RR band for the M-shell recombinations.

Figure 5.8 shows the projection of the experimental measurements on the electron beam energy axis (subfigure (a)). The subfigures (b), (c), (d) and (e) correspond to the FAC calculations of the DR-LMM for the Ne-like, Na-like, Mg-like and Al-like ions. There is no good match between the experimental results and the Ne-like calculations. Moreover, some peaks appeared to align correctly with the Na-like results, so they were used to calibrate the electron beam energy of (a). Furthermore, none of the calculations describe the experiment correctly, but all seem to have resonances that are represented in the experimental result to some degree, being the Na-like the dominant ion, followed by the Ne-like and having small contributions from Mg-like and Al-like.

As such, the plasma of Kr does not appear to be dominated by Kr XXVII. To make a good simulated spectrum comparable to the one in the experiment, the population distribution has to be simulated at several pressure conditions and more charge state calculations should be included to improve the results.

As discussed before, there was no appreciable DR depletion, as there is no significant difference between the upwards and downwards scan. Given the calculation presented in the figure 5.8, the population of Na-like appears to be higher than the Ne-like population. The CX, due to high pressure, could be a possible explanation for this mixing of populations, the simulations presented in the last chapter show that the Ne-like population remains higher than the Na-like population, even for high pressures. Furthermore, When the Ne-like is no longer dominant, other species beyond Ne-like, Na-like, Mg-like and Al-like are expected to appear at quantities comparable to the motioned charge states, something that is not observed experimentally.

---

<sup>1</sup><https://open.adas.ac.uk/>

<sup>2</sup><http://www.atomdb.org/>



## CONCLUSIONS AND FUTURE PROSPECTS

In this thesis, the DR-LMM structure for Fe XVII was measured in two different EBIT systems and the obtained data was analysed and compared to previous measurements made in the Test Storage Ring. These measurements were made and compared with newly calculated FAC, FAC-MBPT and MCDF cross sections, as well as with atomic data available in widely used databases. The charge state distribution of the EBIT plasmas were simulated in a time-dependant manner to investigate the effects of the several EBIT experimental conditions and evaluate the presence of unwanted charge states during the probing stage or undesirable DR depletions of the Ne-like population. To make this possible, calculations of DR, RR, CI and EA were performed using FAC (and FAC-MBPT for DR-LMM) for several charge states.

The simulations allowed the estimation of the effective electron density of the experiments, which was in agreement with order of magnitude of the values found in EBIT experiments made by other groups. The role of charge exchange in the EBIT environment was also explored, highlighting the importance of the ultra-high vacuum needed for these experiments, as a high pressure ultimately translates into the loss the ions that are required in the chamber. No significant DR depletion was found for any of the experiments. The PolarX-EBIT allows the measurement of the time dynamics of the spectrum itself, so the same setup was also simulated. The comparison between the experimental time-dependent spectrum and the simulation result showed an excellent agreement all across the board, with the exception of a constant background for smaller times, serving as a validation for this type of simulations as a method to realistically study EBIT plasmas.

The experimental results were fitted to obtain values for the resonant energies and resonant strengths of the structures of the DR-LMM for Fe XVII. The experimental results were in general in good agreement with the new calculations. The FAC-MBPT was the method that showed more promising results. In this case, the MCDF energy

of some resonances in disagreement with the experimental results, leading to the apparent lack or existence of extra peaks that differed from experiments. These resulting resonant strengths were used to provide DR rate coefficients, the values that are directly used in astrophysical plasma models. The coefficient rates were provided in 3 different temperatures and were divided by the final state of the Na-like ion, as well as the total rate coefficient for the entire DR-LMM process. These values were compared to what is available in frequently used databases for astrophysical plasma diagnostics, such as OPEN-ADAS and AtomDB.

Several significant discrepancies were found between the database values and the experimental values. These discrepancies are important, as the values given by the databases may result in biased diagnostics and erroneous evaluations of the astrophysical plasma conditions. This is of special importance given the proximity of future x-ray satellite missions XRISM and Athena, that will use x-ray microcalorimeters. In addition, these values are of special importance to interpret the currently available high-resolution spectra from Chandra and XMM-Newton. Furthermore, these inconsistencies highlight the importance of laboratory measurements of atomic data, specially of HCI, for the test and development of astrophysical models.

Future work might include the analysis of the rest of the  $LMn$  DR structure, perhaps using the fitting procedure developed in this work. Preliminary results of Kr measurements and theoretical calculations and simulations were also presented. Further simulations with more atomic processes need to be performed in the future to model the spectra observed experimentally. These spectra appear to be more complex than the case of iron because there seems to be a high mixture of charge states constituting to the emissions at the same time. Several measurements were made and all resulted in similar spectra. After a good modeling is achieved, the extracted atomic data might be useful for plasma modeling in fusion reactors, namely for the evaluation of the radiative cooling at the edges of the plasma with the collisional excitation and resonant excitation. Furthermore, EBIT spectra of highly charged tungsten is also available to analyse, leaving room for the extraction of useful atomic data for another element that may play a fundamental role in future fusion reactor plasma diagnostics.



## PUBLICATIONS

The work performed during this thesis contributed to the following publications:

- C. Shah, J. R. C. López-Urrutia, M. F. Gu, T. Pfeifer, J. Marques, F. Grilo, J. P.Santos, and P. Amaro. *"Revisiting the Fe xvii Line Emission Problem: Laboratory Measurements of the  $3s-2p$  and  $3d-2p$  Line-formation Channels."* In: *The Astrophysical Journal* 881.2 (2019), p. 100. ISSN: 1538-4357. DOI:10.3847/1538-4357/ab2896.
- F. Grilo, C. Shah, S. Kühn, R. Steinbrügge, K. Fujii, J. Marques, M. F. Gu, J. P.Santos, J. R. C. López-Urrutia, P. Amaro. *Comprehensive laboratory measurements resolving the LMM dielectronic recombination satellite lines in Ne-like Fe XVII ions.* Submitted to *The Astrophysical Journal*, under review. A version of the manuscript is in attachment.



## BIBLIOGRAPHY

- [1] S. Hawking. *On the Shoulders of Giants: The Great Works of Physics and Astronomy*. 1st ed. Running Press, 2002. ISBN: 9780762416981.
- [2] P. A. Oesch et al. “A remarkably luminous galaxy at  $Z = 11.1$  measured with Hubble space telescope grism spectroscopy.” In: *The Astrophysical Journal* 819.2 (2016), p. 129. ISSN: 1538-4357. DOI: [10.3847/0004-637X/819/2/129](https://doi.org/10.3847/0004-637X/819/2/129).
- [3] L. Vegard. “Die Deutung der Nordlichterscheinungen und die Struktur der Ionosphäre.” In: *Ergebnisse der exakten naturwissenschaften*. Berlin, Heidelberg: Springer Berlin Heidelberg, pp. 229–281. DOI: [10.1007/BFb0112099](https://doi.org/10.1007/BFb0112099).
- [4] C. U. Keller. “X-rays from the Sun.” In: *Experientia* 51.7 (1995), pp. 710–720. ISSN: 0014-4754. DOI: [10.1007/BF01941268](https://doi.org/10.1007/BF01941268).
- [5] H. Friedman. “Solar ionizing radiation.” In: *Journal of Atmospheric and Terrestrial Physics* 36.12 (1974), pp. 2245–2253. ISSN: 00219169. DOI: [10.1016/0021-9169\(74\)90150-0](https://doi.org/10.1016/0021-9169(74)90150-0).
- [6] J. Bidwell, T. Khuwatsamrit, B. Askew, J. A. Ehrenberg, and S. Helmers. “Seizure reporting technologies for epilepsy treatment: A review of clinical information needs and supporting technologies.” In: *Seizure* 32.3B (2015), pp. 109–117. ISSN: 10591311. DOI: [10.1016/j.seizure.2015.09.006](https://doi.org/10.1016/j.seizure.2015.09.006).
- [7] W. Voges et al. “The Rosat All-Sky Survey Bright Source Catalog.” In: *New Horizons from Multi-Wavelength Sky Surveys*. Vol. 349. 2. Dordrecht: Springer Netherlands, 1997, pp. 433–434. DOI: [10.1007/978-94-009-1485-8\\_109](https://doi.org/10.1007/978-94-009-1485-8_109). arXiv: [9909315v2 \[arXiv:astro-ph\]](https://arxiv.org/abs/9909315v2).
- [8] F. Jansen et al. “XMM-Newton observatory.” In: *Astronomy & Astrophysics* 365.1 (2001), pp. L1–L6. ISSN: 0004-6361. DOI: [10.1051/0004-6361:20000036](https://doi.org/10.1051/0004-6361:20000036).
- [9] M. Weisskopf. “Chandra X-Ray Observatory.” In: *Van Nostrand’s Scientific Encyclopedia*. Hoboken, NJ, USA: John Wiley & Sons, Inc., 2005, pp. 1–6. DOI: [10.1002/0471743984.vse1635](https://doi.org/10.1002/0471743984.vse1635).
- [10] F. A. Harrison et al. “THE NUCLEAR SPECTROSCOPIC TELESCOPE ARRAY (NuSTAR) HIGH-ENERGY X-RAY MISSION.” In: *The Astrophysical Journal* 770.2 (2013), p. 103. DOI: [10.1088/0004-637x/770/2/103](https://doi.org/10.1088/0004-637x/770/2/103).

- [11] M. C. Weisskopf et al. “Chandra phase-resolved X-Ray spectroscopy of the Crab pulsar.” In: *The Astrophysical Journal* 743.2 (2011), p. 139. ISSN: 0004-637X. DOI: [10.1088/0004-637X/743/2/139](https://doi.org/10.1088/0004-637X/743/2/139).
- [12] G. R. Sivakoff, A. Jordán, A. M. Juett, C. L. Sarazin, and J. A. Irwin. “Deep Chandra X-ray Observations of Low Mass X-ray Binary Candidates in the Early-Type Galaxy NGC 4697.” In: *arXiv* 0806.2004 (2008), p. 31. arXiv: [0806.0626](https://arxiv.org/abs/0806.0626).
- [13] R. W. Pfeifle et al. “A Triple AGN in a Mid-infrared Selected Late-stage Galaxy Merger.” In: *The Astrophysical Journal* 883.2 (2019), p. 167. ISSN: 1538-4357. DOI: [10.3847/1538-4357/ab3a9b](https://doi.org/10.3847/1538-4357/ab3a9b). arXiv: [1908.01732](https://arxiv.org/abs/1908.01732).
- [14] O. Kargaltsev, M. Durant, G. G. Pavlov, and G. Garmire. “CHANDRA PULSAR SURVEY (ChaPS).” In: *The Astrophysical Journal Supplement Series* 201.2 (2012), p. 37. ISSN: 0067-0049. DOI: [10.1088/0067-0049/201/2/37](https://doi.org/10.1088/0067-0049/201/2/37).
- [15] XRISM Science Team. “Science with the X-ray Imaging and Spectroscopy Mission (XRISM).” In: (2020). arXiv: [2003.04962](https://arxiv.org/abs/2003.04962).
- [16] X. Barcons et al. “Athena: ESA’s X-ray observatory for the late 2020s.” In: *Astronomische Nachrichten* 338.2-3 (2017), pp. 153–158. ISSN: 00046337. DOI: [10.1002/asna.201713323](https://doi.org/10.1002/asna.201713323).
- [17] *Chandra :: Photo Album :: Crab Nebula :: 2020*. URL: <https://chandra.harvard.edu/photo/2018/crab/>.
- [18] T. R. Kallman and P. Palmeri. “Atomic data for x-ray astrophysics.” In: *Reviews of Modern Physics* 79.1 (2007), pp. 79–133. ISSN: 0034-6861. DOI: [10.1103/RevModPhys.79.79](https://doi.org/10.1103/RevModPhys.79.79). arXiv: [0610423](https://arxiv.org/abs/0610423) [astro-ph].
- [19] P. Beiersdorfer. “Laboratory X-Ray Astrophysics.” In: *Annual Review of Astronomy and Astrophysics* 41.1 (2003), pp. 343–390. ISSN: 0066-4146. DOI: [10.1146/annurev.astro.41.011802.094825](https://doi.org/10.1146/annurev.astro.41.011802.094825).
- [20] M. Kikuchi. “A Review of Fusion and Tokamak Research Towards Steady-State Operation: A JAEA Contribution.” In: *Energies* 3.11 (2010), pp. 1741–1789. ISSN: 1996-1073. DOI: [10.3390/en3111741](https://doi.org/10.3390/en3111741).
- [21] M. J. May et al. “The American Astronomical Society, find out more The Institute of Physics, find out more Accurate Wavelength Measurements and Modeling of Fe XV to Fe XIX Spectra Recorded in High-Density Plasmas between 13.5 and 17 Å.” In: *The Astrophysical Journal Supplement Series* 158.2 (2005), pp. 230–241. ISSN: 0067-0049. DOI: [10.1086/429541](https://doi.org/10.1086/429541).
- [22] J. D. Gillaspy et al. “Overview of the electron beam ion trap program at NIST.” In: *Physica Scripta* T59.T59 (1995), pp. 392–395. ISSN: 0031-8949. DOI: [10.1088/0031-8949/1995/T59/053](https://doi.org/10.1088/0031-8949/1995/T59/053).

- [23] R. E. Marrs, S. R. Elliott, and D. A. Knapp. “Production and Trapping of Hydrogenlike and Bare Uranium Ions in an Electron Beam Ion Trap.” In: *Physical Review Letters* 72.26 (1994), pp. 4082–4085. ISSN: 0031-9007. DOI: [10.1103/PhysRevLett.72.4082](https://doi.org/10.1103/PhysRevLett.72.4082).
- [24] J. N. Tan, E. Silver, J. Pomeroy, J. M. Laming, and J. Gillaspy. “An Electron Beam Ion Trap (EBIT) Plus a Microcalorimeter: A Good Combination for Laboratory Astrophysics.” In: *Physica Scripta* T119 (2005), pp. 30–34. ISSN: 0031-8949. DOI: [10.1088/0031-8949/2005/T119/005](https://doi.org/10.1088/0031-8949/2005/T119/005).
- [25] S. Kühn et al. “High Resolution Photoexcitation Measurements Exacerbate the Long-Standing Fe XVII Oscillator Strength Problem.” In: *Physical Review Letters* 124.22 (2020), p. 225001. ISSN: 0031-9007. DOI: [10.1103/PhysRevLett.124.225001](https://doi.org/10.1103/PhysRevLett.124.225001). arXiv: [1911.09707 \[physics.atom-ph\]](https://arxiv.org/abs/1911.09707).
- [26] R. Mewe, A. J. J. Raassen, J. J. Drake, J. S. Kaastra, R. L. J. van der Meer, and D. Porquet. “CHANDRA-LETGS X-ray observations of Capella.” In: *Astronomy & Astrophysics* 368.3 (2001), pp. 888–900. ISSN: 0004-6361. DOI: [10.1051/0004-6361:20010026](https://doi.org/10.1051/0004-6361:20010026).
- [27] A. Müller. “Electron–ion collisions: Fundamental processes in the focus of applied research.” In: *Advances in Atomic, Molecular and Optical Physics*. Vol. 55. 07. 2008, pp. 293–417. ISBN: 9780123737106. DOI: [10.1016/S1049-250X\(07\)55006-8](https://doi.org/10.1016/S1049-250X(07)55006-8).
- [28] J. D. Gillaspy et al. “Fe XVII X-ray line ratios for accurate astrophysical plasma diagnostics.” In: *The Astrophysical Journal* 728.2 (2011), p. 132. ISSN: 0004-637X. DOI: [10.1088/0004-637X/728/2/132](https://doi.org/10.1088/0004-637X/728/2/132).
- [29] F. B. Paerels and S. M. Kahn. “High-Resolution X-Ray Spectroscopy with Chandra and XMM-Newton.” In: *Annual Review of Astronomy and Astrophysics* 41.1 (2003), pp. 291–342. ISSN: 0066-4146. DOI: [10.1146/annurev.astro.41.071601.165952](https://doi.org/10.1146/annurev.astro.41.071601.165952).
- [30] C. Shah, P. Amaro, R. Steinbrügge, S. Bernitt, J. R. C. López-Urrutia, and S. Tashenov. “Polarization of K-shell Dielectronic Recombination Satellite Lines of Fe xix–xxv and Its Application for Diagnostics of Anisotropies of Hot Plasmas.” In: *The Astrophysical Journal Supplement Series* 234.2 (2018), p. 27. ISSN: 1538-4365. DOI: [10.3847/1538-4365/aaa4c0](https://doi.org/10.3847/1538-4365/aaa4c0).
- [31] M. Nobukawa, H. Uchiyama, K. K. Nobukawa, S. Yamauchi, and K. Koyama. “Origin of the galactic diffuse X-ray emission: iron K-shell line diagnostics.” In: *The Astrophysical Journal* 833.2 (2016), p. 268. ISSN: 1538-4357. DOI: [10.3847/1538-4357/833/2/268](https://doi.org/10.3847/1538-4357/833/2/268).

- [32] A Graf, P Beiersdorfer, G. V. Brown, and M. F. Gu. “Measurement and modeling of Na-like Fe XVI inner-shell satellites between 14.5 Å and 18 Å.” In: *The Astrophysical Journal* 695.2 (2009), pp. 818–824. ISSN: 0004-637X. DOI: [10.1088/0004-637X/695/2/818](https://doi.org/10.1088/0004-637X/695/2/818).
- [33] J. M. Laming et al. “Emission-Line Intensity Ratios in Fe XVII Observed with a Microcalorimeter on an Electron Beam Ion Trap.” In: *The Astrophysical Journal* 545.2 (2000), pp. L161–L164. ISSN: 0004637X. DOI: [10.1086/317876](https://doi.org/10.1086/317876).
- [34] P Beiersdorfer et al. “Laboratory Measurements of the Relative Intensity of the 3s → 2p and 3d → 2p Transitions in Fe XVII.” In: *The Astrophysical Journal* 576.2 (2002), pp. L169–L172. ISSN: 0004637X. DOI: [10.1086/343785](https://doi.org/10.1086/343785).
- [35] P Beiersdorfer, M Bitter, S. von Goeler, and K. W. Hill. “Laboratory Measurements of the Fe XVII 2p-3s and 2p-3d Transitions and Comparison with Solar and Astrophysical Observations.” In: *The Astrophysical Journal* 610.1 (2004), pp. 616–623. ISSN: 0004-637X. DOI: [10.1086/421512](https://doi.org/10.1086/421512).
- [36] G. V. Brown et al. “Energy-Dependent Excitation Cross Section Measurements of the Diagnostic Lines of Fe XVII.” In: *Physical Review Letters* 96.25 (2006), p. 253201. ISSN: 0031-9007. DOI: [10.1103/PhysRevLett.96.253201](https://doi.org/10.1103/PhysRevLett.96.253201).
- [37] C. Shah et al. “Revisiting the Fe xvii Line Emission Problem: Laboratory Measurements of the 3 s – 2 p and 3 d – 2 p Line-formation Channels.” In: *The Astrophysical Journal* 881.2 (2019), p. 100. ISSN: 1538-4357. DOI: [10.3847/1538-4357/ab2896](https://doi.org/10.3847/1538-4357/ab2896).
- [38] G. V. Brown, P. Beiersdorfer, D. A. Liedahl, K. Widmann, S. M. Kahn, and E. J. Clothiaux. “Laboratory Measurements and Identification of the Fe XVIII – XXIV L-Shell X-Ray Line Emission.” In: *The Astrophysical Journal Supplement Series* 140.2 (2002), pp. 589–607. ISSN: 0067-0049. DOI: [10.1086/339374](https://doi.org/10.1086/339374).
- [39] H Chen et al. “Electron Impact Excitation Cross Section Measurement from n= 3 to n= 2 Line Emission in Fe17+ to Fe23+.” In: *The Astrophysical Journal* 646.1 (2006), pp. 653–665. DOI: [10.1086/504708](https://doi.org/10.1086/504708).
- [40] H Chen et al. “Excitation Cross Section Measurement for n = 3 to n = 2 Line Emission in Fe 20+ to Fe 23+.” In: *The Astrophysical Journal* 618.2 (2005), pp. 1086–1094. ISSN: 0004-637X. DOI: [10.1086/426135](https://doi.org/10.1086/426135).
- [41] M. F. Gu, D. W. Savin, and P Beiersdorfer. “Effects of electron spiralling on the anisotropy and polarization of photon emission from an electron beam ion trap.” In: *Journal of Physics B: Atomic, Molecular and Optical Physics* 32.22 (1999), pp. 5371–5378. ISSN: 0953-4075. DOI: [10.1088/0953-4075/32/22/314](https://doi.org/10.1088/0953-4075/32/22/314).
- [42] H Chen et al. “Measurement of Emission Cross Sections for n = 3 → 2 Lines in Li-like Fe23+.” In: *The Astrophysical Journal* 567.2 (2002), pp. L169–L172. DOI: [10.1086/340007](https://doi.org/10.1086/340007).



- [43] M. F. Gu et al. “Laboratory Measurements of Iron L-Shell Emission: 3→2 Transitions of Fe XXI – XXIV between 10.5 and 12.5 Å.” In: *The Astrophysical Journal* 563.1 (2001), pp. 462–471. ISSN: 0004-637X. DOI: [10.1086/323683](https://doi.org/10.1086/323683).
- [44] T. Nagayama et al. “Systematic Study of L-Shell Opacity at Stellar Interior Temperatures.” In: *Physical Review Letters* 122.23 (2019), p. 235001. ISSN: 0031-9007. DOI: [10.1103/PhysRevLett.122.235001](https://doi.org/10.1103/PhysRevLett.122.235001).
- [45] H. Netzer. “The Iron Unresolved Transition Array in Active Galactic Nuclei.” In: *The Astrophysical Journal* 604.2 (2004), pp. 551–555. ISSN: 0004-637X. DOI: [10.1086/382038](https://doi.org/10.1086/382038).
- [46] J. de Plaa et al. “Estimating turbulent velocities in the elliptical galaxies NGC 5044 and NGC 5813.” In: *Astronomy & Astrophysics* 539 (2012), A34. ISSN: 0004-6361. DOI: [10.1051/0004-6361/201118404](https://doi.org/10.1051/0004-6361/201118404).
- [47] D. Bernhardt et al. “Absolute rate coefficients for photorecombination and electron-impact ionization of magnesiumlike iron ions from measurements at a heavy-ion storage ring.” In: *Physical Review A* 90.1 (2014), p. 012702. ISSN: 1050-2947. DOI: [10.1103/PhysRevA.90.012702](https://doi.org/10.1103/PhysRevA.90.012702).
- [48] G. V. Brown, P. Beiersdorfer, D. A. Liedahl, K. Widmann, and S. M. Kahn. “Laboratory Measurements and Modeling of the Fe  $\text{XVII}$  X-Ray Spectrum.” In: *The Astrophysical Journal* 502.2 (1998), pp. 1015–1026. ISSN: 0004-637X. DOI: [10.1086/305941](https://doi.org/10.1086/305941).
- [49] J. M. Laming et al. “Emission-Line Intensity Ratios in Fe XVII Observed with a Microcalorimeter on an Electron Beam Ion Trap.” In: *The Astrophysical Journal* 545.2 (2000), pp. L161–L164. ISSN: 0004637X. DOI: [10.1086/317876](https://doi.org/10.1086/317876).
- [50] S. Bernitt et al. “An unexpectedly low oscillator strength as the origin of the Fe xvii emission problem.” In: *Nature* 492.7428 (2012), pp. 225–228. ISSN: 0028-0836. DOI: [10.1038/nature11627](https://doi.org/10.1038/nature11627).
- [51] J. Dudík, E. Dzifčáková, G. Del Zanna, H. E. Mason, L. L. Golub, A. R. Winebarger, and S. L. Savage. “Signatures of the non-Maxwellian  $\kappa$ -distributions in optically thin line spectra.” In: *Astronomy & Astrophysics* 626 (2019), A88. ISSN: 0004-6361. DOI: [10.1051/0004-6361/201935285](https://doi.org/10.1051/0004-6361/201935285).
- [52] J. Clementson and P. Beiersdorfer. “Investigation of dielectronic recombination satellite emission to Fe XVIII for temperature measurements of stellar atmospheres.” In: *The Astrophysical Journal* 763.1 (2013), p. 54. ISSN: 0004-637X. DOI: [10.1088/0004-637X/763/1/54](https://doi.org/10.1088/0004-637X/763/1/54).
- [53] P. Beiersdorfer, N. Hell, and J. K. Lepson. “Temperature Measurements Using the Dielectronic Satellite Lines of Fe xvii.” In: *The Astrophysical Journal* 864.1 (2018), p. 24. ISSN: 1538-4357. DOI: [10.3847/1538-4357/aad27f](https://doi.org/10.3847/1538-4357/aad27f).

- [54] L. Gu et al. “X-ray spectra of the Fe-L complex.” In: *Astronomy & Astrophysics* 641 (2020), A93. ISSN: 0004-6361. DOI: [10.1051/0004-6361/202037948](https://doi.org/10.1051/0004-6361/202037948). arXiv: [2007.03843](https://arxiv.org/abs/2007.03843).
- [55] A. R. Foster, L. Ji, R. K. Smith, and N. S. Brickhouse. “Updated atomic data and calculations for X-ray spectroscopy.” In: *The Astrophysical Journal* 756.2 (2012), p. 128. ISSN: 0004-637X. DOI: [10.1088/0004-637X/756/2/128](https://doi.org/10.1088/0004-637X/756/2/128).
- [56] J. Kaastra, R Mewe, and H Nieuwenhuijzen. “SPEX: a new code for spectral analysis of X & UV spectra.” In: *UV and X-ray Spectroscopy of Astrophysical and Laboratory Plasmas*. 1996, pp. 411–414.
- [57] K. P. Dere, G. D. Zanna, P. R. Young, E. Landi, and R. S. Sutherland. “CHI-ANTI—An Atomic Database for Emission Lines. XV. Version 9, Improvements for the X-Ray Satellite Lines.” In: *The Astrophysical Journal Supplement Series* 241.2 (2019), p. 22. ISSN: 1538-4365. DOI: [10.3847/1538-4365/ab05cf](https://doi.org/10.3847/1538-4365/ab05cf).
- [58] P. Beiersdorfer, M. P. Bode, Y. Ishikawa, and F. Diaz. “L-shell dielectronic satellite transitions of Fe XVII.” In: *The Astrophysical Journal* 793.2 (2014), p. 99. ISSN: 1538-4357. DOI: [10.1088/0004-637X/793/2/99](https://doi.org/10.1088/0004-637X/793/2/99).
- [59] *Machine*. 2020. URL: <https://www.iter.org/mach>.
- [60] M. Shimada et al. “Chapter 1: Overview and summary.” In: *Nuclear Fusion* 47.6 (2007), S1–S17. ISSN: 0029-5515. DOI: [10.1088/0029-5515/47/6/S01](https://doi.org/10.1088/0029-5515/47/6/S01).
- [61] P. Beiersdorfer, J. Clementson, and U. Safronova. “Tungsten Data for Current and Future Uses in Fusion and Plasma Science.” In: *Atoms* 3.2 (2015), pp. 260–272. ISSN: 2218-2004. DOI: [10.3390/atoms3020260](https://doi.org/10.3390/atoms3020260).
- [62] S. A. Cohen, K. A. Werley, D. E. Post, B. J. Braams, J. L. Perkins, and D. Pearlstein. “Two-dimensional fluid simulations of the ITER SOL plasma.” In: *Journal of Nuclear Materials* 176-177.C (1990), pp. 909–915. ISSN: 00223115. DOI: [10.1016/0022-3115\(90\)90167-L](https://doi.org/10.1016/0022-3115(90)90167-L).
- [63] J. Cummings, S. A. Cohen, R. Hulse, D. E. Post, M. H. Redi, and J. Perkins. “Power radiated from ITER by impurities.” In: *Journal of Nuclear Materials* 176-177.C (1990), pp. 916–921. ISSN: 00223115. DOI: [10.1016/0022-3115\(90\)90168-M](https://doi.org/10.1016/0022-3115(90)90168-M).
- [64] M. Bitter et al. “Spectra of heliumlike krypton from Tokamak Fusion Test Reactor plasmas.” In: *Physical Review Letters* 71.7 (1993), pp. 1007–1010. ISSN: 0031-9007. DOI: [10.1103/PhysRevLett.71.1007](https://doi.org/10.1103/PhysRevLett.71.1007).
- [65] K. Widmann et al. “Studies of He-like krypton for use in determining electron and ion temperatures in very-high-temperature plasmas.” In: *Review of Scientific Instruments* 66.1 (1995), pp. 761–763. ISSN: 0034-6748. DOI: [10.1063/1.1146281](https://doi.org/10.1063/1.1146281).

- [66] R. Radtke, C. Biedermann, T. Fuchs, G. Fußmann, and P. Beiersdorfer. “Measurement of the radiative cooling rates for high-ionization species of krypton using an electron beam ion trap.” In: *Physical Review E* 61.2 (2000), pp. 1966–1974. ISSN: 1063-651X. DOI: [10.1103/PhysRevE.61.1966](https://doi.org/10.1103/PhysRevE.61.1966).
- [67] M. F. Gu. “The flexible atomic code.” In: *Canadian Journal of Physics* 86.5 (2008), pp. 675–689. ISSN: 0008-4204. DOI: [10.1139/p07-197](https://doi.org/10.1139/p07-197).
- [68] W. Greiner. *Relativistic Quantum Mechanics. Wave Equations*. 3rd ed. Heidelberg: Springer-Verlag Berlin Heidelberg, 2000, p. 424. ISBN: 978-3-662-04275-5. DOI: [10.1007/978-3-662-04275-5](https://doi.org/10.1007/978-3-662-04275-5).
- [69] W. R. Johnson. *Atomic Structure Theory*. Ed. by Springer-Verlag Berlin Heidelberg. 1st ed. Berlin, Heidelberg: Springer Berlin Heidelberg, 2007, p. 312. ISBN: 978-3-540-68010-9. DOI: [10.1007/978-3-540-68013-0](https://doi.org/10.1007/978-3-540-68013-0).
- [70] E. Schrödinger. “Quantisierung als Eigenwertproblem.” In: *Annalen der Physik* 384.6 (1926), pp. 489–527. ISSN: 00033804. DOI: [10.1002/andp.19263840602](https://doi.org/10.1002/andp.19263840602).
- [71] P. A. M. Dirac. “The quantum theory of the electron.” In: *Proceedings of the Royal Society of London. Series A, Containing Papers of a Mathematical and Physical Character* 117.778 (1928), pp. 610–624. ISSN: 0950-1207. DOI: [10.1098/rspa.1928.0023](https://doi.org/10.1098/rspa.1928.0023).
- [72] P. Amaro, A. Surzhykov, F. Parente, P. Indelicato, and J. P. Santos. “Calculation of two-photon decay rates of hydrogen-like ions by using B-polynomials.” In: *Journal of Physics A: Mathematical and Theoretical* 44.24 (2011), p. 245302. ISSN: 1751-8113. DOI: [10.1088/1751-8113/44/24/245302](https://doi.org/10.1088/1751-8113/44/24/245302).
- [73] W. R. Johnson, S. A. Blundell, and J. Sapirstein. “Finite basis sets for the Dirac equation constructed from B splines.” In: *Physical Review A* 37.2 (1988), pp. 307–315. ISSN: 0556-2791. DOI: [10.1103/PhysRevA.37.307](https://doi.org/10.1103/PhysRevA.37.307).
- [74] M. Cohen and R. P. Mceachran. “Atomic Hartree–Fock Theory.” In: ed. by D. R. Bates and B. B. Stewart. Vol. 16. *Advances in Atomic and Molecular Physics*. Academic Press, 1980, pp. 1–54. DOI: [https://doi.org/10.1016/S0065-2199\(08\)60005-6](https://doi.org/10.1016/S0065-2199(08)60005-6).
- [75] A. Bar-Shalom, M. Klapisch, and J. Oreg. “Electron collision excitations in complex spectra of ionized heavy atoms.” In: *Phys. Rev. A* 38 (4 1988), pp. 1773–1784. DOI: [10.1103/PhysRevA.38.1773](https://doi.org/10.1103/PhysRevA.38.1773).
- [76] W. Lotz. “An empirical formula for the electron-impact ionization cross-section.” In: *Zeitschrift für Physik* 206.2 (1967), pp. 205–211. ISSN: 1434-6001. DOI: [10.1007/BF01325928](https://doi.org/10.1007/BF01325928).
- [77] M. Hahn et al. “Storage ring cross section measurements for electron impact ionization of Fe 11+ forming Fe 12+ and Fe 13+.” In: *The Astrophysical Journal* 729.1 (2011), p. 76. ISSN: 0004-637X. DOI: [10.1088/0004-637X/729/1/76](https://doi.org/10.1088/0004-637X/729/1/76).










- [78] M. Hahn et al. “Storage ring cross section measurements for electron impact single and double ionization of Fe 13 + and single ionization of Fe 16 + and Fe 17 +.” In: *The Astrophysical Journal* 767.1 (2013), p. 47. ISSN: 0004-637X. DOI: [10.1088/0004-637X/767/1/47](https://doi.org/10.1088/0004-637X/767/1/47).
- [79] G. J. Tallents. *An Introduction to the Atomic and Radiation Physics of Plasmas*. Cambridge University Press, 2018. DOI: [10.1017/9781108303538](https://doi.org/10.1017/9781108303538).
- [80] Y. Hahn. “Electron - ion recombination processes - an overview.” In: *Reports on Progress in Physics* 60.7 (1997), pp. 691–759. ISSN: 0034-4885. DOI: [10.1088/0034-4885/60/7/001](https://doi.org/10.1088/0034-4885/60/7/001).
- [81] G. J. Ferland, K. T. Korista, D. A. Verner, J. W. Ferguson, J. B. Kingdon, and E. M. Verner. “CLOUDY 90: Numerical Simulation of Plasmas and Their Spectra.” In: *Publications of the Astronomical Society of the Pacific* 110.749 (1998), pp. 761–778. DOI: [10.1086/316190](https://doi.org/10.1086/316190).
- [82] T. Kallman and M. Bautista. “Photoionization and High-Density Gas.” In: *The Astrophysical Journal Supplement Series* 133.1 (2001), pp. 221–253. DOI: [10.1086/319184](https://doi.org/10.1086/319184).
- [83] Dere, K. P., Landi, E., Mason, H. E., Monsignori Fossi, B. C., and Young, P. R. “CHIANTI - an atomic database for emission lines\* - I. Wavelengths greater than 50 Å.” In: *Astron. Astrophys. Suppl. Ser.* 125.1 (1997), pp. 149–173. DOI: [10.1051/aas:1997368](https://doi.org/10.1051/aas:1997368).
- [84] M. F. Gu. “Dielectronic Recombination Rate Coefficients for H-like through Ne-like Isosequences of Mg, Si, S, Ar, Ca, Fe, and Ni.” In: *The Astrophysical Journal* 590.2 (2003), pp. 1131–1140. ISSN: 0004-637X. DOI: [10.1086/375135](https://doi.org/10.1086/375135).
- [85] R. K. Janev, D. S. Belić, and B. H. Bransden. “Total and partial cross sections for electron capture in collisions of hydrogen atoms with fully stripped ions.” In: *Physical Review A* 28.3 (1983), pp. 1293–1302. ISSN: 0556-2791. DOI: [10.1103/PhysRevA.28.1293](https://doi.org/10.1103/PhysRevA.28.1293).
- [86] P. Beiersdorfer et al. “Measurement and interpretation of the polarization of the x-ray line emission of heliumlike Fe XXV excited by an electron beam.” In: *Physical Review A* 53.6 (1996), pp. 3974–3981. ISSN: 1050-2947. DOI: [10.1103/PhysRevA.53.3974](https://doi.org/10.1103/PhysRevA.53.3974).
- [87] V. V. Balashov, A. N. G. Grzhimailo, and N. M. Kabachnik. *Polarization and Correlation Phenomena in Atomic Collisions: A Practical Theory Course*. 2000. ISBN: 9781475732283.
- [88] C. Shah. “Measuring and modeling of anisotropic and polarized x-ray emission following resonant recombination into highly charged ions.” PhD. Combined Faculties of the Natural Sciences and Mathematics of the Ruperto-Carola-University of Heidelberg, Germany, 2016. DOI: [10.11588/heidok.00019922](https://doi.org/10.11588/heidok.00019922).

- [89] O Gorceix, P Indelicato, and J. P. Desclaux. “Multiconfiguration Dirac-Fock studies of two-electron ions. I. Electron-electron interaction.” In: *Journal of Physics B: Atomic and Molecular Physics* 20.4 (1987), pp. 639–649. ISSN: 0022-3700. DOI: [10.1088/0022-3700/20/4/006](https://doi.org/10.1088/0022-3700/20/4/006).
- [90] P Indelicato, O Gorceix, and J. P. Desclaux. “Multiconfigurational Dirac-Fock studies of two-electron ions. II. Radiative corrections and comparison with experiment.” In: *Journal of Physics B: Atomic and Molecular Physics* 20.4 (1987), pp. 651–663. ISSN: 0022-3700. DOI: [10.1088/0022-3700/20/4/007](https://doi.org/10.1088/0022-3700/20/4/007).
- [91] K. Dyall, I. Grant, C. Johnson, F. Parpia, and E. Plummer. “GRASP: A general-purpose relativistic atomic structure program.” In: *Computer Physics Communications* 55.3 (1989), pp. 425–456. ISSN: 00104655. DOI: [10.1016/0010-4655\(89\)90136-7](https://doi.org/10.1016/0010-4655(89)90136-7).
- [92] P Jönsson, G Gaigalas, J Bieroń, C. F. Fischer, and I. Grant. “New version: Grasp2K relativistic atomic structure package.” In: *Computer Physics Communications* 184.9 (2013), pp. 2197–2203. ISSN: 00104655. DOI: [10.1016/j.cpc.2013.02.016](https://doi.org/10.1016/j.cpc.2013.02.016).
- [93] C Froese Fischer, G Gaigalas, P Jönsson, and J Bieroń. “GRASP2018—A Fortran 95 version of the General Relativistic Atomic Structure Package.” In: *Computer Physics Communications* 237 (2019), pp. 184–187. ISSN: 00104655. DOI: [10.1016/j.cpc.2018.10.032](https://doi.org/10.1016/j.cpc.2018.10.032).
- [94] M Klapisch, J. L. Schwob, B. S. Fraenkel, and J Oreg. “The 1s-3p  $K\beta$ -like x-ray spectrum of highly ionized iron.” In: *Journal of the Optical Society of America* 67.2 (1977), p. 148. ISSN: 0030-3941. DOI: [10.1364/JOSA.67.000148](https://doi.org/10.1364/JOSA.67.000148).
- [95] A Bar-Shalom, M Klapisch, and J Oreg. “HULLAC, an integrated computer package for atomic processes in plasmas.” In: *Journal of Quantitative Spectroscopy and Radiative Transfer* 71.2-6 (2001), pp. 169–188. ISSN: 00224073. DOI: [10.1016/S0022-4073\(01\)00066-8](https://doi.org/10.1016/S0022-4073(01)00066-8).
- [96] M. S. Safronova, W. R. Johnson, and U. I. Safronova. “Relativistic many-body calculations of the energies of  $n = 2$  states for the berylliumlike isoelectronic sequence.” In: *Physical Review A* 53.6 (1996), pp. 4036–4053. ISSN: 1050-2947. DOI: [10.1103/PhysRevA.53.4036](https://doi.org/10.1103/PhysRevA.53.4036).
- [97] D Gregory, G. H. Dunn, R. A. Phaneuf, and D. H. Crandall. “Absolute cross sections for 2s2p excitation of  $N^{4+}$  by electron impact.” In: *Physical Review A* 20.2 (1979), pp. 410–420. ISSN: 0556-2791. DOI: [10.1103/PhysRevA.20.410](https://doi.org/10.1103/PhysRevA.20.410).
- [98] M. A. Levine, R. E. Marrs, J. R. Henderson, D. A. Knapp, and M. B. Schneider. “The Electron Beam Ion Trap: A New Instrument for Atomic Physics Measurements.” In: *Physica Scripta* T22 (1988), pp. 157–163. ISSN: 0031-8949. DOI: [10.1088/0031-8949/1988/T22/024](https://doi.org/10.1088/0031-8949/1988/T22/024).

- [99] E. Donets. “Electron beam ion sources and associated physics at JINR.” In: *Nuclear Instruments and Methods in Physics Research Section B: Beam Interactions with Materials and Atoms* 9.4 (1985), pp. 522–525. ISSN: 0168583X. DOI: [10.1016/0168-583X\(85\)90359-3](https://doi.org/10.1016/0168-583X(85)90359-3).
- [100] G. Herrmann. “Optical Theory of Thermal Velocity Effects in Cylindrical Electron Beams.” In: *Journal of Applied Physics* 29.2 (1958), pp. 127–136. ISSN: 0021-8979. DOI: [10.1063/1.1723053](https://doi.org/10.1063/1.1723053).
- [101] L. Brillouin. “A Theorem of Larmor and Its Importance for Electrons in Magnetic Fields.” In: *Physical Review* 67.7-8 (1945), pp. 260–266. ISSN: 0031-899X. DOI: [10.1103/PhysRev.67.260](https://doi.org/10.1103/PhysRev.67.260).
- [102] S. W. Epp et al. “X-ray laser spectroscopy of highly charged ions at FLASH.” In: *Journal of Physics B: Atomic, Molecular and Optical Physics* 43.19 (2010), p. 194008. ISSN: 0953-4075. DOI: [10.1088/0953-4075/43/19/194008](https://doi.org/10.1088/0953-4075/43/19/194008).
- [103] P. Micke et al. “The Heidelberg compact electron beam ion traps.” In: *Review of Scientific Instruments* 89.6 (2018), p. 063109. ISSN: 0034-6748. DOI: [10.1063/1.5026961](https://doi.org/10.1063/1.5026961).
- [104] J. Linkemann et al. “Electron-Impact Ionization of Fe 15+ Ions: An Ion Storage Ring Cross Section Measurement.” In: *Physical Review Letters* 74.21 (1995), pp. 4173–4176. ISSN: 0031-9007. DOI: [10.1103/PhysRevLett.74.4173](https://doi.org/10.1103/PhysRevLett.74.4173).
- [105] E. W. Schmidt et al. “Experimental rate coefficient for dielectronic recombination of neonlike iron forming sodiumlike iron.” In: *Journal of Physics: Conference Series* 163 (2009), p. 012028. ISSN: 1742-6596. DOI: [10.1088/1742-6596/163/1/012028](https://doi.org/10.1088/1742-6596/163/1/012028).
- [106] J. Nilsen. “Dielectronic satellite spectra for neon-like ions.” In: *Atomic Data and Nuclear Data Tables* 41.1 (1989), pp. 131–177. ISSN: 0092640X. DOI: [10.1016/0092-640X\(89\)90028-4](https://doi.org/10.1016/0092-640X(89)90028-4).
- [107] NIST: Atomic Spectra Database - Ionization Energies Form. URL: <https://physics.nist.gov/PhysRefData/ASD/ionEnergy.html> (visited on 11/02/2020).
- [108] T. P. Arthanayaka, P. Beiersdorfer, G. V. Brown, M. Hahn, N. Hell, T. E. Lockard, and D. W. Savin. “Measurements of the effective electron density in an electron beam ion trap using extreme ultraviolet spectra and optical imaging.” In: *Review of Scientific Instruments* 89.10 (2018), 10E119. ISSN: 0034-6748. DOI: [10.1063/1.5036758](https://doi.org/10.1063/1.5036758).
- [109] G. Y. Liang et al. “Experimental investigations of ion charge distributions, effective electron densities, and electron-ion cloud overlap in electron beam ion trap plasma using extreme-ultraviolet spectroscopy.” In: *The Astrophysical Journal* 702.2 (2009), pp. 838–850. ISSN: 0004-637X. DOI: [10.1088/0004-637X/702/2/838](https://doi.org/10.1088/0004-637X/702/2/838).

- [110] H. Chen, P. Beiersdorfer, D. Robbins, A. J. Smith, and M. F. Gu. “Polarization measurement of Iron L-shell lines on EBIT-1.” In: (2004).
- [111] G. Xiong et al. “KLL dielectronic-recombination measurement for Li-like to O-like gold.” In: *Physical Review A* 88.4 (2013), p. 042704. ISSN: 1050-2947. DOI: [10.1103/PhysRevA.88.042704](https://doi.org/10.1103/PhysRevA.88.042704).
- [112] K Yao et al. “KLL dielectronic recombination resonant strengths of He-like up to O-like xenon ions.” In: *Physical Review A* 81.2 (2010), p. 022714. ISSN: 1050-2947. DOI: [10.1103/PhysRevA.81.022714](https://doi.org/10.1103/PhysRevA.81.022714).
- [113] O. Zatsarinny, T. W. Gorczyca, K. Korista, N. R. Badnell, and D. W. Savin. “Dielectronic recombination data for dynamic finite-density plasmas.” In: *Astronomy & Astrophysics* 426.2 (2004), pp. 699–705. ISSN: 0004-6361. DOI: [10.1051/0004-6361:20040463](https://doi.org/10.1051/0004-6361:20040463).

## Comprehensive laboratory measurements resolving the LMM dielectronic recombination satellite lines in Ne-like Fe XVII ions

FILIPE GRILO <sup>1</sup>, CHINTAN SHAH <sup>2,3</sup>, STEFFEN KÜHN <sup>2,4</sup>, RENÉ STEINBRÜGGE <sup>5</sup>, KEISUKE FUJII <sup>6</sup>, JOSÉ MARQUES <sup>7,1</sup>,  
MING FENG GU <sup>8</sup>, JOSÉ PAULO SANTOS <sup>1</sup>, JOSÉ R. CRESPO LÓPEZ-URRUTIA <sup>2</sup> AND PEDRO AMARO <sup>1</sup>

<sup>1</sup>Laboratory of Instrumentation, Biomedical Engineering and Radiation Physics (LIBPhys-UNL), Department of Physics, NOVA School of Science and Technology, NOVA University Lisbon, 2829-516 Caparica, Portugal

<sup>2</sup>Max-Planck-Institut für Kernphysik, Saupfercheckweg 1, 69117 Heidelberg, Germany

<sup>3</sup>NASA Goddard Space Flight Center, 8800 Greenbelt Rd, Greenbelt, MD 20771, USA

<sup>4</sup>Heidelberg Graduate School of Fundamental Physics, Ruprecht-Karls-Universität Heidelberg, Im Neuenheimer Feld 226, 69120 Heidelberg, Germany

<sup>5</sup>Deutsches Elektronen-Synchrotron DESY, Notkestraße 85, 22607 Hamburg, Germany

<sup>6</sup>Department of Mechanical Engineering and Science, Graduate School of Engineering, Kyoto University, Kyoto 615-8540, Japan

<sup>7</sup>University of Lisboa, Faculty of Sciences, BioISI—Biosystems & Integrative Sciences Institute, Lisboa, Portugal

<sup>8</sup>Space Science Laboratory, University of California, Berkeley, CA 94720, USA

(Received August 8, 2020)

Submitted to ApJ

### ABSTRACT

We investigate experimentally and theoretically dielectronic recombination (DR) populating doubly excited configurations  $3l3l'$  (LMM) in Fe XVII, the strongest channel for soft x-ray line formation in this ubiquitous species. We used two different electron beam ion traps and two complementary measurement schemes for preparing the Fe XVII samples and evaluating their purity, observing negligible contamination effects. This allowed us to diagnose the electron density in both EBITs. We compare our experimental resonance energies and strengths with a previous independent work at a storage ring as well as configuration-interaction, multiconfiguration Dirac-Fock calculations and many-body perturbation theory. The latter showed outstanding predictive power in comparison with the combined independent experimental results. From these we also infer DR rate coefficients, unveiling significant discrepancies from those compiled in the OPEN-ADAS and AtomDB databases.

*Keywords:* atomic data — atomic processes — line: formation — methods: laboratory: atomic — plasmas — X-rays: general

### 1. INTRODUCTION

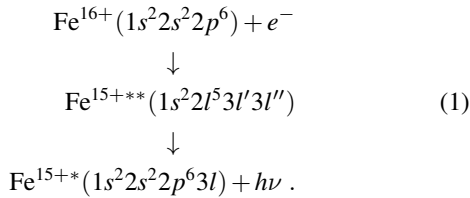
Iron, the heaviest among the abundant chemical elements, has strong L-shell transitions that dominate the X-ray spectra of astrophysical hot (MK temperature regime) plasmas in the range of 15-18 Å. Due to its closed-shell configuration with a high ionization potential of 1260 eV, Fe XVII (Ne-like Fe<sup>+16</sup>) is a very stable and abundant species under those conditions. Collisional excitation of the  $3d \rightarrow 2p$  and  $3s \rightarrow 2p$  transitions in this ion generates the strongest observed lines in the X-ray spectra (for an overview, see (Brown 2008) and references therein). These, together with less intense L-shell transitions from Fe in other charge states, e. g., Fe XVI (Na-

like Fe<sup>+15</sup>), provide means for diagnosing the physical conditions of those plasmas (Paerels & Kahn 2003). Therefore, over many years numerous laboratory measurements have aimed at providing accurate values of the wavelengths and relative intensities of L-shell transitions in Fe XV-XIX (May et al. 2005), Fe XVI (Graf et al. 2009), Fe XVII (Laming et al. 2000; Gillaspay et al. 2011; Beiersdorfer et al. 2002, 2004; Brown et al. 2006; Shah et al. 2019), Fe XVIII-XXIV (Brown et al. 2002; Chen et al. 2006), Fe XXI – Fe XXIV (Chen et al. 2005), Fe XXIV (Gu et al. 1999; Chen et al. 2002), and Fe XXI-XXIV (Gu et al. 2001). These works have revealed significant discrepancies with theory; well-known problems are the 3C/3D line ratio in Fe XVII (Bernitt et al. 2012; Kühn et al. 2020) and the Fe solar opacity issue (Nagayama et al. 2019). Moreover, it is expected that updated atomic data on Fe L-shell could resolve disparities among collision mod-



els used for predicting the Fe abundance (Mao et al. 2019) in low-temperature (and low-mass) elliptical galaxies (Yates et al. 2017; Mernier et al. 2018). A recent review of astrophysical diagnostics of Fe-L lines can be found in Refs. (Gu et al. 2019; Gu et al. 2020).

Dielectronic recombination (DR) is the dominant photorecombination channel for Fe XVII in such plasmas. In case of DR-LMM this means the capture of an electron into a vacancy of the M shell with a simultaneous, energetically resonant electron L-M excitation. The resulting doubly excited state can either autoionize, resulting in resonant excitation ((Shah et al. 2019) and (Tsuda et al. 2017) for Fe XVII and Fe XV-XVII), or radiatively decay, completing the recombination:



Among the various processes exciting LM emission, DR produces strong 'satellite' transitions very close to the main lines due to the perturbation caused by the added spectator electron (Clementson & Beiersdorfer 2013). Such lines were seen with the *Chandra X-Ray Observatory* in spectra from stellar coronae, like Capella and Procyon, and are used for plasma temperature determination (Beiersdorfer et al. 2018; Gu et al. 2020). DR also strongly influences plasma-ionization equilibrium. It is thus crucial to accurately know these dielectronic satellites when diagnosing temperatures using collision-radiative models (Savin & Laming 2002; Dudík et al. 2019), such as AtomDB (Foster et al. 2012), SPEX (Kaastra et al. 1996), or with the help of atomic databases like CHIANTI (Dere et al. 2019) and OPEN-ADAS<sup>1</sup>.

Except for direct observation of DR  $3l5l'$  and  $3l6l'$  satellites in Fe XXII-XXIV (Gu et al. 2001), no laboratory wavelengths and intensities of Fe DR L-shell satellites are available, as mention in Beiersdorfer et al. (2014). Only recently, DR cross sections for the  $3lnl'$  series for Fe XVII were published, with the purpose of investigating the  $3d \rightarrow 2p$  and  $3s \rightarrow 2p$  line ratios above collision excitation threshold (Shah et al. 2019). These data benchmark the SPEX model and provide constraints on the global fit of Capella spectra (Gu et al. 2020). Continuing those works, we focus on the DR  $3l3l'$  (LMM) satellites of Fe XVII, and provide experimental resonance strengths and rate coefficients. Similar measure-

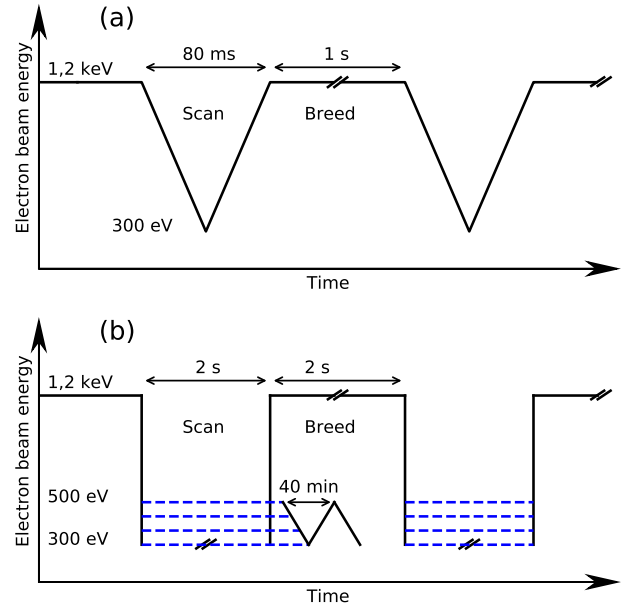


**Figure 1.** (Color online) Time pattern of the electron beam energy sweeping at (a) FLASH-EBIT (Epp et al. 2010) and (b) PolarX-EBIT (Micke et al. 2018). The dashed blue lines indicate slow energy scans between 300 eV and 500 eV with a period of 40 minutes.

ments were previously done for Au (Schneider et al. 1992), Xe (DeWitt et al. 1992) and more recently for Si (Lindroth et al. 2020).

In this work, we remeasured previously studied Fe XVII LMM region by our group (see (Shah et al. 2019)) with another electron beam ion trap (EBIT), PolarX-EBIT (described in (Micke et al. 2018)). By using a modified measurement scheme, we obtained higher electron collision energy resolution and yielded more accurate values on resonance energies and strengths, compared to previous works. We also simulated the dynamical charge-state distribution for the present experimental conditions in order to exclude a possible large depletion of Fe XVII ions due to DR. Furthermore, we inferred the electron beam density for both devices, obtained experimental energies and resonance strengths from the two different measurement schemes, and compared them with earlier photorecombination studies at the Heidelberg Test Storage Ring (TSR) (Schmidt et al. 2009).

In addition, our new calculations based on multiconfiguration Dirac-Fock and our previous ones based on Flexible Atomic Code (FAC) are compared with configuration-interaction predictions by Nilsen (1989) that are compiled in AtomDB (Foster et al. 2012), spectral modeling code widely used in the X-ray astrophysics community. Finally, our experimental and theoretical resonance strengths were converted to DR rate coefficients and compared with the ones in OPEN-ADAS dataset and in Zatsarinny et al. (2004) for a few electron temperatures.

<sup>1</sup> <https://open.adas.ac.uk>

## 2. EXPERIMENT

For accurate values of DR intensities, we rely on two complementary measurements made on two different EBITs. Previous work with FLASH-EBIT at Max-Planck-Institut für Kernphysik in Heidelberg is reported in detail in [Shah et al. \(2019\)](#). We summarize here the method and emphasize the differences with the new measurements performed with PolarX-EBIT. In both devices, Fe atoms are injected into the trap and ionized by a magnetically compressed monoenergetic electron beam with a radius of tens of micrometers. Its negative space-charge potential confines the ions, allowing high stages of ionization to be reached.

The DR-LMM resonances appear at electron energies below the Na-like ionization threshold into Ne-like. This requires to first produce (breed) the Fe XVII of interest before quickly changing the interaction energy to the values to be probed, as described below. Since DR recombination depletes the Ne-like population into Na-like if the probe time is too long, we quantify this small effect in [Sec. 4](#). Our recorded signal, X-ray emission including the contribution from DR was observed at 90° to the beam axis with a silicon-drift detector (SDD) at both EBITs. Its photon energy-resolution was around 120 eV full-width-half-maxima (FWHM) at 6 keV.

### 2.1. FLASH-EBIT measurements

The electron beam energy was at 1.15 keV for a 1 s breeding time, followed by a linear ramp-down from 1.15 to 0.3 keV within 40 ms and a symmetric ramp-up, as shown in [Fig. 1 \(a\)](#) ([Shah et al. 2019](#)), a procedure introduced by [Knapp et al. \(1989, 1993\)](#) also used in many other experiments, e. g. the recent Refs. ([Yao et al. 2010](#); [Xiong et al. 2013](#); [Hu et al. 2013](#)). For such scans, simulations of the ion population predict a negligible DR depletion of the Fe XVII population (seen [Sec. 4](#)).

Every 40 s the ion inventory of the trap was dumped and regenerated to avoid contamination by W and Ba ions that take typically few minutes to accumulate. FLASH-EBIT uses superconductive coils inducing a magnetic field up to 6 T ([Epp et al. 2010](#)) that strongly compresses the electron beam. This beam efficiently produces ions up to the highest charge state allowed by the ionization threshold, in this case Ne-like Fe XVII. The residual pressure at the trap center stays below  $10^{-12}$  mbar, making charge-exchange with residual gas negligible. Therefore, a high-purity sample of Fe xvii ions is prepared ([Shah et al. 2019](#)). The beam current was adjusted according to  $n_e \propto I_e/\sqrt{E}$  to keep the electronic density  $n_e$  constant, having 20 mA at the breeding energy. The measured electron-energy spread was  $\sim 5$  eV.

### 2.2. PolarX-EBIT measurements

New measurements used PolarX-EBIT, operating at PE-TRA III, Deutsches Elektronen-Synchrotron (DESY), Hamburg. It uses an off-axis electron gun and a magnetic field at trap up to 0.86 T ([Micke et al. 2018](#)) produced by an assembly of permanent magnets. It operates at room temperature and had at the time of these measurements a rather poor vacuum ( $10^{-8}$  mbar) which could increase the recombination from Ne-like to Na-like ions through charge exchange process. As observed in [Sec. 4](#), the presence of Na-like ions is not significant. PolarX-EBIT was also run at low beam current, in the present case 2 mA, and thus reached a lower (3.5 eV FWHM at 400 eV) electron-energy spread than FLASH-EBIT. The measurement scheme is different (see [Fig. 1 \(b\)](#)): here, the electron beam varies according to a square-wave scan, instead of a saw-tooth scan. A breeding time of 0.4 s at 1 keV is sufficient to reach Fe XVII population equilibrium, according to both prospective measurements and simulations. The probe energy was maintained for 1 s and varies slowly (minutes) between 300 eV and 500 eV. The electron energy is changed between breeding (constant) and probing values (slowly scanned) by means of a fast (tens of nanoseconds) high-voltage switch. The time evolution of the ion population can thus be observed directly.

## 3. CALCULATIONS

Dielectronic recombination (DR) is a resonant process involving two steps. At first, a dielectronic capture of a free electron into an initial ionic state  $i$  excites a bound electron and forms a doubly excited (or intermediate) state  $d$ . Then, this state may radiatively decay into a final state  $f$ , thereby completing the DR process. Following our previous works ([Shah et al. 2019](#); [Amaro et al. 2017](#); [Shah et al. 2018](#)), we calculate cross sections and resonant strengths in the isolated-resonance approximation, i. e. no quantum interference between DR resonances ([Pindzola et al. 1992](#)), or with non-resonant recombination channels is considered ([Zatsarinny et al. 2006](#); [González Martínez et al. 2005](#); [Tu et al. 2015, 2016](#)). This contribution only influences weak resonances as been previously shown in [Pindzola et al. \(1992\)](#); [Zatsarinny et al. \(2006\)](#). In this approximation, the DR strength is given by

$$S_{idf}^{DR} = \int_0^\infty \sigma_{idf}^{DR}(E_e) dE_e \\ = \frac{\pi^2 \hbar^3}{m_e E_{id}} \frac{g_d}{2g_i} \frac{A_{di}^a A_{df}^r}{\sum_{i'} A_{di'}^a + \sum_{f'} A_{df'}^r}, \quad (2)$$

where  $\sigma_{idf}^{DR}(E_e)$  is the DR cross section as function of the free electron kinetic energy  $E_e$ .  $E_{id}$  is the resonant energy of the electron-ion recombination between state  $i$  and  $d$ , with respective statistical weights  $g_i$  and  $g_d$ , and  $m_e$  is the electron mass. The autoionization rates  $A_{di}^a$  and radiative  $A_{df}^r$  were

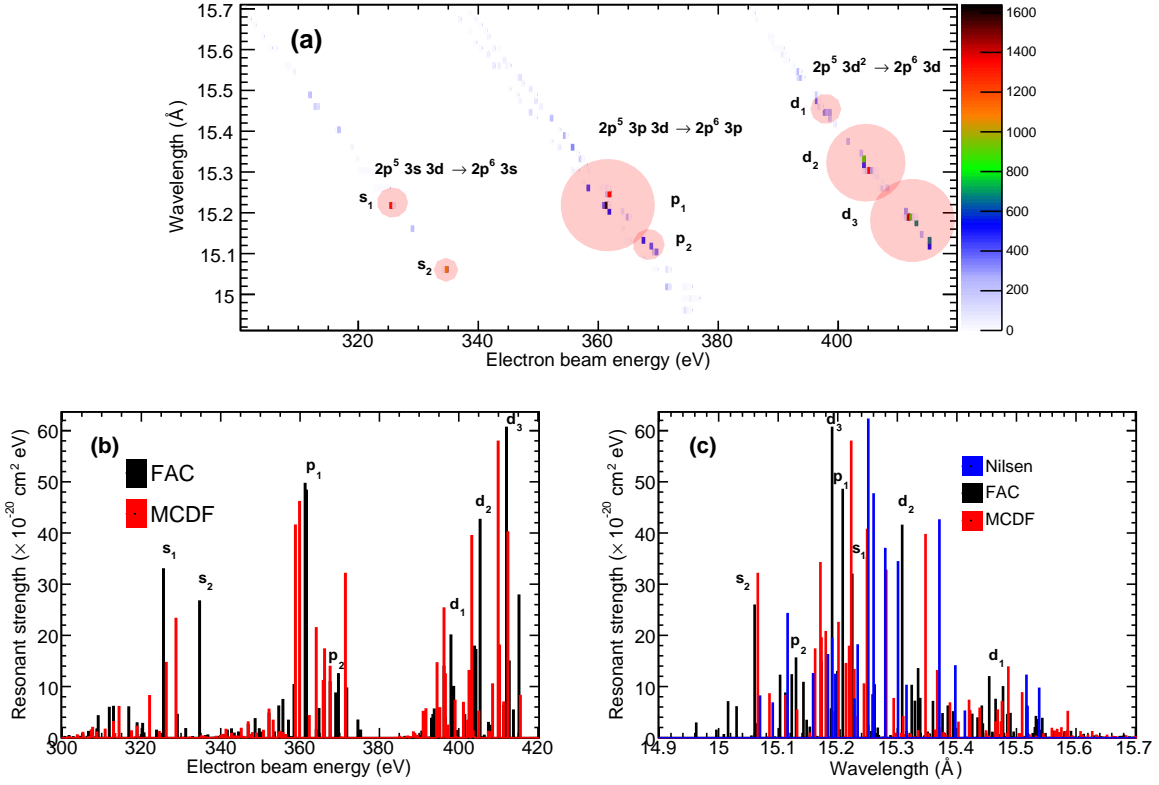


**Figure 2.** Top plot: theoretical resonant strengths obtained from FAC. Abscissa: electron beam energy; ordinate: emitted wavelength. Experimentally resolved spectral lines are labelled as  $s_1$ ,  $s_2$ ,  $p_1$ ,  $p_2$ ,  $d_1$ ,  $d_2$ ,  $d_3$  and  $d_4$ , where the first letter is the  $l$  of the spectator electron in the  $2p^5 3l 3d \rightarrow 2p^6 3l$  transition. The circle diameter shows the relative resonance strength of the channels contributing to these spectral lines. Projection onto both axes are displayed in bottom left (b) and right (c) plots, respectively, and compared with our (MCDF) and Nilsen’s (Nilsen 1989) calculations.

calculated with both Flexible Atomic Code (FAC) and multi-configuration Dirac-Fock (MCDF) methods.

The details of the FAC calculation are given in (Shah et al. 2019). FAC (Gu 2008) provides atomic radial wave functions and respective eigenvalues obtained in a configuration-interaction method with orbitals from a modified electron-electron central potential. This code uses the Distorted Wave (DW) Born approximation for calculating the autoionization rates. Besides the standard configuration-interaction module of FAC, we also considered the many-body perturbation theory (MBPT) (Gu et al. 2006) option of FAC for predicting energies and rates.

Calculations of the energies for the initial, intermediate and final states as well as their respective transition and autoionization rates were also obtained with the Multiconfiguration Dirac Fock General Matrix Elements (MCDFGME) code of Desclaux and Indelicato (Desclaux 1975; Indelicato et al. 1987; Indelicato & Desclaux 1990). Details of the method, including the Hamiltonian and the variational processes employed for retrieving wavefunctions can be found in (Desclaux 1993; Indelicato 1995). In the present calculations, the electronic correlation was restricted to mix-

ing all states of a given  $j$  within an intermediate coupling scheme. Autoionization rates were evaluated using Fano’s single-channel discrete-continuous expansion, which allows for non-orthogonal basis sets between the initial and final states (see Howat et al. (1978) for details). Figure 2 shows our calculations of DR resonant strengths obtained using FAC and the MCDF method, as well as a comparison with Nilsen (1989) values. In the case of DR LMM, most resonances decay through only one strong radiative channel ( $2p^5 3l 3d \rightarrow 2p^6 3l$ , see Fig. 2 (a)). We predicted with FAC the main spectral features that can be experimentally resolved in both EBITs. We found eight spectral lines that have either a single resonance contribution, like  $s_1$ , or a blend of resonances, such as  $p_1$  or  $d_1$ . Note that in our line nomenclature we use the  $l$  of the  $3l$  spectator electron for labeling. The observed line energies and strengths are compared with all theoretical predictions and available literature. Details are given in Appendix A.

For spectral modeling, DR rate coefficients are convenient parameters. They can be obtained by integrating the corresponding DR resonance strengths over a Maxwellian velocity

distribution of the electrons (Gu 2003),

$$\alpha_{if}^{DR} = \frac{m_e}{\sqrt{\pi}\hbar^3} \left( \frac{4E_y}{K_B T_e} \right)^{3/2} a_0^3 \sum_d E_{id} S_{idf}^{DR} e^{-\frac{E_{id}}{K_B T_e}}, \quad (3)$$

where  $E_y$  is the Rydberg constant in energy units,  $a_0$  the Bohr radius,  $K_B$  the Boltzmann constant, and  $T_e$  the electron temperature. A comparison between the present rate coefficients and those available in OPEN-ADAS database is shown in Sec. 5.

#### 4. SIMULATIONS OF THE CHARGE-STATE DISTRIBUTION

To measure DR resonance strengths for a given ionic species, it is necessary to know the charge state distribution of the ions trapped in the EBIT. This is mostly determined by the following charge-changing: collisional ionization (CI), radiative recombination (RR), dielectronic recombination (DR), and charge exchange (CX). Their competition, depending on the measurement conditions and methods determines the overall charge-state distribution. Here, we simulate them following the work of Penetrante et al. (1991) for computing the time evolution of the ion population in the different charged states in an EBIT by using  $Z + 1$  steady-state rate equations,

$$\begin{aligned} \frac{dN_q}{dt} = & n_e v_e [N_{q-1} \sigma_{q-1}^{CI} + N_{q+1} (\sigma_{q+1}^{RR} + \sigma_{q+1}^{DR}) \\ & - N_q \sigma_q^{CI} - N_q (\sigma_q^{RR} + \sigma_q^{DR})] \\ & - N_0 N_q \sigma_q^{CX} \bar{v}_q + N_0 N_{q+1} \sigma_{q+1}^{CX} \bar{v}_{q+1}. \end{aligned} \quad (4)$$

Here,  $N_q$  denotes the population of charge state  $q$ ,  $n_e$  the electron density,  $v_e$  the free-electron velocity,  $\sigma$  the cross section associated to a specific atomic process and  $\bar{v}_q$  the mean (Maxwellian) velocity of an ion with charge  $q$ . The RR total cross sections for Mg-like, Na-like, and Ne-like Fe ions under the present experimental conditions were obtained using FAC, taking into account the principal quantum numbers up to  $n = 15$ . For other Fe charge states, we used the analytical equation of Kim & Pratt (1983) to obtain RR cross sections. CI cross sections from the measurements performed at TSR (Linkemann et al. 1995; Hahn et al. 2013; Bernhardt et al. 2014) for Mg-like, Na-like, and Ne-like Fe ions are also used. These include, apart from the usual direct CI channel, also resonant ionization processes, such as excitation and subsequent autoionization, which become strong starting from the collision excitation threshold ( $\sim 750$  eV). For the remaining charge states, CI cross sections were estimated using the Lotz formula (Lotz 1968). As for the CX cross sections used in our simulations, we applied the analytical expression from Janev et al. (1983) to obtain them. The CX rate is proportional to the residual gas density within the trap region. Thus, by reducing the flow of the iron pentacarbonyl molecular beam in our experiment, we can enhance the population

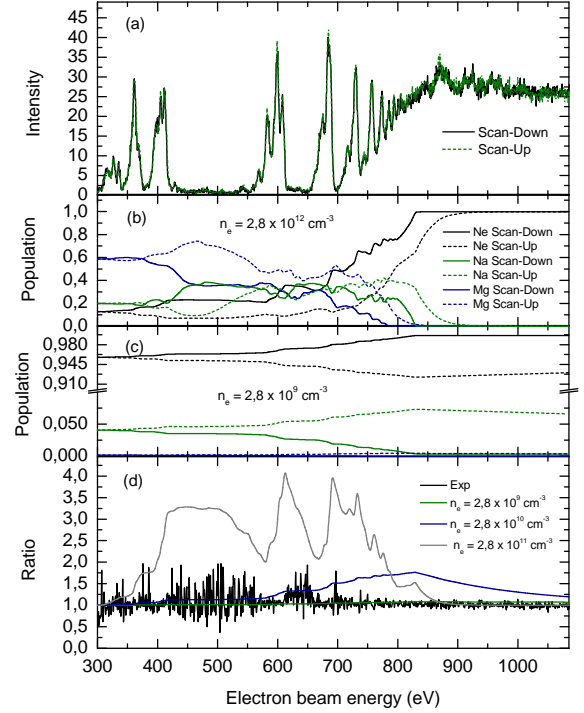


**Figure 3.** (Color online) (a) Spectral maps observed at FLASH-EBIT by scanning upwards and downwards the electron beam energy (see Fig. 1 (a) for timing pattern). Simulations of Fe charge-state distributions as a function of the electron beam energy for effective electron densities of (b)  $2.8 \times 10^{12} \text{ cm}^{-3}$  and (c)  $2.8 \times 10^9 \text{ cm}^{-3}$ . (d) Experimental ratio between downwards and upwards scans compared with simulations for different effective electron densities.

of Fe in higher charge states. For these experiments, it is very important to choose the ratio of ionization time to recombination time appropriately to the simulation parameters. DR is a very strong resonant process; within the resonance width it has cross sections orders of magnitude higher than other collisional processes. This means for our measurement scheme that the Ne-like population in the trap should not be significantly depleted towards lower charge states by the required electron beam energy across the DR resonances. Therefore, we perform simulations for quantifying this depletion. We calculate the corresponding DR rates for Mg-like, Na-like, and Ne-like Fe ions using FAC. Principal quantum numbers of the recombined state up to  $n = 30$  for Ne-like Fe and up to  $n = 10$  for all other relevant ions are taken into account in our calculations, as well as radiative cascades for all relevant atomic processes. With these calculations we then generate synthetic X-ray emission spectra.

##### 4.1. FLASH-EBIT: Simulated charge-state distributions

Using Eq. 4 and scanning parameters presented in Fig. 1, we simulated the time evolution of the charge state distribution during the upward and downward electron beam en-

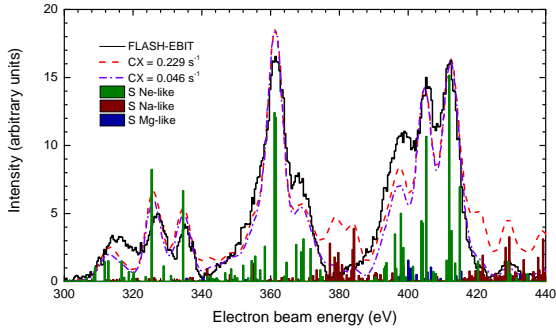


**Figure 4.** (Color online) Theoretical resonant strengths for Ne-like, Na-like and Mg-like Fe ions and simulated fluorescence yield under charge-exchange rates of  $0.229 \text{ s}^{-1}$  and  $0.046 \text{ s}^{-1}$  in comparison with FLASH-EBIT data.

ergy scans in our FLASH-EBIT measurements (Shah et al. 2019), see Fig. 3(a). First, we investigated the effect of the electron-beam density on the Ne-like, Na-like, and Mg-like Fe trapped-ion populations. The panel (b) of Fig. 3 shows an extreme case of electron densities of  $n_e \sim 10^{12} \text{ cm}^{-3}$ , where the Ne-like population is drastically depleted into the Na-like and Mg-like ones due to strong DR resonances. In contrast, at  $n_e \sim 10^9 \text{ cm}^{-3}$ , this effect found to be negligible (panel (c)). In panel (d) of Fig. 3, we display the experimental ratio of the rapid upward and downward energy scans, which shows a negligible effect of the scanning direction on Fe xvii ion density in the trap. This stands in contrast with other experiments using slow scans, where the two scanning directions show clear differences in the distribution of charge states. We compared our present experimental ratio with simulations for different electron densities and found out that below  $5 \times 10^9 \text{ cm}^{-3}$  only a negligible charge-state depletion due to LMM DR resonances takes place.

Second, we investigated the influence of CX on the Fe xvii ion population distribution. FLASH-EBIT has a four-stage differential pumping system for injecting an atomic or molecular beam into the trap, where the ions are generated. The first two stages operate at room temperature at pressures of  $\sim 8 \times 10^{-9}$  mbar. Two additional stages operate cryogenically at 45 K and 4 K, and further constrain the gas flow into the trap region. This brings the residual gas pressure well below  $\leq 10^{-11}$  mbar at the trap center and tremendously reduces the CX rates. For the study of a possible influence of CX in our measurements, we simulated the ion population and generated synthetic X-ray spectra for CX rates of  $0.23 \text{ s}^{-1}$  and  $0.05 \text{ s}^{-1}$ , see Fig. 4. When Fe XVI and Fe XV ions are produced by CX, distinct DR resonances of these ions appear at beam energies of 380 eV and 440 eV. Since those resonances were not observed, we conclude that under the present conditions the dominant Ne-like Fe ion population was maintained during the FLASH-EBIT measurements (Shah et al. 2019).

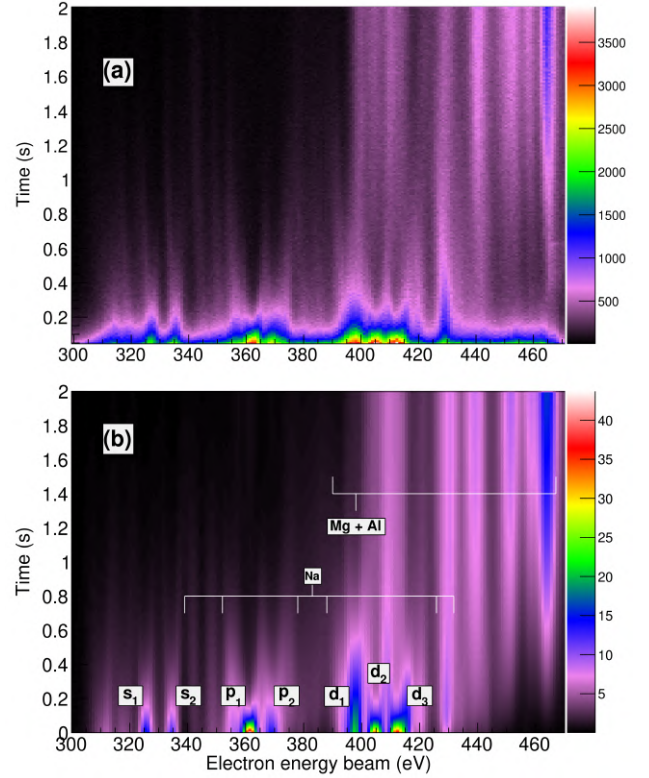


**Figure 5.** (Color online) (a) Measured fluorescence yield as a function of electron beam energy and probing time at Polar-X EBIT. (b) Simulation of the DR emission at the experimental conditions.

#### 4.2. PolarX-EBIT: Simulated charge-state distributions

We also simulated the time evolution of the charge state distribution and its effect on the observed LMM DR X-ray emission for PolarX-EBIT conditions. With the technique shown in Fig. 1 (b), we can also measure these quantities while scanning the electron beam energy. We compare measurement and simulation in Fig. 5. For probing times of less than 100 ms, we observe a dominant population of Ne-like ions with a small population of Na-like and Mg-like Fe ions. Slightly higher intensities of Na-like and Mg-like LMM resonances are seen in Fig. 5 (also see Fig. 4 for resonance energy positions). Simulations yield populations of 0.922, 0.075, and 0.003 for Ne-like, Na-like, and Mg-like Fe ions, respectively, at the breeding electron beam energy of 1.2 keV. The most intense Ne-like resonances exhibit decay times between 0.07 and 0.13 s in our experiment, while Na-like resonances (e.g. at 345 eV, 380 eV, and 435 eV beam energies) reach their maxima between 0.2 and 0.4 s as the Ne-like population starts to deplete. For probing times longer than 1 s, the spectra are dominated by DR emission from Mg-like and Al-like Fe populations. We also observe a constant x-ray emission background in our experiment, which cannot be explained by simulations under any conditions of electron density and CX

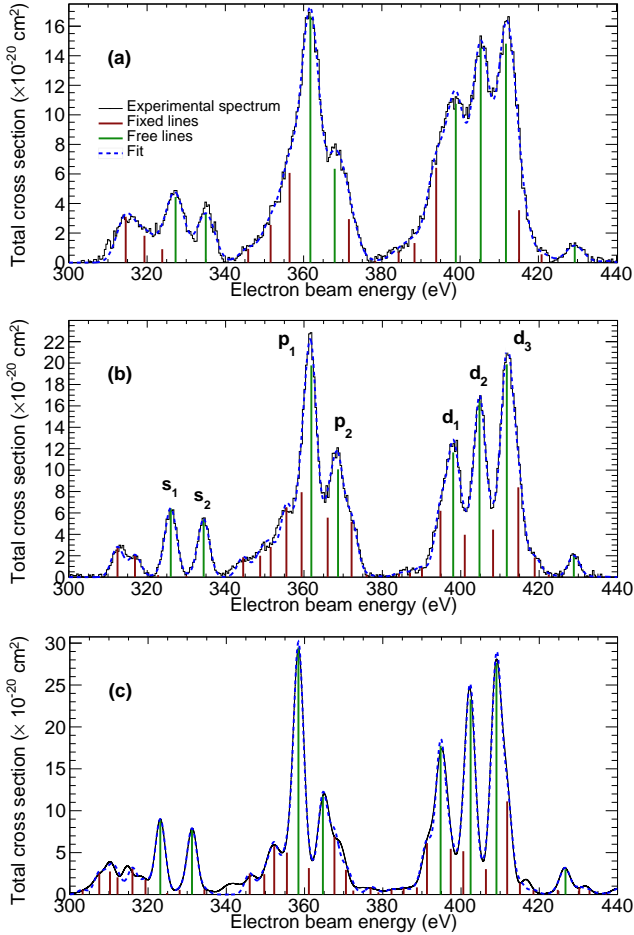


**Figure 6.** Experimental results from (a) FLASH-EBIT, (b) PolarX-EBIT, and (c) TSR measurements, respectively. Black curves represent the experimental spectra, the fitting model is shown in blue. Vertical lines mark position and amplitude of each DR LMM resonance (red: fixed energies, green: free energies in the fitting procedure).

rate. It might be attributed to the delayed photon emission from metastable states. However, no exponential decay of the signal was found in FLASH-EBIT data. Another possible source could be electronic ADC noise caused by switching between power supplies.

Finally, when considering various recombination data either from FAC or MCDF or from TSR measurements in the charge state distribution simulations, we did not see any change in the final synthetic spectrum. Also, this does not change our conclusion that neither spurious charge states other than Ne-like Fe nor charge-state depletion due to DR significantly affect any of the two measurements.

## 5. DATA ANALYSIS

Experimental spectra observed in FLASH-EBIT, PolarX-EBIT, and TSR measurements are shown in Fig. 6. In the case of PolarX-EBIT, as explained in Sec. 4, we have only

selected the first 50 ms of data in order to avoid possible charge state depletion due to the DR and CX processes, see Fig. 5. The strong and well-isolated DR resonances were identified in Sec. 3, which are clearly resolved with an excellent collision energy resolution provided by both EBITs. The TSR data have a significantly better resolution than the EBIT results. However, for this comparison purpose, we convolved them with a Gaussian to match the EBIT resolution (for a complete data set, see (Schmidt et al. 2009; Shah et al. 2019)). First, we calibrated the electron beam energy axis using the theoretical values of the  $p_1$  and  $d_3$  resonances obtained from FAC and MCDF. The experimental spectra were then fitted with a linear combination of Gaussian functions with widths given by the apparatus resolution, as the natural widths of LMM DR resonances are much smaller than the electron beam energy spread. We assumed a linear background from RR continua in our fitting procedure. An electron beam energy resolution of 5.4 eV and 3.5 eV was obtained from the well-isolated  $p_1$  resonance at a beam energy of 360 eV for FLASH-EBIT and PolarX-EBIT, respectively. According to our calculations, there are more than  $\sim 200$  LMM DR resonances within the experimental scanning range. Therefore, to simplify the fit, (i) only resonances separated by more than half the full-width at half maximum (FWHM) of the electron beam energy spread were individually considered, (ii) the centroids of the eight strongest resonances were set as free parameters, (iii) the positions of weak and blended resonances were fixed and bundled into a single one, and (iv) the widths for all resonances were fixed to the respective electron beam energy spread. Weak and blended resonances near strong ones can influence their fitted positions and amplitudes. To estimate this effect, we randomly varied positions of such weak features within half the FWHM of a DR resonance, and fitted the spectrum again with the procedure described above. These results were then compared with those of previous fits, and the differences between them were quadratically added to final uncertainties presented in Table 1 and 2.

The DR resonance strengths were calibrated against the DR resonance  $d_3$  at 412 eV beam energy in both EBIT spectra. A cross section calibration using the RR emission, as in works of (Schneider et al. 1992; Brown et al. 2006; Chen 2008), was not possible in any of two measurements due to insufficient detector resolution, pileup, and contamination of the RR band (*cf.* Fig. 1 of Shah et al. (2019)). Details of calibration are explained in our previous work (Shah et al. 2019). In EBITs, the unidirectional electron beam causes anisotropic and polarized x-ray emission. We observed photons at  $90^\circ$  with respect to the electron beam. We thus apply a correction factor defined as  $W(90^\circ) = 3/(3 - P)$ , where  $P$  is the polarization for a specific radiative transition (Shah et al. 2018). The calculated polarization values are taken

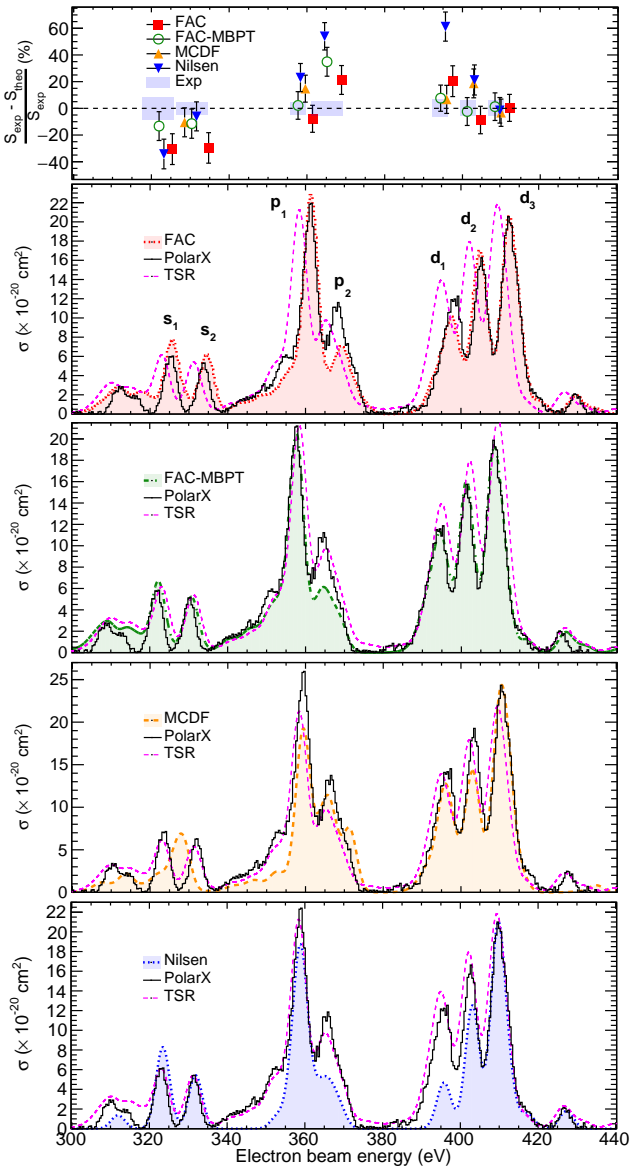


**Figure 7.** PolarX-EBIT and TSR measurements and theoretical total DR cross sections obtained using FAC, FAC-MBPT, MCDF, as well as literature values from Nilsen (1989). Calculations were convolved with a Gaussian of 4.5 eV FWHM for the comparison. The top scatter plot compares theory and experiment.

from Shah et al. (2019), which also agree with measurements performed by Chen et al. (2004). With this correction we obtain the total cross sections using  $S^{\text{total}} = 4\pi I^{90^\circ} / W(90^\circ)$  relation, where  $I^{90^\circ}$  is the observed DR intensity.

## 6. RESULTS AND DISCUSSION

Table 1 lists the resonant energies inferred from each measurement. For the comparison in Fig. 7, we also fitted the synthetic spectra from FAC, FAC-MBPT, and MCDF with the same procedure that was applied to the experimental

spectra. Typically, FAC and FAC-MBPT energy positions show less than  $\sim 0.3\%$  relative departures from the experimental values, while MCDF values only agree within  $\sim 1\%$ . Distinct disagreements of MCDF predictions are visible for the  $s_1$ ,  $s_2$  and  $p_2$  resonances. DR resonances from these features show a larger energy splitting in the MCDF predictions than in FAC and FAC-MBPT ones. The opposite effect was seen in other two distinct features,  $s_1$  and  $s_2$ , where energy separations predicted by MCDF were smaller than the FAC, FAC-MBPT, and experimental values. Moreover, a clear resonance next to the  $d_3$  line at 425 eV is not predicted by MCDF. Overall, it can be stated that FAC and FAC-MBPT energy predictions provide better agreement with experiments than MCDF. The reason behind this might be that the MCDFGME package we have used in the present work could not generate reliable Auger rates with correlation to other configurations beyond minimal coupling, which would be necessary to improve the energy centroids.

Table 2 presents experimentally inferred total resonant strengths. For the resonance strengths determinations with FLASH-EBIT and PolarX-EBIT, we estimate total uncertainties on the level of  $\sim 20\%$  and  $\sim 17\%$ , respectively. The largest contributions to the error budget arise from the influence of blended weak DR features. For the TSR results, we assume the quoted uncertainty of 20% from the original work by Schmidt et al. (2009). By combining the three independent measurements, we obtain final values for the resonance strengths  $S_{\text{EXP}}$  and their respective uncertainties, found to be at the level of  $\sim 10\%$ . Fig. 7 shows a comparison with predictions by FAC, FAC-MBPT, MCDF, and by Nilsen (1989). Overall, the resonance strength predictions are in good agreement with the measurements. However,  $s_1$ ,  $s_2$ , and  $p_2$  disagree with MCDF theory, as noted earlier. Furthermore, no calculations can effectively predict the resonance strength of the  $p_2$  feature. EBIT and TSR data also disagree here; since simulations seem to exclude spurious features at this energy in EBITs, at present we do not have an explanation for this.

In addition to DR resonance strengths, we also obtained DR rate coefficients using Eq. (3) for different plasma electron temperatures. Table 3 lists our experimentally inferred and theoretical DR rate coefficients from  $S_{\text{EXP}}$  together with those available in the OPEN-ADAS and AtomDB databases.

As usual in OPEN-ADAS, we identified and compared our DR rates by the respective final-state configuration of the Na-like Fe ion. Combined total rates for the  $3s$ ,  $3p$ , and  $3d$  final configurations are presented in Tab. 3. Since some minor final-state configurations are shared by the main experimental spectral features only experimental total rates are given in Table 3. Our experimental rate coefficients generally agree within  $\sim 3\text{--}8\%$  with the theoretical FAC-MBPT and MCDF rates. However, we found discrepancies with the corresponding DR rates in the OPEN-ADAS database. It overestimates

**Table 1.** Experimental and theoretical (FAC-CI, FAC-MBPT, and MCDF) DR resonance energies. Round brackets: relative difference in percent between measured and theoretical energy positions, where each measurement is independently calibrated with  $p_1$  and  $d_3$  values from respective theories.  $CE$  stands for combined energy values obtained by fitting the synthetic spectra (all energies given in eV).

Label	$E_{FLASH}$	$E_{PolarX}$	$E_{TSR}$	$CE_{FAC}$	$CE_{FAC-MBPT}$	$CE_{MCDF}$
$s_1$	$322.8 \pm 0.9$	$321.5 \pm 0.03$	$323.2 \pm 0.2$	325.64 (-0.15%)	322.24 (-0.23%)	
$s_2$	$330.7 \pm 0.3$	$330 \pm 0.03$	$331.2 \pm 0.1$	334.75 (-0.31%)	330.65 (-0.18%)	
$p_1$			$358.3 \pm 0$	361.52	357.8	359.60
$p_2$	$364.1 \pm 0.3$	$364.7 \pm 0.02$	$364.73 \pm 0.1$	369.18 (-0.2%)	365.31 (-0.17%)	364.93 (0.62%)
						371.52
$d_1$	$395.7 \pm 0.4$	$394.1 \pm 0.03$	$394.7 \pm 0.03$	397.71 (0.05%)	394.44 (-0.08%)	395.95 (0.005%)
$d_2$	$401.9 \pm 0.3$	$401.6 \pm 0.02$	$402.6 \pm 0.1$	404.87 (0.13%)	401.32 (0.06%)	402.95 (0.01%)
$d_3$			$409.14 \pm 0.04$	412.37	408.55	410.18

**Table 2.** Experimental resonant strengths ( $10^{-20} \text{cm}^2 \text{eV}$ ) compared to values obtained with FAC, MCDF (this work) and reported by Nilsen (1989). Listed experimental cross sections were calibrated with the FAC-MBPT theoretical value of the  $d_3$  feature. Round brackets: relative difference in percent between measured and theoretical resonant strengths, where each measurement is independently calibrated with the  $d_3$  value from respective theories.

Label	$S_{FLASH}$	$S_{PolarX}$	$S_{TSR}$	$S_{EXP}$	$S_{FAC}$	$S_{FAC-MBPT}$	$S_{MCDF}$	Nilsen (1989)
$s_1$	$23 \pm 5$	$26 \pm 4$	$28 \pm 6$	$25 \pm 3$	33.99 (-31%)	28.72 (-13%)	8.17 (71%)	36.95 (-35%)
$s_2$	$18 \pm 4$	$21 \pm 4$	$25 \pm 5$	$21 \pm 2$	27.87 (-31%)	23.28 (-12%)	26.27 (-10%)	24.24 (-7%)
$p_1$	$87 \pm 16$	$82 \pm 13$	$98 \pm 20$	$87 \pm 9$	96.62 (-8%)	85.18 (2%)	84.4 (15%)	73.58 (22%)
$p_2$	$34 \pm 7$	$41 \pm 8$	$35 \pm 7$	$37 \pm 4$	29.53 (21%)	24.12 (34%)	73.94 (-83%)	17.95 (54%)
$d_1$	$53 \pm 10$	$48 \pm 8$	$54 \pm 11$	$50 \pm 5$	41.67 (20%)	47.29 (7%)	53.63 (6%)	21.68 (60%)
$d_2$	$76 \pm 14$	$63 \pm 11$	$64 \pm 13$	$67 \pm 7$	74.29 (-9%)	68.44 (-3%)	60.2 (19%)	56.85 (20%)
$d_3$			$90 \pm 18$	$87 \pm 9$	88.76 (0.3%)	86.14 (1%)	101.96 (-4%)	95.84 (-2%)

rates by as much as  $\sim 7$ – $60\%$  for the total rates, in comparison with our experimental and theoretical results. Similar discrepancies were found with rates from the AtomDB spectral modeling database (taken from Nilsen (1989)), which are  $\sim 30\%$  lower than the experimental values. The total DR rates obtained with AUTOSTRUCTURE code (Zatsarinny et al. 2004) show slightly lesser overestimation ( $\sim 10\%$ ).

## 7. SUMMARY AND CONCLUSIONS

The DR LMM resonances for Fe xvii ions have been measured using two different EBITs and compared with results obtained at the Test Storage Ring (Schmidt et al. 2009). We simulated the time-dependent charge-state distribution to rule out systematic effects due to the presence of spurious charge states and depletion of charge states due to DR that may affect our resonance strength measurements. The results extracted from all three experiments were compared with cal-

culations performed using FAC, FAC-MBPT, and MCDF codes. Among them, FAC-MBPT shows the best agreement with the experiments. We also derive LMM DR rate coefficients from our experimental data for several temperatures. Our experimental rates show significant discrepancies with the OPEN-ADAS database and the AtomDB spectral modeling package, which are frequently used for the analysis of astrophysical spectra. Such discrepancies highlight how crucial laboratory measurements are for testing spectral models. This not only important in the perspective of upcoming X-ray satellite missions *XRISM* (Tashiro et al. 2018) and *Athena* (Barret et al. 2016), which will soon provide high-resolution spectra using X-ray microcalorimeters (Durkin et al. 2019), but also for interpreting available high-resolution spectra from the operating *Chandra* and *XMM-Newton* obser-



**Table 3.** Experimental DR rate coefficients ( $\times 10^{-13} \text{ cm}^3 \text{ s}^{-1}$ ) for a few electron temperatures  $T_e$  (eV) compared to values obtained with OPEN-ADAS, FAC-MBPT, MCDF, by Nilsen (1989) and by Zatsarinny et al. (2004). The label indicates the orbital of the decoupled electron in the final state after DR emission.

Label	$T_e$	Exp	OPEN-ADAS	FAC-MBPT	MCDF	Nilsen (1989)	Zatsarinny et al. (2004) <sup>a</sup>
s	100		5.88	7.69	5.45	5.65	
	300		11.7	12.8	9.71	9.51	
	2000		1.97	1.89	1.48	1.39	
p	100		14.0	15.7	14.2	8.97	
	300		42.8	31.9	30.0	19.1	
	2000		9.11	5.12	4.86	3.08	
d	100		13.5	15.4	13.4	8.94	
	300		52.6	41.3	37.5	25.9	
	2000		12.2	7.46	6.86	4.75	
total	100	$36 \pm 2$	33.4	38.8	33.1	23.6	38.0
	300	$81 \pm 5$	107.1	86.0	77.2	54.5	90.3
	2000	$14 \pm 1$	23.3	14.5	13.2	9.22	15.3

<sup>a</sup> Only total DR rates are provided.

vatories (Gu et al. 2020) needed for reliably plasma diagnostics (Beiersdorfer et al. 2014, 2018).

#### ACKNOWLEDGMENTS

P. A. acknowledges the support from Fundação para a Ciência e a Tecnologia (FCT), Portugal, under Grant

No. UID/FIS/04559/2020(LIBPhys) and under Contract No. SFRH/BPD/92329/2013. Work by C. S. was supported by the Max-Planck-Gesellschaft (MPG), by Deutsche Forschungsgemeinschaft (DFG) Project No. 266229290, and by an appointment to the NASA Postdoctoral Program at the NASA Goddard Space Flight Center, administered by Universities Space Research Association under contract with NASA. We thanks Prof. Dr. Stefan Schippers for providing the raw data of Fe XVII DR rates measured at the Test Storage Ring in Heidelberg, Germany.

#### APPENDIX

##### A. DR CALCULATIONS FOR Fe XVII

Table 4 contains the resonance energies, strengths for the main spectral features, which were benchmarked within this work. The emitted wavelengths of the decay channels are listed in Table 5 with additional data provided by Nilsen (1989) and Beiersdorfer et al. (2014).

The complete set of resonance energies, strengths, and emitted wavelengths used for the synthetic spectra shown in Fig. 7, as well as for calculation of DR rates listed in Table 3, are available online as machine-readable tables.

#### REFERENCES

- Amaro, P., Shah, C., Steinbrügge, R., et al. 2017, Physical Review A, 95, 022712, doi: [10.1103/PhysRevA.95.022712](https://doi.org/10.1103/PhysRevA.95.022712)
- Barret, D., Trong, T. L., den Herder, J.-W., et al. 2016, Proc. SPIE, 9905, 99052F. <https://doi.org/10.1117/12.2232432>
- Beiersdorfer, P., Bitter, M., von Goeler, S., et al. 2004, The Astrophysical Journal, 610, 616, doi: [10.1086/421512](https://doi.org/10.1086/421512)

**Table 4.** Theoretical values of the peak resonant energies  $E$  (eV) and strengths  $S$  ( $10^{-20}\text{cm}^2\text{eV}$ ) obtained in this work with FAC, FAC-MBPT and MCDF. The resonant and final states are given in  $j-j$  and LSJ notations.

Label	Intermediate state	Final state	$E_{\text{FAC}}$	$E_{\text{MBPT}}$	$E_{\text{MCDF}}$	$S_{\text{FAC}}$	$S_{\text{MBPT}}$	$S_{\text{MCDF}}$
	$(((2p_{1/2}^2 2p_{3/2}^3)_{3/2} 3s_{1/2})_2 3d_{5/2})_{1/2}$	$^4D_{1/2} \quad 3s_{1/2} 2^2S_{1/2}$	313.06	310.23	313.08	6.04	6.42	2.74
$s_1$	$(((2p_{1/2} 2p_{3/2}^4)_{1/2} 3s_{1/2})_1 3d_{5/2})_{3/2}$	$^2D_{3/2} \quad 3s_{1/2} 2^2S_{1/2}$	325.70	322.21	321.98	31.91	29.54	7.34
$s_2$	$(((2p_{1/2} 2p_{3/2}^4)_{1/2} 3s_{1/2})_1 3d_{3/2})_{3/2}$	$^2P_{3/2} \quad 3s_{1/2} 2^2S_{1/2}$	334.62	330.72	328.60	25.89	23.22	20.61
	$(((2p_{1/2}^2 2p_{3/2}^3)_{3/2} 3p_{1/2})_2 3d_{5/2})_{3/2}$	$^4P_{3/2} \quad 3p_{1/2} 2^2P_{1/2}$	341.50	338.94	339.95	1.04	1.11	0.24
	$(((2p_{1/2}^2 2p_{3/2}^3)_{3/2} 3p_{3/2})_0 3d_{5/2})_{5/2}$	$^2D_{5/2} \quad 3p_{3/2} 2^2P_{3/2}$	354.47	351.41	352.30	6.16	7.99	4.59
	$(((2p_{1/2} 2p_{3/2}^4)_{1/2} 3p_{1/2})_1 3d_{5/2})_{5/2}$	$^4F_{5/2} \quad 3p_{3/2} 2^2P_{3/2}$	355.8	353.04	354.05	5.14	4.95	0.04
$p_1$	$(((2p_{1/2} 2p_{3/2}^4)_{1/2} 3p_{1/2})_1 3d_{3/2})_{3/2}$	$^4F_{3/2} \quad 3p_{1/2} 2^2P_{1/2}$	353.65	355.05	352.28	1.06	9.70	0.16
	$(((2p_{1/2} 2p_{3/2}^4)_{1/2} 3p_{1/2})_1 3d_{3/2})_{3/2}$	$^4F_{3/2} \quad 3p_{3/2} 2^2P_{3/2}$	353.65	355.05	352.28	0.008	0.22	0.32
	$(((2p_{1/2} 2p_{3/2}^4)_{1/2} 3p_{3/2})_2 3d_{5/2})_{5/2}$	$^2D_{5/2} \quad 3p_{3/2} 2^2P_{3/2}$	358.36	355.09	356.22	0.03	0.61	0.48
	$(((2p_{1/2} 2p_{3/2}^4)_{1/2} 3p_{1/2})_1 3d_{3/2})_{3/2}$	$^2D_{3/2} \quad 3p_{1/2} 2^2P_{1/2}$	361.25	357.38	358.83	48.50	47.02	38.59
	$(((2p_{1/2}^2 2p_{3/2}^3)_{3/2} 3p_{3/2})_2 3d_{5/2})_{5/2}$	$^2D_{5/2} \quad 3p_{3/2} 2^2P_{3/2}$	361.67	358.04	359.77	35.26	34.74	30.35
	$(((2p_{1/2} 2p_{3/2}^4)_{1/2} 3p_{1/2})_1 3d_{3/2})_{1/2}$	$^2S_{1/2} \quad 3p_{1/2} 2^2P_{1/2}$	361.71	358.42	367.70	12.90	12.36	12.68
$p_2$	$[(2s_{1/2} 2p_{1/2}^2 2p_{3/2}^4)_{1/2} 3s_{1/2}^2]_{1/2}$	$3p_{3/2} 2^2P_{3/2}$	364.85	361.80		5.56	4.45	
	$(((2p_{1/2} 2p_{3/2}^4)_{1/2} 3p_{3/2})_2 3d_{3/2})_{1/2}$	$^2P_{1/2} \quad 3p_{3/2} 2^2P_{3/2}$	367.42	363.36	364.06	10.77	11.87	19.61
	$(((2p_{1/2} 2p_{3/2}^4)_{1/2} 3p_{3/2})_1 3d_{3/2})_{5/2}$	$^2D_{5/2} \quad 3p_{3/2} 2^2P_{3/2}$	368.99	364.74	371.33	8.69	4.43	29.69
	$(((2p_{1/2} 2p_{3/2}^4)_{1/2} 3p_{3/2})_1 3d_{5/2})_{3/2}$	$^2D_{3/2} \quad 3p_{3/2} 2^2P_{3/2}$	369.50	365.35	366.12	12.17	11.39	16.64
$d_1$	$(((2p_{1/2}^2 2p_{3/2}^3)_{3/2} 3d_{3/2})_2 3d_{5/2})_{5/2}$	$^4G_{5/2} \quad 3d_{3/2} 2^2D_{3/2}$	396.39	393.3	396.73	9.42	11.46	11.37
	$(((2p_{1/2}^2 2p_{3/2}^3)_{3/2} 3d_{5/2}^2)_{7/2}$	$^4D_{7/2} \quad 3d_{5/2} 2^2D_{5/2}$	397.93	394.65	396.22	11.89	13.96	12.55
$d_2$	$(((2p_{1/2} 2p_{3/2}^4)_{1/2} 3d_{5/2}^2)_{7/2}$	$^2G_{7/2} \quad 3d_{5/2} 2^2D_{5/2}$	404.14	400.95	402.46	13.45	12.08	11.92
	$(((2p_{1/2} 2p_{3/2}^4)_{1/2} 3d_{3/2})_2 3d_{5/2})_{5/2}$	$^2F_{5/2} \quad 3d_{3/2} 2^2D_{3/2}$	404.45	401.05	402.21	10.19	24.19	1.33
	$(((2p_{1/2} 2p_{3/2}^4)_{1/2} 3d_{3/2})_2 3d_{5/2})_{5/2}$	$^2F_{5/2} \quad 3d_{5/2} 2^2D_{5/2}$	404.45	401.05	402.21	7.00	6.27	1.78
	$(((2p_{1/2} 2p_{3/2}^4)_{1/2} 3d_{5/2}^2)_{5/2}$	$^2F_{5/2} \quad 3d_{3/2} 2^2D_{3/2}$	405.22	401.98	403.14	41.48	23.62	35.91
$d_3$	$(((2p_{1/2} 2p_{3/2}^4)_{1/2} 3d_{5/2}^2)_{1/2}$	$^2P_{1/2} \quad 3d_{3/2} 2^2D_{3/2}$	411.16	407.57	408.61	6.25	7.53	9.59
	$(((2p_{1/2} 2p_{3/2}^4)_{1/2} 3d_{3/2})_1 3d_{5/2})_{7/2}$	$^2F_{7/2} \quad 3d_{5/2} 2^2D_{5/2}$	411.90	407.96	410.07	60.63	58.13	52.73
	$(((2p_{1/2} 2p_{3/2}^4)_{1/2} 3d_{3/2})_1 3d_{5/2})_{5/2}$	$^2D_{5/2} \quad 3d_{5/2} 2^2D_{5/2}$	412.85	408.75	410.29	14.74	13.79	16.84
	$(((2p_{1/2} 2p_{3/2}^4)_{1/2} 3d_{3/2})_1 3d_{5/2})_{3/2}$	$^2P_{3/2} \quad 3d_{3/2} 2^2D_{3/2}$	415.20	411.12	412.39	12.26	12.66	17.84
	$(((2p_{1/2} 2p_{3/2}^4)_{1/2} 3d_{3/2})_1 3d_{5/2})_{3/2}$	$^2P_{3/2} \quad 3d_{5/2} 2^2D_{5/2}$	415.20	411.12	412.39	15.55	16.92	18.24
	$(((2p_{1/2} 2p_{3/2}^4)_{1/2} 3d_{5/2}^2)_{1/2}$	$^2P_{1/2} \quad 3d_{3/2} 2^2D_{3/2}$	420.27	416.73	415.67	6.01	5.39	7.49

**Table 5.** Theoretical values of emitted wavelengths (Å) obtained in this work with FAC, FAC-MBPT, and MCDF. The resonant and final states are given in  $j-j$  and LSJ notations. Respective data provided by [Nilsen \(1989\)](#) and by [Beiersdorfer et al. \(2014\)](#) are also listed for comparison.

Label	Intermediate state	Final state	$W_{\text{FAC}}$	$W_{\text{FAC-MBPT}}$	$W_{\text{MCDF}}$	Nilsen (1989)	Beiersdorfer et al. (2014)
	$[(2p_{1/2}^2 2p_{3/2}^3)_{3/2} 3s_{1/2}] 2 3d_{5/2} ]_{1/2}$	$^4D_{1/2} \quad 3s_{1/2}^2 S_{1/2}$	15.47	15.52	15.46	15.52	15.49
$s_1$	$[(2p_{1/2} 2p_{3/2}^4)_{1/2} 3s_{1/2}] 1 3d_{5/2} ]_{3/2}$	$^2D_{3/2} \quad 3s_{1/2}^2 S_{1/2}$	15.23	15.29	15.29	15.28	15.27
$s_2$	$[(2p_{1/2} 2p_{3/2}^4)_{1/2} 3s_{1/2}] 1 3d_{3/2} ]_{3/2}$	$^2P_{3/2} \quad 3s_{1/2}^2 S_{1/2}$	15.06	15.13	15.17	15.12	15.11
	$[(2p_{1/2}^2 2p_{3/2}^3)_{3/2} 3p_{1/2}] 2 3d_{5/2} ]_{3/2}$	$^4P_{3/2} \quad 3p_{1/2}^2 P_{1/2}$	15.59	15.63	15.61	15.58	
	$[(2p_{1/2}^2 2p_{3/2}^3)_{3/2} 3p_{3/2}] 0 3d_{5/2} ]_{5/2}$	$^2D_{5/2} \quad 3p_{3/2}^2 P_{3/2}$	15.38	15.44	15.42	15.63	
	$[(2p_{1/2} 2p_{3/2}^4)_{1/2} 3p_{1/2}] 1 3d_{5/2} ]_{5/2}$	$^4F_{5/2} \quad 3p_{3/2}^2 P_{3/2}$	15.36	15.41	15.39	15.41	15.41
$p_1$	$[(2p_{1/2} 2p_{3/2}^4)_{1/2} 3p_{1/2}] 1 3d_{3/2} ]_{3/2}$	$^4F_{3/2} \quad 3p_{1/2}^2 P_{1/2}$	15.35	15.32	15.37	15.40	15.30
	$[(2p_{1/2} 2p_{3/2}^4)_{1/2} 3p_{1/2}] 1 3d_{3/2} ]_{3/2}$	$^4F_{3/2} \quad 3p_{3/2}^2 P_{3/2}$	15.40	15.38	15.42	15.45	
	$[(2p_{1/2} 2p_{3/2}^4)_{1/2} 3p_{3/2}] 2 3d_{5/2} ]_{5/2}$	$^2D_{5/2} \quad 3p_{3/2}^2 P_{3/2}$	15.26	15.37	15.35	15.37	
	$[(2p_{1/2} 2p_{3/2}^4)_{1/2} 3p_{1/2}] 1 3d_{3/2} ]_{3/2}$	$^2D_{3/2} \quad 3p_{1/2}^2 P_{1/2}$	15.21	15.27	15.25	15.26	15.26
	$[(2p_{1/2}^2 2p_{3/2}^3)_{3/2} 3p_{3/2}] 2 3d_{5/2} ]_{5/2}$	$^2D_{5/2} \quad 3p_{3/2}^2 P_{3/2}$	15.25	15.31	15.28	15.55	15.29
	$[(2p_{1/2} 2p_{3/2}^4)_{1/2} 3p_{1/2}] 1 3d_{3/2} ]_{1/2}$	$^2S_{1/2} \quad 3p_{1/2}^2 P_{1/2}$	15.20	15.26	15.08	15.25	15.07
$p_2$	$[(2s_{1/2} 2p_{1/2}^2 2p_{3/2}^4)_{1/2} 3s_{1/2}^2]_{1/2}$	$3p_{3/2}^2 P_{3/2}$	15.19	15.24		15.23	15.24
	$[(2p_{1/2} 2p_{3/2}^4)_{1/2} 3p_{3/2}] 2 3d_{3/2} ]_{1/2}$	$^2P_{1/2} \quad 3p_{3/2}^2 P_{3/2}$	15.14	15.21	15.20	15.19	15.19
	$[(2p_{1/2} 2p_{3/2}^4)_{1/2} 3p_{3/2}] 1 3d_{3/2} ]_{5/2}$	$^2D_{5/2} \quad 3p_{3/2}^2 P_{3/2}$	15.11	15.18	15.07	15.17	
	$[(2p_{1/2} 2p_{3/2}^4)_{1/2} 3p_{3/2}] 1 3d_{5/2} ]_{3/2}$	$^2D_{3/2} \quad 3p_{3/2}^2 P_{3/2}$	15.10	15.17	15.16	15.20	15.16
$d_1$	$[(2p_{1/2}^2 2p_{3/2}^3)_{3/2} 3d_{3/2}] 2 3d_{5/2} ]_{5/2}$	$^4G_{5/2} \quad 3d_{3/2}^2 D_{3/2}$	15.48	15.53	15.47	15.54	15.50
	$[(2p_{1/2}^2 2p_{3/2}^3)_{3/2} 3d_{5/2}^2]_{7/2}$	$^4D_{7/2} \quad 3d_{5/2}^2 D_{5/2}$	15.45	15.51	15.49	15.52	15.49
$d_2$	$[(2p_{1/2} 2p_{3/2}^4)_{1/2} 3d_{5/2}^2]_{7/2}$	$^2G_{7/2} \quad 3d_{5/2}^2 D_{5/2}$	15.34	15.39	15.37	15.40	15.37
	$[(2p_{1/2} 2p_{3/2}^4)_{1/2} 3d_{3/2}] 2 3d_{5/2} ]_{5/2}$	$^2F_{5/2} \quad 3d_{3/2}^2 D_{3/2}$	15.32	15.38	15.36	15.38	
	$[(2p_{1/2} 2p_{3/2}^4)_{1/2} 3d_{3/2}] 2 3d_{5/2} ]_{5/2}$	$^2F_{5/2} \quad 3d_{5/2}^2 D_{5/2}$	15.33	15.39	15.37	15.39	
	$[(2p_{1/2} 2p_{3/2}^4)_{1/2} 3d_{3/2}^2]_{5/2}$	$^2F_{5/2} \quad 3d_{3/2}^2 D_{3/2}$	15.31	15.36	15.35	15.37	15.35
$d_3$	$[(2p_{1/2} 2p_{3/2}^4)_{1/2} 3d_{5/2}^2]_{1/2}$	$^2P_{1/2} \quad 3d_{3/2}^2 D_{3/2}$	15.20	15.26	15.24	15.26	15.24
	$[(2p_{1/2} 2p_{3/2}^4)_{1/2} 3d_{3/2}] 1 3d_{5/2} ]_{7/2}$	$^2F_{7/2} \quad 3d_{5/2}^2 D_{5/2}$	15.19	15.26	15.22	15.25	15.23
	$[(2p_{1/2} 2p_{3/2}^4)_{1/2} 3d_{3/2}] 1 3d_{5/2} ]_{5/2}$	$^2D_{5/2} \quad 3d_{5/2}^2 D_{5/2}$	15.17	15.24	15.22	15.23	15.22
	$[(2p_{1/2} 2p_{3/2}^4)_{1/2} 3d_{3/2}] 1 3d_{5/2} ]_{3/2}$	$^2P_{3/2} \quad 3d_{3/2}^2 D_{3/2}$	15.12	15.19	15.17	15.35	15.18
	$[(2p_{1/2} 2p_{3/2}^4)_{1/2} 3d_{3/2}] 1 3d_{5/2} ]_{3/2}$	$^2P_{3/2} \quad 3d_{5/2}^2 D_{5/2}$	15.13	15.20	15.18	15.36	15.18
	$[(2p_{1/2} 2p_{3/2}^4)_{1/2} 3d_{3/2}^2]_{1/2}$	$^2P_{1/2} \quad 3d_{3/2}^2 D_{3/2}$	15.03	15.09	15.11	15.09	15.08

- Beiersdorfer, P., Bode, M. P., Ishikawa, Y., & Diaz, F. 2014, The Astrophysical Journal, 793, 99.  
<http://stacks.iop.org/0004-637X/793/i=2/a=99>
- Beiersdorfer, P., Hell, N., & Lepson, J. K. 2018, The Astrophysical Journal, 864, 24, doi: [10.3847/1538-4357/aad27f](https://doi.org/10.3847/1538-4357/aad27f)
- Beiersdorfer, P., Behar, E., Boyce, K. R., et al. 2002, The Astrophysical Journal Letters, 576, L169.  
<http://stacks.iop.org/1538-4357/576/i=2/a=L169>
- Bernhardt, D., Becker, A., Grieser, M., et al. 2014, Physical Review A, 90, 012702, doi: [10.1103/PhysRevA.90.012702](https://doi.org/10.1103/PhysRevA.90.012702)
- Bernitt, S., Brown, G. V., Rudolph, J. K., et al. 2012, Nature, 492, 225, doi: [10.1038/nature11627](https://doi.org/10.1038/nature11627)
- Brown, G. V. 2008, Canadian Journal of Physics, 86, 199, doi: [10.1139/p07-158](https://doi.org/10.1139/p07-158)
- Brown, G. V., Beiersdorfer, P., Liedahl, D. A., et al. 2002, The Astrophysical Journal Supplement Series, 140, 589, doi: [10.1086/339374](https://doi.org/10.1086/339374)
- Brown, G. V., Beiersdorfer, P., Chen, H., et al. 2006, Phys Rev Lett, 96, 253201, doi: [10.1103/PhysRevLett.96.253201](https://doi.org/10.1103/PhysRevLett.96.253201)
- Chen, G.-X. 2008, Physical Review A, 77, 022703, doi: [10.1103/PhysRevA.77.022703](https://doi.org/10.1103/PhysRevA.77.022703)
- Chen, H., Beiersdorfer, P., Robbins, D., Smith, A., & Gu, M. 2004, Polarization measurement of Iron L-shell lines on EBIT-I, UNT Digital Library.  
<https://digital.library.unt.edu/ark:/67531/metadc1406374/m1/2/>
- Chen, H., Beiersdorfer, P., Scofield, J. H., et al. 2002, Astrophys. J., 567, L169, doi: [10.1086/340007](https://doi.org/10.1086/340007)
- . 2005, Astrophys. J., 618, 1086, doi: [10.1086/426135](https://doi.org/10.1086/426135)
- Chen, H., Gu, M. F., Beiersdorfer, P., et al. 2006, Astrophys. J., 646, 653, doi: [10.1086/504708](https://doi.org/10.1086/504708)
- Clementson, J., & Beiersdorfer, P. 2013, The Astrophysical Journal, 763, 54, doi: [10.1088/0004-637x/763/1/54](https://doi.org/10.1088/0004-637x/763/1/54)
- Dere, K. P., Zanna, G. D., Young, P. R., Landi, E., & Sutherland, R. S. 2019, The Astrophysical Journal Supplement Series, 241, 22, doi: [10.3847/1538-4365/ab05cf](https://doi.org/10.3847/1538-4365/ab05cf)
- Desclaux, J. P. 1975, Computer Physics Communications, 9, 31.  
<http://www.sciencedirect.com/science/article/pii/S0010465584825187>
- . 1993, in METTEC, Vol. A, Methods and Techniques in Computational Chemistry, ed. E. Clementi (Cagliary LB - des1993: STEF)
- DeWitt, D. R., Schneider, D., Chen, M. H., et al. 1992, Phys. Rev. Lett., 68, 1694, doi: [10.1103/PhysRevLett.68.1694](https://doi.org/10.1103/PhysRevLett.68.1694)
- Dudík, J., Dzifčáková, E., Del Zanna, G., et al. 2019, Astronomy and Astrophysics, 626, A88, doi: [10.1051/0004-6361/201935285](https://doi.org/10.1051/0004-6361/201935285)
- Durkin, M., Adams, J. S., Bandler, S. R., et al. 2019, IEEE Transactions on Applied Superconductivity, 29, 2904472.  
<https://doi.org/10.1109/TASC.2019.2904472>
- Epp, S. W., López-Urrutia, J. R. C., Simon, M. C., et al. 2010, Journal of Physics B: Atomic, Molecular and Optical Physics, 43, 194008. <http://stacks.iop.org/0953-4075/43/i=19/a=194008>
- Foster, A. R., Ji, L., Smith, R. K., & Brickhouse, N. S. 2012, The Astrophysical Journal, 756, 128.  
<http://stacks.iop.org/0004-637X/756/i=2/a=128>
- Gillaspy, J. D., Lin, T., Tedesco, L., et al. 2011, The Astrophysical Journal, 728, 132, doi: [10.1088/0004-637X/728/2/132](https://doi.org/10.1088/0004-637X/728/2/132)
- González Martínez, A. J., López-Urrutia, J., Braun, J., et al. 2005, Phys. Rev. Lett., 94, 203201, doi: [10.1103/PhysRevLett.94.203201](https://doi.org/10.1103/PhysRevLett.94.203201)
- Graf, A., Beiersdorfer, P., Brown, G. V., & Gu, M. F. 2009, The Astrophysical Journal, 695, 818, doi: [10.1088/0004-637X/695/2/818](https://doi.org/10.1088/0004-637X/695/2/818)
- Gu, L., Raassen, A. J. J., Mao, J., et al. 2019, Astronomy&Astrophysics, 51.  
<https://doi.org/10.1051/0004-6361/201833860>
- Gu, L., Shah, C., Mao, J., et al. 2020, arXiv e-prints, arXiv:2007.03843. <https://arxiv.org/abs/2007.03843>
- Gu, M. F. 2003, The Astrophysical Journal, 590, 1131, doi: [10.1086/375135](https://doi.org/10.1086/375135)
- . 2008, Canadian Journal of Physics, 86, 675, doi: [10.1139/p07-197](https://doi.org/10.1139/p07-197)
- Gu, M. F., Holczer, T., Behar, E., & Kahn, S. M. 2006, Astrophys. J., 641, 1227, doi: [10.1086/500640](https://doi.org/10.1086/500640)
- Gu, M. F., Kahn, S. M., Savin, D. W., et al. 2001, Astrophys. J., 563, 462, doi: [10.1086/323683](https://doi.org/10.1086/323683)
- . 1999, The Astrophysical Journal, 518, 1002, doi: [10.1086/307326](https://doi.org/10.1086/307326)
- Hahn, M., Becker, A., Bernhardt, D., et al. 2013, Astrophysical Journal, 767, 47, doi: [10.1088/0004-637X/767/1/47](https://doi.org/10.1088/0004-637X/767/1/47)
- Howat, G., Aberg, T., & Goscinski, O. 1978, Journal of Physics B: Atomic and Molecular Physics, 11, 1575, doi: [10.1088/0022-3700/11/9/011](https://doi.org/10.1088/0022-3700/11/9/011)
- Hu, Z., Li, Y., & Nakamura, N. 2013, Physical Review A, 87, 52706, doi: [10.1103/PhysRevA.87.052706](https://doi.org/10.1103/PhysRevA.87.052706)
- Indelicato, P. 1995, Physical Review A, 51, 1132.  
[http://prola.aps.org/abstract/PRA/v51/i2/p1132\\_1](http://prola.aps.org/abstract/PRA/v51/i2/p1132_1)
- Indelicato, P., & Desclaux, J. P. 1990, Physical Review A, 42, 5139. <http://link.aps.org/abstract/PRA/v42/p5139>
- Indelicato, P., Gorceix, O., & Desclaux, J. P. 1987, Journal of Physics B: Atomic and Molecular Physics, 20, 651.  
<http://iopscience.iop.org/0022-3700/20/4/007>
- Janev, R. K., Belić, D. S., & Bransden, B. H. 1983, Physical Review A, 28, 1293, doi: [10.1103/PhysRevA.28.1293](https://doi.org/10.1103/PhysRevA.28.1293)
- Kaastra, J. S., Mewe, R., & Nieuwenhuijzen, H. 1996, in 11th Colloq. on UV and X-ray Spectroscopy of Astrophysical and Laboratory Plasmas, 411–414.  
<http://adsabs.harvard.edu/abs/1996uxsa.conf.411K>

- Kim, Y. S., & Pratt, R. H. 1983, *Physical Review A*, 27, 2913, doi: [DOI:10.1103/PhysRevA.27.2913](https://doi.org/10.1103/PhysRevA.27.2913)
- Knapp, D. A., Marrs, R. E., Levine, M. A., et al. 1989, *Phys. Rev. Lett.*, 62, 2104, doi: [10.1103/PhysRevLett.62.2104](https://doi.org/10.1103/PhysRevLett.62.2104)
- Knapp, D. A., Marrs, R. E., Schneider, M. B., et al. 1993, *Phys. Rev. A*, 47, 2039, doi: [10.1103/PhysRevA.47.2039](https://doi.org/10.1103/PhysRevA.47.2039)
- Kühn, S., Shah, C., López-Urrutia, J., et al. 2020, *Phys. Rev. Lett.*, 124, 225001, doi: [10.1103/PhysRevLett.124.225001](https://doi.org/10.1103/PhysRevLett.124.225001)
- Laming, J. M., Kink, I., Takacs, E., et al. 2000, *The Astrophysical Journal Letters*, 545, L161, doi: [10.1086/317876](https://doi.org/10.1086/317876)
- Lindroth, E., Orban, I., Trotsenko, S., & Schuch, R. 2020, *Phys. Rev. A*, 101, 062706, doi: [10.1103/PhysRevA.101.062706](https://doi.org/10.1103/PhysRevA.101.062706)
- Linkemann, J., Müller, A., Kenntner, J., et al. 1995, *Physical Review Letters*, 74, 4173, doi: [10.1103/PhysRevLett.74.4173](https://doi.org/10.1103/PhysRevLett.74.4173)
- Lotz, W. 1968, *Zeitschrift für Physik A Hadrons and Nuclei*, 216, 241. <http://dx.doi.org/10.1007/BF01392963>
- Mao, J., Mernier, F., Kaastra, J., et al. 2019, *Journal of Instrumentation*, 14, C07012–C07012, doi: [10.1088/1748-0221/14/07/c07012](https://doi.org/10.1088/1748-0221/14/07/c07012)
- May, M. J., Beiersdorfer, P., Dunn, J., et al. 2005, *The Astrophysical Journal Supplement Series*, 158, 230, doi: [10.1086/429541](https://doi.org/10.1086/429541)
- Mernier, F., de Plaa, J., Werner, N., et al. 2018, *Monthly Notices of the Royal Astronomical Society: Letters*, 478, L116, doi: [10.1093/mnrasl/sly080](https://doi.org/10.1093/mnrasl/sly080)
- Micke, P., Kühn, S., Buchauer, L., et al. 2018, *Review of Scientific Instruments*, 89, doi: [10.1063/1.5026961](https://doi.org/10.1063/1.5026961)
- Nagayama, T., Bailey, J. E., Loisel, G. P., et al. 2019, *Physical Review Letters*, 122, 235001, doi: [10.1103/PhysRevLett.122.235001](https://doi.org/10.1103/PhysRevLett.122.235001)
- Nilsen, J. 1989, *Atomic Data and Nuclear Data Tables*, 41, 131, doi: [https://doi.org/10.1016/0092-640X\(89\)90028-4](https://doi.org/10.1016/0092-640X(89)90028-4)
- Paerels, F. B., & Kahn, S. M. 2003, *Annual Review of Astronomy and Astrophysics*, 41, 291, doi: [10.1146/annurev.astro.41.071601.165952](https://doi.org/10.1146/annurev.astro.41.071601.165952)
- Penetrante, B. M., Bardsley, J. N., DeWitt, D., Clark, M., & Schneider, D. 1991, *Phys. Rev. A*, 43, 4861, doi: [10.1103/PhysRevA.43.4861](https://doi.org/10.1103/PhysRevA.43.4861)
- Pindzola, M. S., Badnell, N. R., & Griffin, D. C. 1992, *Physical Review A*, 46, 5725, doi: [10.1103/PhysRevA.46.5725](https://doi.org/10.1103/PhysRevA.46.5725)
- Savin, D. W., & Laming, J. M. 2002, *The Astrophysical Journal*, 566, 1166, doi: [10.1086/338271](https://doi.org/10.1086/338271)
- Schmidt, E. W., Bernhardt, D., Hoffmann, J., et al. 2009, *Journal of Physics: Conference Series*, 163, 12028, doi: [10.1088/1742-6596/163/1/012028](https://doi.org/10.1088/1742-6596/163/1/012028)
- Schneider, M. B., Knapp, D. A., Chen, M. H., et al. 1992, *Phys. Rev. A*, 45, R1291, doi: [10.1103/PhysRevA.45.R1291](https://doi.org/10.1103/PhysRevA.45.R1291)
- Shah, C., Amaro, P., Steinbrügge, R., et al. 2018, *Astrophys. J. Supplement*, 234, 27, doi: [10.3847/1538-4365/aaa4c0](https://doi.org/10.3847/1538-4365/aaa4c0)
- Shah, C., López-Urrutia, J. R. C., Gu, M. F., et al. 2019, *The Astrophysical Journal*, 881, 100, doi: [10.3847/1538-4357/ab2896](https://doi.org/10.3847/1538-4357/ab2896)
- Tashiro, M., Maejima, H., Toda, K., et al. 2018, *Proc. SPIE*, 10699, 1069922. <https://doi.org/10.1117/12.2309455>
- Tsuda, T., Shimizu, E., Ali, S., et al. 2017, *The Astrophysical Journal*, 851, 82, doi: [10.3847/1538-4357/aa97e5](https://doi.org/10.3847/1538-4357/aa97e5)
- Tu, B., Xiao, J., Yao, K., et al. 2015, *Phys. Rev. A*, 91, 060502(R), doi: [10.1103/PhysRevA.91.060502](https://doi.org/10.1103/PhysRevA.91.060502)
- . 2016, *Phys. Rev. A*, 93, 032707, doi: [10.1103/PhysRevA.93.032707](https://doi.org/10.1103/PhysRevA.93.032707)
- Xiong, G., Zhang, J., Hu, Z., et al. 2013, *Physical Review A*, 88, 042704, doi: [10.1103/PhysRevA.88.042704](https://doi.org/10.1103/PhysRevA.88.042704)
- Yao, K., Geng, Z., Xiao, J., et al. 2010, *Physical Review A*, 81, 22714, doi: [10.1103/PhysRevA.81.022714](https://doi.org/10.1103/PhysRevA.81.022714)
- Yates, R. M., Thomas, P. A., & Henriques, B. M. B. 2017, *Monthly Notices of the Royal Astronomical Society*, 464, 3169, doi: [10.1093/mnras/stw2361](https://doi.org/10.1093/mnras/stw2361)
- Zatsarinny, O., Gorczyca, T. W., Fu, J., et al. 2006, *Astronomy and Astrophysics*, 447, 379, doi: [10.1051/0004-6361:20053737](https://doi.org/10.1051/0004-6361:20053737)
- Zatsarinny, O., Gorczyca, T. W., Korista, K., Badnell, N. R., & Savin, D. W. 2004, *Astronomy and Astrophysics*, 426, 699, doi: [10.1051/0004-6361:20040463](https://doi.org/10.1051/0004-6361:20040463)